Helmholtz-Zentrum Potsdam - Deutsches GeoForschungsZentrum
Sektion 2.5 - Geodynamische Modellierung

GPS based analysis of earthquake induced phenomena at the Sunda Arc

Dissertation
zur Erlangung des akademischen Grades
'doctor rerum naturalium' (Dr. rer. nat.)
in der Wissenschaftsdisziplin 'Geophysik'

eingereicht an der
Mathematisch-Naturwissenschaftlichen Fakultät
der Universität Potsdam

vorgelegt von
Dipl. phys. Andreas Höchner
Potsdam, September 2010

Abstract

Indonesia is one of the countries most prone to natural hazards. Complex interaction of several tectonic plates with high relative velocities leads to approximately two earthquakes with magnitude $M_w>7$ every year, being more than 15% of the events worldwide. Earthquakes with magnitude above 9 happen far more infrequently, but with catastrophic effects. The most severe consequences thereby arise from tsunamis triggered by these subduction-related earthquakes, as the Sumatra-Andaman event in 2004 showed. In order to enable efficient tsunami early warning, which includes the estimation of wave heights and arrival times, it is necessary to combine different types of real-time sensor data with numerical models of earthquake sources and tsunami propagation.

This thesis was created as a result of the GITEWS project (German Indonesian Tsunami Early Warning System). It is based on five research papers and manuscripts. Main project-related task was the development of a database containing realistic earthquake scenarios for the Sunda Arc. This database provides initial conditions for tsunami propagation modeling used by the simulation system at the early warning center. An accurate discretization of the subduction geometry, consisting of 25x150 subfaults was constructed based on seismic data. Green's functions, representing the deformational response to unit dip- and strike slip at the subfaults, were computed using a layered half-space approach. Different scaling relations for earthquake dimensions and slip distribution were implemented. Another project-related task was the further development of the 'GPS-shield' concept. It consists of a constellation of near field GPS-receivers, which are shown to be very valuable for tsunami early warning.

The major part of this thesis is related to the geophysical interpretation of GPS data. Coseismic surface displacements caused by the 2004 Sumatra earthquake are inverted for slip at the fault. The effect of different Earth layer models is tested, favoring continental structure. The possibility of splay faulting is considered and shown to be a secondary order effect in respect to tsunamigenity for this event. Tsunami models based on source inversions are compared to satellite radar altimetry observations.

Postseismic GPS time series are used to test a wide parameter range of uni- and biviscous rheological models of the asthenosphere. Steady-state Maxwell rheology is shown to be incompatible with near-field GPS data, unless large afterslip, amounting to more than 10% of the coseismic moment is assumed. In contrast, transient Burgers rheology is in agreement with data without the need for large aseismic afterslip. Comparison to postseismic geoid observation by the GRACE satellites reveals that even with afterslip, the model implementing Maxwell rheology results in amplitudes being too small, and thus supports a biviscous asthenosphere.

A simple approach based on the assumption of quasi-static deformation propagation is introduced and proposed for inversion of coseismic near-field GPS time series. Application of this approach to observations from the 2004 Sumatra event fails to quantitatively reconstruct the rupture propagation, since a priori conditions are not fulfilled in this case. However, synthetic tests reveal the feasibility of such an approach for fast estimation of rupturing properties.

Zusammenfassung

Indonesien ist eines der am stärksten von Naturkatastrophen bedrohten Länder der Erde. Die komplexe Interaktion mehrer tektonischer Platten, die sich mit hohen Relativgeschwindigkeiten zueinander bewegen, führt im Mittel zu ungefähr zwei Erdbeben mit Magnitude $M_w>7$ pro Jahr, was mehr als 15% der Ereignisse weltweit entspricht. Beben mit Magnitude über 9 sind weitaus seltener, haben aber katastrophale Folgen. Die schwerwiegendsten Konsequenzen hierbei werden durch Tsunamis verursacht, welche durch diese Subduktionsbeben ausgelöst werden, wie das Sumatra-Andamanen Ereignis von 2004 gezeigt hat. Um eine wirksame Tsunami-Frühwarnung zu ermöglichen, welche die Abschätzung der Wellenhöhen und Ankunftszeiten beinhaltet, ist es erforderlich, verschieden Arten von Echtzeit-Sensordaten mit numerischen Modellen für die Erdbebenquelle und Tsunamiausbreitung zu kombinieren.

Diese Doktorarbeit wurde im Rahmen des GITEWS-Projektes (German Indonesian Tsunami Early Warning System) erstellt und umfasst fünf Fachpublikationen und Manuskripte. Projektbezogene Hauptaufgabe war die Erstellung einer Datenbank mit realistischen Bebenszenarien für den Sundabogen. Die Datenbank beinhaltet Anfangsbedingungen für die Tsunami-Ausbreitungsmodellierung und ist Teil des Simulationssystems im Frühwarnzentrum. Eine sorgfältige Diskretisierung der Subduktionsgeometrie, bestehend aus 25x150 subfaults, wurde basierend auf seismischen Daten erstellt. Greensfunktionen, welche die Deformation, hervorgerufen durch Verschiebung an den subfaults ausmachen, wurden mittels eines semianalytischen Verfahrens für den geschichteten Halbraum berechnet. Verschiedene Skalierungsrelationen für Erdbebendimension und slip-Verteilung wurden implementiert. Eine weitere projektbezogene Aufgabe war die Weiterentwicklung des ‚GPS-Schild'-Konzeptes. Dieses besteht aus einer Konstellation von GPS-Empfängern im Nahfeldbereich, welche sich als sehr wertvoll für die Tsunami-Frühwarnung erweisen.

Der größere Teil dieser Doktorarbeit beschäftigt sich mit der geophysikalischen Interpretation von GPS-Daten. Coseismische Verschiebungen an der Erdoberfläche, ausgelöst durch das Erdbeben von 2004, werden nach slip an der Verwerfung invertiert. Die Wirkung verschiedener Erdschichtungsmodelle wird getestet und resultiert in der Bevorzugung einer kontinentalen Struktur. Die Möglichkeit von splay-faulting wird untersucht und erweist sich als zweitrangiger Effekt bezüglich der Tsunamiwirkung für dieses Ereignis. Die auf der Quelleninversion basierenden Tsunamimodelle werden mit satellitengestützen Radaraltimetriedaten verglichen.

Postseismische GPS-Daten werden verwendet, um einen weiten Parameterbereich uni- und bi-viskoser Modelle der Asthenosphäre zu testen. Dabei stellt sich stationäre Maxwell-Rheologie als inkompatibel mit Nahfeld-GPS-Zeitreihen heraus, es sei denn, eine große Quantität an afterslip, entsprechend etwa 10% des coseismischen Momentes, wird angenommen. Im Gegensatz dazu ist die transiente Burgers-Rheologie ohne große Mengen an afterslip kompatibel zu den Beobachtungen. Der Vergleich mit postseismischen Geoidbeobachtungen durch die GRACE-Satelliten zeigt, dass das Modell basierend auf Maxwell-Rheologie, auch mit afterslip, zu kleine Amplituden liefert, und bekräftigt die Annahme einer biviskosen Rheologie der Asthenosphäre.

Ein einfacher Ansatz, der auf einer quasi-statischen Deformationsausbreitung beruht, wird eingeführt und zur Inversion coseismischer Nahfeld-GPS-Zeitreihen vorgeschlagen. Die Anwendung dieses Ansatzes auf Beobachtungen vom Sumatra-Beben von 2004 ermöglicht nicht die quantitative Rekonstruktion der Ausbreitung des Bruches, da die notwendigen Bedingungen in diesem Fall nicht erfüllt sind. Jedoch zeigen Experimente an synthetischen Daten die Gültigkeit eines solchen Ansatzes zur raschen Abschätzung der Bruchausbreitungseigenschaften.

Abstrak

Indonesia adalah salah satu negara yang paling rawan terhadap bencana alam. Interaksi komplek antara beberapa lempeng tektonik yang bergerak dengan kecepatan relatif tinggi menyebabkan sekitar 2 gempabumi dengan kekuatan M_w>7 per tahun, yang merupakan 15% dari seluruh kejadian gempa di bumi. Walaupun gempabumi dengan kekuatan lebih besar dari 9 lebih jarang terjadi, namun dampaknya dapat menimbulkan malapetaka. Dampak yang paling hebat adalah timbulnya tsunami yang dipicu oleh gempabumi pada zona subduksi, seperti yang ditunjukkan oleh peristiwa Sumatra-Andaman 2004. Untuk menghasilkan peringatan dini tsunami yang efisien, yang mencakup estimasi ketinggian gelombang dan waktu tiba, kita perlu menggabungkan berbagai jenis data sensor real time dan model numerik dari proses terjadinya gempa dengan perambatan gelombang tsunami.

Disertasi ini merupakan bagian dari proyek GITEWS (German Indonesian Early Warning System). Tugas utama dari tesis ini adalah membangun database gempabumi untuk Busur Sunda. Database memberikan syarat awal untuk pemodelan perambatan tsunami yang digunakan oleh sistem simulasi di pusat peringatan dini. Suatu model diskrit akurat dari geometri subduksi yang terdiri dari 25x150 patahan, dibangun berdasarkan data seismik tersebut. Fungsi Green's yang menggambarkan respon deformasi terhadap satuan dip dan strike pada patahan, dihitung menggunakan pendekatan medium berlapis setengah ruang. Relasi skala yang berbeda untuk dimensi gempa dan distribusi pergeseran juga diterapkan. Tugas lain dari disertasi ini adalah mengembangkan lebih lanjut konsep ‚GPS-shield‘ yang terdiri atas suatu konstelasi beberapa penerima GPS near field yang sangat berguna dalam peringatan dini tsunami.

Sebagian besar dari disertasi ini berhubungan dengan interpretasi geofisika dari data GPS. Pergeseran koseismik di permukaan yang disebabkan oleh gempa 2004 diinversi untuk mendapatkan nilai slip pada patahan. Efek dari berbagai model bumi berlapis diuji, terutama yang mewakili struktur kontinen. Kemungkinan terjadinya patahan splay dipertimbangkan dan terbukti merupakan efek sekunder dari kejadian tsunami. Berbagai model tsunami berdasarkan inversi sumber gempa juga dibandingkan terhadap hasil observasi altimetri radar satelit.

Data GPS fungsi waktu digunakan untuk menguji parameter model reologi univiskos dan biviskos dari astenosfer. Reologi steady-state Maxwell ternyata tidak sesuai dengan data GPS near field, kecuali jika nilai afterslip cukup besar, lebih besar dari 10% asumsi momen koseismiknya. Sebaliknya, reologi transien Burgers cocok dengan data, tanpa memerlukan nilai afterslip aseismik yang besar. Perbandingan dengan observasi geoid pascaseismik oleh satelit GRACE memperlihatkan bahwa dengan adanya afterslip sekalipun, model yang menerapkan reologi Maxwell menghasilkan amplitudo yang terlalu kecil, dan hal ini berarti mendukung astenosfer biviskos.

Sebuah pendekatan sederhana terhadap asumsi perambatan deformasi kuasi-statik diajukan untuk inversi GPS near field fungsi waktu. Aplikasi pendekatan ini terhadap data dari kejadian Sumatra 2004 tidak berhasil merekonstruksi secara kuantitatif perambatan robekan karena syarat awal tidak terpenuhi dalam kasus ini. Namun demikian, uji sintetik mengungkapkan kelayakan pendekatan tersebut dalam mengestimasi secara cepat sifat-sifat dari robekan.

1 Contents

2 Introduction

2.1 Thesis context

The present thesis was created in the framework of the GITEWS project (German Indonesian Tsunami Early Warning System), which was a response to the devastating earthquake and tsunami in the Indian Ocean in December 2004 [Rudloff et al., 2009]. Leadership of the project was situated at the German Research Centre for Geosciences (GFZ) and headed by Dr. Jörn Lauterjung.

Before the 2004 event, the Sunda Arc was not widely present in the perception of the authorities, the public and many experts as being capable of earthquakes of more than magnitude M_w=9, and thus as posing a high threat to coastal areas in the whole Indian Ocean. As a consequene, the region was neither prepared in terms of early warning, nor in terms of disaster response and the event took almost a quarter of a million of lives, some as far as the east coast of Africa. Since then, large efforts were made to improve the situation. On the technical side by installing numerous instruments such as seismometers, GPS receivers, buoys and tide gauges. They allow real-time monitoring and facilitate increasing of knowledge about the tectonic situation. The development of a simulation- and a decision support system enables the staff of the warning center to react quickly and adequately. Capacity building made huge progress, encompassing giving mandates to dedicated institutions, set-up of an early warning center, training of personnel and education of the public.

Especially challenging in the case of Indonesia is the fact that due to its vicinity to the Sunda Arc, tsunami waves may arrive at the coast in less than half an hour, requiring very fast detection and decision support mechanisms [Lauterjung et al., 2010]. A central role thereby is played by the simulation system, which processes data from various sensor types and provides wave heights and arrival times together with uncertainty estimates. The work package responsible for the simulation system within the GITEWS project comprised three parts: tsunami source modeling, deep water wave propagation- and coastal inundation modeling. The first one was further divided in earthquake- and (submarine) landslide type sources. While the latter subject was covered by my colleague Sascha Brune [Brune, 2009], this thesis is related to the most frequent and destructive earthquake-type tsunami sources.

My PhD position included the development and testing of a database of synthetic earthquake scenarios for the Sunda Arc for tsunami early warning, something that had not been done before in Germany. It also involved teaching and training of the staff of the warning center in Indonesia. Better understanding of the source processes is crucial in order to advance the technologies used to mitigate the effects of future events. GPS turned out to be a very valuable tool in this respect. I performed inversions for slip of the 2004 and other events, which provided useful know-how for the implementation of the scenario database. Most scientific activities involved geophysical interpretation of GPS data, be it for coseismic or postseismic phenomena, as I will further explain in section 2.5 and as can be seen in the list of publications in chapter 11.

2.2 Study area

The GITEWS project was started with signing of the Joint Declaration between Germany and Indonesia in march 2005, but soon other countries showed interest and participated in several activities, which almost changed the meaning of 'GITEWS' to 'German Indian ocean Tsunami Early Warning System'. However, main focus remained on the Sunda Arc. Special attention was given to the southern part of Sumatra. Large earthquakes with associated tsunami occurred in that region in the past centuries [Sieh et al., 2008], and significant events happened after the 2004 earthquake, but based on analysis of locking conditions at the fault, accumulated slip deficit is not thought to have been fully released [Konca et al., 2008], thus still posing a threat for instance to the highly populated and strongly exposed city of Padang.

The database of synthetic earthquakes we built comprises the whole Sunda Arc as shown in Figure 2.1 Most of the GPS data used in this thesis are related to the effects of the Sumatra 2004 earthquake, which started offshore the northern tip of Sumatra and propagated to the north until the Andaman Islands [Krüger and Ohrnberger, 2005b].

2.3 Project tasks and scientific goals

Main task of the tsunami source modeling group of GITEWS, which was based at GFZ and headed by Dr. Andrey Babeyko, was the develpment of a database containing possible earthquakes along the Sunda Arc. To this purpose we set up a software tool called 'RuptGen'. Requiring a minimal input of epicenter and magnitude, it computes slip distribution at the fault, deformation of the sea floor and response of GPS receivers.

Responsibility of the simulation package, including deep water wave propagation and a matching tool for the database was situated at Alfred Wegener Institute in Bremerhaven (AWI) under leadership of Prof. Jörn Behrens. We also did tsunami modeling in our group at GFZ in order to analyze the strong nonlinearities introduced by bathymetric features such as the Mentawai Islands offshore Sumatra, to compare the efficiency of various inversion strategies and to demonstrate the power of the so-called 'GPS-shield' concept [Sobolev et al., 2007] (see chapter 7), which matters very much to us since it can overcome several problems associated with traditional tsunami warning approaches and represents an ideal complement to recent seismological developments as in [Roessler et al., 2010]. However, practical implementation of such a system within GITEWS gained momentum only recently [Falck et al., 2010].

Since sensor systems are still being installed and enhanced, and large events are rare and only partially captured, another benefit from the simulation system lies in the possibility to generate coherent synthetic scenarios including the response at seismometers, GPS receivers, buoys and tide gauges, which can be used instead of real world observations for testing of the sensor communication infrastructure, database selection tool and decision support logic, as well as for training purposes for the staff of the warning center.

A more exotic application of GPS for tsunami early warning was studied in [Stosius et al., 2010], where the possibility to observe reflected GPS signals from the sea surface using a constellation of low earth orbiting satellites is analyzed in order to enable global monitoring. However I did not include this publication in the thesis, since my contribution consisted in providing tsunami models of past and possible events in the Indian Ocean and the Mediterranean and did not involve the main topic of above study.

Besides contributing to mitigate the impact of future catastrophic events, my PhD position at GFZ and Potsdam University offered the opportunity to explore scientific possibilities associated with the analysis of co- and postseismic GPS time series. I performed inversions in order to reconstruct slip distribution (Chapter 3) or rupture timing (Chapter 6), and performed a parameter search together with the analysis of satellite-based geoid data enabling to infer rheological properties of the asthenosphere (Chapter 5). My contributions are described in more detail in section 2.5.

2.4 Tectonic setting

An excellent review of the tectonic setting of the region of interest of this study is given in: 'The Tectonic Framework of the Sumatran Subduction Zone' [McCaffrey, 2009]. I give an outline of the relevant aspects.

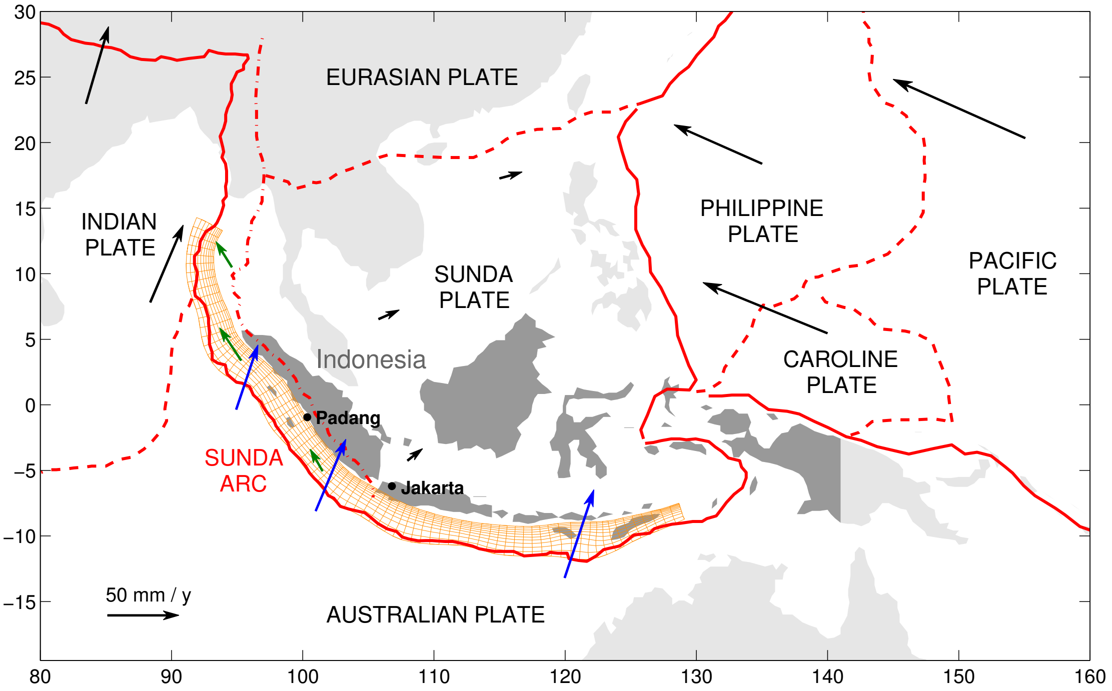

Figure 2.1 Tectonic setting of Indonesia. Red lines: solid: major plate boundaries, dashed: minor plate boundaries, dash-dotted: Sumatran fault system and continuation to north. Arrows: black: relative velocities to the Eurasian plate, blue: relative to the Sunda plate, green: motion of the forearc sliver plate (Burma plate) relative to the Sunda plate. Orange mesh: discretization of the subduction interface (actual subfaults in the database are half as large).

Indonesia is situated at the triple junction of the Indian-Australian, the Eurasian and the Pacific tectonic plates. The high relative motions of the plates and the further complications caused by interaction of sub plates and intraplate deformation makes it one of the most seismically active regions of the Earth. In the region of Sumatra, the Indian Ocean seafloor is subducted with a relative velocity of about 40-50 mm per year beneath the continental Sunda shelf. Subduction related volcanism in Sumatra occurred at least since the Oligocene, indicating that the setting has been close to its present form for more than 20 million years. This means that very large events have repeated up to tens of thousands of times, but only few of them are documented or have been reconstructed by now.

The Barisan mountain range, which forms the backbone of Sumatra, coincides roughly, but not exactly with the Sumatran fault system. This feature of 1900 km length takes up part of the oblique convergence in form of right lateral motion, being 6 mm/y at the Sunda strait to about 40 mm/y in the north and leads to independent motion of the forearc. Due to the strong segmentation of the fault system, and because of the smaller maximum width of the fault as compared to the subduction fault, strike-slip earthquakes at Sumatra are probably limited to a magnitude M_w of less than 8, which nevertheless poses an enormous threat to the densely populated area [Petersen et al., 2004; Sørensen and Atakan, 2008].

Between the trench, running parallel to the coast at a distance of about 200 km, and the mainland of Sumatra, lies the nonvolcanic forearc ridge, giving rise to the Mentawai islands. These are formed as a result of the scraping off and accumulation of sediments during the subduction process. Most of the sediments are brought in as a result of the collision of India with the Eurasian plate from the Himalayas and to a lesser degree from the Sumatran mountain range. These islands, which are not present in most other subduction zones, offer the opportunity of geodetic and seismological observations in proximity of the trench. They reveal strong heterogeneities, which can be explained by different age and thus temperature and density of the incoming lithosphere, unequal sediment influx, geometric variation of the relative motion and bathymetric features such as ridges and sea mounts. Locking conditions at the subduction zone have also been derived by analysis of coral heads [Sieh et al., 1999].

2.5 Structure of the thesis

This thesis is based on five papers which are either published, accepted, or to be submitted to peer-reviewed international journals (see chapter 11). Two more publications I co-authored are not included in the thesis. Some non-scientific materials are appended.

In chapter 3: ‘Enhanced GPS inversion technique applied to the 2004 Sumatra Earthquake and Tsunami’ I use coseismic GPS observations from the great Sumatra earthquake to derive coseismic slip distribution at the fault. By applying an accurate discretization of the subduction interface, physical boundary conditions and Earth layering according to IASP91 continental structure, I show that discrepancies between near- and far field observations, otherwise assigned to postseismic contamination, can be overcome. Inverted tsunami source models are consistent with satellite radar altimetry data. Splay faulting is possible but has only second-order contribution to the tsunami for this event.

Chapter 4 contains technical auxiliary material published together with the paper from the previous section, namely some additional informations and tests concerning geometry of the fault zone, Earth layering and the effect of horizontal displacement on tsunamigenity.

In chapter 5: ‘Investigation on afterslip and steady state and transient rheology based on postseismic deformation and geoid change caused by the Sumatra 2004 earthquake’ I show that univiscous Maxwell rheology without afterslip is incompatible with GPS time series, while biviscous Burgers rheology is in good agreement. Comparison of the postseismic geoid change induced by the earthquake and observed by the GRACE satellites to model results, shows that Maxwell rheology, even including afterslip, yields too small amplitudes, and thus is a strong indication of transient rheological behavior in the asthenosphere.

Chapter 6: ‘Deriving Earthquake Rupture Timing from GPS Observations’ is a manuscript in which I apply a straightforward approach based on the assumption of quasi-static evolution of deformation to coseismic GPS time series. Using synthetic tests I show that for large earthquakes and near-field receivers it is possible to quantitatively derive rupture properties. Application to far-field data from the Sumatra 2004 earthquake correctly resolves the epicenter region and rupturing direction but yields too high rupture velocity, since the requirements for above assumption are not satisfied in this case.

The first publication I was involved in: ‘Tsunami early warning using GPS-Shield arrays’, comprised in chapter 7, introduces a concept for tsunami early warning based on strategically placed arrays of GPS receivers in the vicinity of the Sunda Arc or other subduction zones. By performing statistical analysis on one-dimensional profiles it demonstrates the resolving power of such a system in terms of magnitude and location, depending on the distance of the receivers to the trench. I contributed inversions of realistic and a checkerboard scenario as well as a performance analysis regarding time using synthetic seismograms. In the appendix I compare an analytical expression for slip perpendicular to the trench to the result obtained from the Sumatra earthquake.

Chapter 8: ’Source modeling and inversion with near real-time GPS: a GITEWS perspective for Indonesia’ summarizes the results and products obtained in order to achieve the goals related to the GITEWS project. We introduce the ‘RuptGen’ software tool, to which I contributed the discretization of the Sunda Arc, computation of the Green’s functions and testing of scaling relations for earthquake dimensions and slip distribution. ‘RuptGen’ was used to set up the database of realistic earthquakes used by the warning center in Jakarta. Some historical events are presented and the importance of coherent synthetic scenarios for testing and training is stressed. I further compare different inversion strategies applied to heterogeneous slip distributions.

The appendix ‘Public outreach’ (chapter 10) contains some materials for educational purposes in whose preparation I was involved in. I include them, since they reflect that the GITEWS project and also my PhD position were not only purely scientific ventures.

3 Enhanced GPS inversion technique applied to the 2004 Sumatra Earthquake and Tsunami

Andreas Hoechner[1], Andrey Y. Babeyko[1], Stephan V. Sobolev[1,2]
[1]GFZ German Research Centre For Geosciences, Potsdam, Germany
[2]Institute of Physics of the Earth, Moscow, Russia

An edited version of this paper was published in: Geophysical Research Letters, 35, L08310, doi: 10.1029/2007GL033133. Received 28 December 2007; accepted 26 March 2008; published 25 April 2008. Reviewed by R. Bürgmann and another anonymous referee. Copyright (2008) American Geophysical Union.

3.1 Abstract

Since the devastating earthquake and tsunami in 2004 offshore Sumatra, many source models have been put forward. Recent studies clearly show that modern GPS-processing could achieve high resolving power for slip in near real time, which is crucial for determining tsunami initial conditions, provided accurate GPS-processing and inversion. Here, we propose an inversion technique with improved representation of the subduction zone geometry and physically justified boundary conditions. We show that the discrepancy between the inversion of near- and far field GPS data for the 2004 event, which is often explained by postseismic slip, can be eliminated by using our inversion method and IASP91 earth model. Inverted source models, including versions with splay faulting, are shown to be consistent with satellite altimetry data of offshore tsunami wave height, suggesting that displacement at the splay fault might have been present but was likely a second order process.

3.2 Introduction

The Sumatra-Andaman earthquake of December 2004 is probably the most extensively analyzed earthquake-tsunami event ever. Recently, a number of special issues of scientific journals (see introductory papers by) have been dedicated to the investigation of a very broad spectrum of aspects of this event. Tsunami source models have been proposed based on seismic, tide gauge, satellite altimetry, GPS-data and combinations thereof. Of first order importance as initial condition for the tsunami is the static deformation of the sea bed resulting from the coseismic relative motion between the subducted oceanic and the overriding continental plate It can be computed if the slip distribution at the fault zone is known. While teleseismic inversions yield a detailed picture of rupture timing and extent [Krüger and Ohrnberger, 2005a], GPS-inversions provide a more direct measure for slip [Banerjee et al., 2007], are available shortly after an earthquake [Blewitt et al., 2006], and could even be used to follow rupture propagation in near-real time [Sobolev et al., 2007]. It is one of the goals of the German Indonesian Tsunami Early Warning System (GITEWS) to provide reliable information about expected arrival times, wave heights and inundation as quickly as possible to local warning centers in order to save lives and protect infrastructure. This is rendered difficult by the geomorphological settings in Indonesia: the trench is located closely to the coast, and the bathymetry is complex, including islands either protecting the main land or trapping tsunami energy in the forearc basin in case of a deep earthquake. Traditionally used tsunami source models based on epicenter and magnitude are not first choice: The epicenter does not necessarily coincide with the position of slip maximum, slip heterogeneities play an important role in the near-field [Geist and Dmowska, 1999], and the magnitude of large earthquakes is often underestimated during the first minutes. Thus, some events might not be recognized as being dangerous while at the same time the number of false alarms would be prohibitively high. These problems can be overcome using GPS [Sobolev et al., 2006; Sobolev et al., 2007], which is ideally suited for local Tsunami early warning.

However, GPS based inversions for slip distribution still need to be improved. Recent inversions for the Sumatra 2004 event imply inconsistency between near- (<300 km) and far field (300-900 km) GPS data and tend to underestimate tsunami wave heights compared to satellite radar altimetry data ([Chlieh et al., 2007; Pietrzak et al., 2007]). Chlieh et al. [2007] attribute the apparent inconsistency in the GPS observations to large unconsidered postseismic slip, which, however, was not confirmed by the analyses of Banerjee et al. [2007]. Discrepancy between predicted and observed tsunami wave heights may arise due to activation of splay faults [Plafker et al., 2007], but may also result from an inappropriate earth model used in inversion (see below). To address these issues, we first present an enhanced inversion technique, and then apply this technique to the Sumatra 2004 event, focusing primarily on roles of postseismic slip and splay faulting by comparison of our modeling results with observations.

3.3 Methods

We employ the following slip inversion procedure. First, the subduction interface is discretized into subfaults. A Green's functions approach is used to find the slip distribution which minimizes misfit between observed and modeled GPS displacements and which is in compliance with imposed physical boundary conditions. Finally, the slip distribution at the fault is used to compute the coseismic deformation of the sea floor, which provides the initial condition for the tsunami wave propagation code.

Most GPS based approaches, this study included, rely on a-priori knowledge of the potential fault zone geometry because, on the one hand, inversion for fault geometry itself is highly nonlinear, computationally intensive [Maerten et al., 2005] and requires a number of measurements which is rarely achieved with nowadays distribution of GPS-receivers. On the other hand, especially for large subduction earthquakes being of importance in the tsunami early warning context, slip can be assumed to be localized fairly well near the top of the Benioff zone, with exception maybe of particularities like splay faults. Discretization of the fault should provide resolution high enough to allow for realistic slip heterogeneities [Geist and Dmowska, 1999], overlap of adjacent subfaults should be minimized and variation of the dip angle along and perpendicular to the trench has to be taken into account. We propose an algorithm to perform automatic discretization of the subduction interface which will be made available, and works as described in the supplement A splay faulting option is included in the form of assigning a fix dip angle to selected subfaults (or using these faults additionally).

Our reference fault geometry model for the 2004 event consists of 12x36=432 subfaults ranging from 5 to 53 km depth (models ranging deeper revealed no slip below 50 km). Additionally, we constructed two models featuring splay faulting: model Sp260 and model Sp845a are described in the 'Results' section, inversions using other geometries can be found in the supplement.

For the forward model we use FORTRAN code EDGRN/ EDCMP by R. Wang et al. [2003] which is based on a semi-analytical approach for a layered half-space and applies an orthogonalization scheme to accurately compute the layering effects. We restrict ourselves to GPS-stations which are located closer than 900 km from their nearest subfault, hence sphericity does not play a significant role [Banerjee et al., 2005; Chlieh et al., 2007], especially since some distance correction is taken into account by using a stereographic projection from spherical to cartesian coordinates. Earth layering models are based on IASP91, PREM (continental) and CRUST2 (oceanic) seismic velocity models.

The inversion concept is similar to the one used by other authors, but provides some changes concerning regularization to enhance physical justification of the boundary conditions. Green's functions, being the response of the GPS-stations (three or two components) to unit dip- and strike-slip at the subfaults, are computed. The number of model parameters is larger than the number of observations, which renders the inversion an optimization problem. The cost-function to be minimized is set up in the following way:

$$C = \chi^2_{red} + \lambda_1 S_{slip} + \lambda_2 S_{azi}$$

with

$$\chi^2_{red} = \frac{1}{N} \sum_{Sta} \sum_{Dim} \frac{\left(d^{obs}_{mn} - d^{mod}_{mn}\right)^2}{\sigma^2_{mn}}$$, chi-square reduced,

$$S_{slip} = \sum_{SF} \sum_{NN+BND} \left(slip_i - slip_j\right)^2$$, smoothing of norm of slip,

$$S_{azi} = \sum_{SF} \sum_{NN} \left(azi_i - azi_j\right)^2$$, smoothing of azimuth of slip,

$$azi_i = strike_i - \arctan(\tan(rake_i) \cdot \cos(dip_i))$$, azimuth of slip vector.

The weighting factors λ_1 and λ_2 for the smoothing terms are calibrated using synthetic scenarios with checkerboard, homogenous (end members) and realistic slip distributions. Summation for χ^2 is over the available displacement components at all GPS-stations, d^{obs} are the observed, d^{mod} are the modeled (predicted) displacements and σ are the 1-sigma standard deviations. Summation in the smoothing terms is over all subfaults (SF) and their respective nearest neighbors (NN). Additionally, for the slip-smoothing term a 'virtual' subfault layer is placed at the lower and lateral boundaries (BND) which is set to zero to avoid physically impossible infinite stress concentration at the fault boundaries. The slip smoothing regularization with above boundary conditions enables us to skip global moment minimization or driving moment towards an a-priori target as done e.g. by Subarya et al. [2006] or Chlieh et al. [2007]. The first would lead to patchy patterns with high slip at measurement points and low slip in-between, while the second is hard to justify, because seismic and geodetic moment are not easily comparable as being derived from very different frequencies and measuring different processes (energy release vs. acoustic luminosity [Menke et al., 2006]). Instead of applying smoothing to rake angles, we apply it to azimuth of slip vectors. This makes some difference for large events with strongly varying strike- and dip angles, and is in accordance to the relative motion of the tectonic plates. No minimum/maximum constraints on slip and rake are required. Minimization of the cost function is performed with a quasi-Newton line-search algorithm from the [Matlab] Optimization Toolbox.

3.4 GPS Data

We use GPS data published by by Banerjee et al. [2007] (Electronic Supp. Table S1-S4), who integrated their own GPS solutions with coseismic displacements from earlier studies ([Vigny et al., 2005; Banerjee et al., 2005; Gahalaut et al., 2006; Subarya et al., 2006]) in a consistent fashion, and apply two modifications: (1) only stations being less than 900 km from their closest subfault are used in order not to violate limits of our non-spherical forward model, and (2) data originally published by Gahalaut et al. [2006] are assigned 1-sigma standard deviations being 15 times larger, following the argument by Chlieh et al. [2007]. Altogether 33 measurements with 3 components and 48 measurements with only horizontal displacements yielding a total of 195 data points are used and listed in the supplement.

Usually, timing of the rupture can be neglected for tsunami initial conditions. For this exceptionally large event though, which lasted around 10 minutes, some influence of the timing is reflected in the sea surface height as recorded by satellite JASON1 (see section 4.4). Here, we base the timing of the source on a GPS-inversion for rupture propagation by Vigny et al. [2005]. It is generally consistent with teleseismic analysis by Krüger and Ohrnberger [2005] and shows slip having started at 94.7° E / 3.1 °N and rupture velocity being around 3.7 km/s for the first 200 km and then slowing down to about 2 km/s. Rise time is assumed to be 60 s. Effect of timing on JASON1-track is shown in section 4.4.

3.5 Results

In general, our inversion is in agreement with previous studies, e.g. Chlieh et al. [2007]. Inverted slip, together with observed and modeled GPS displacements for different crustal models is shown in Figure 3.1. Clearly localized patches with maximum slip of approximately 24 m are located around 4° N and between 6 and 9° N. Smaller, but still significant amount of slip is found in the Andaman segment of the rupture. The upper model in Figure 3.1 has been computed using earth layering corresponding to IASP91 crustal structure (continental), the lower corresponding to CRUST2 (oceanic). The IASP91 model smoothly fits the whole dataset, whereas the CRUST2 model over predicts near- and under predicts far field data. Chlieh et al. [2007] attributed this deficiency to post-seismic slip that occurred before the near-field measurements were collected and which has not been accounted for correctly. However, our inversion shows that this discrepancy is drastically reduced if a continental crust earth model (IASP91) is used, leaving only minor need for postseismic slip. GPS-residuals and an additional model using PREM layering are shown in the supplement, together with energy release projected on latitude.

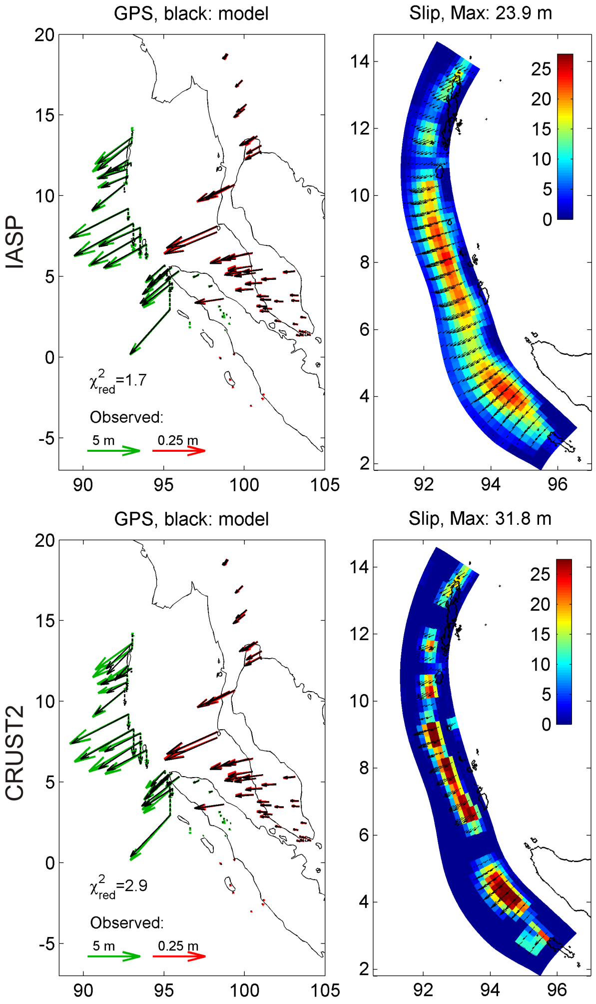

Figure 3.1 Comparison of models using IASP (continental) and CRUST2 (oceanic) earth structure. Left: Observed (color) and modeled (black) GPS-displacements. Right: Slip distribution at the fault. IASP-model fits data effortlessly, whereas CRUST2-model slightly over predicts near field and under predicts far field displacements.

Plafker et al. [2007] suggested that a splay fault offshore northern Sumatra could be the secondary source responsible for the severe inundation which struck the Aceh province. In order to check this hypothesis, we performed an inversion based on following geometry. An additional splay fault connects to the 9th subfault layer of the reference geometry at 37 km depth and has a dip angle of 45°, which places the upper edge at around 105 km from the trench (model Sp845a). This corresponds approximately to splay faulting as suggested by Sibuet et al. [2007] for the Aceh basin. Figure 3.2 illustrates inversion results for slip and rake obtained from this model. Indeed we find surface slip on the splay fault around 4.5°N. Other significant patches of slip are located around 9°N and 13.5°N. However, we note that due to the relatively low number of measurements in the near field, these findings should be considered with care, hence it would be very desirable to have independent confirmation on splay faulting in the northern part of the rupture, e.g. from seismic, bathymetric or ROV surveys. Note also that slip on the main fault is only slightly changed by the presence of the splay fault (compare Figure 3.1and Figure 3.2). Detailed inundation modeling for Banda Aceh, assessing the effect of splay faulting will be published elsewhere.

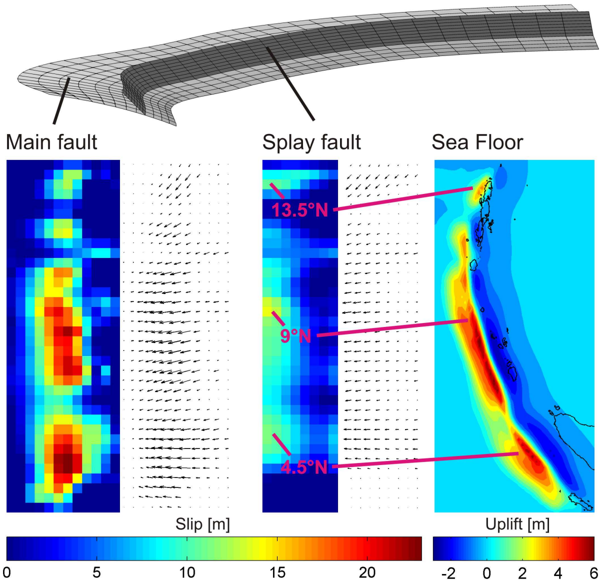

Figure 3.2 Top: Illustration of fault geometry seen from south-east. Left: Slip distribution obtained by model Sp845a consisting of a main fault and an additional splay fault, shown as rectangles for better visualization. Significant surface slip at the splay fault is found around 4.5°N, 9°N and 13.5°N. Right: Associated sea floor deformation in map view.

Next we use the inverted slip distribution to compute the corresponding sea floor deformation. We include the effect of horizontal displacements [Tanioka and Satake, 1996] into initial conditions for the tsunami-propagation model, but find it to be small in this case (see supplement). JASON1 satellite radar altimetry data (obtained from T. Schoene) provide an independent check for our inversion. Since run-up and inundation is not required here, relatively low resolution is sufficient to correctly reproduce the satellite data. Fast, robust and well-tested code TUNAMI-N2 by Imamura et al. [1997] with spatial and temporal resolution of 5 arcmin (ETOPO2) and 3 s respectively is used and takes less than 10 min of computation time on a single processor. Figure 3.3a shows the measured and modeled sea surface elevation along the JASON1 track approximately two hours after the earthquake. The CRUST2 model (magenta) clearly yields too small amplitudes of the leading waves in the south, whereas the IASP model (blue) performs quite well.

Figure 3.3b shows the models with splay faulting (using IASP crust). Model Sp260, in which the upper two subfault layers are assigned a fix dip angle of 60°, fits the JASON1 data slightly better than the model without splay fault, as it is able to better reproduce the splitting of the first wave, which is due to the two separated slip maxima, one offshore Aceh and one around the Nicobar islands (see discussion in Pietrzak et al. [2007]). The second model including splay faulting (Sp845a) results in a too pronounced first trough. All in all, our modeling implies that JASON1 data does not appear to be sufficient to deduce or to reject splay faulting.

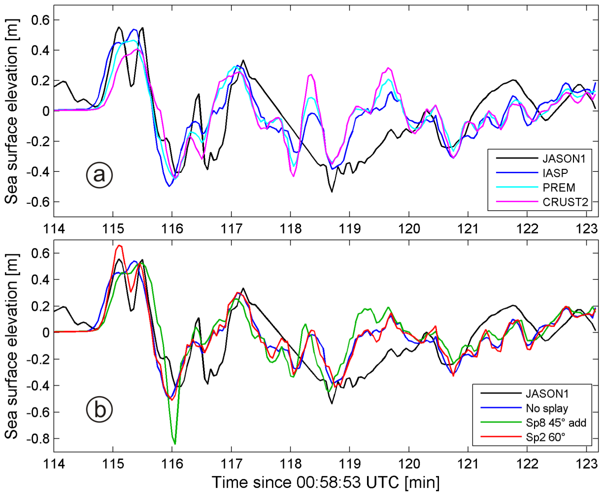

Figure 3.3 Observed and computed sea surface heights along JASON1 satellite track across the Indian Ocean from south-west to north-east approximately two hours after the event. IASP-model performs significantly better than CRUST2. Splay faulting slightly increases the splitting of the first wave.

3.6 Conclusions

Application of an accurate discretization of the subduction zone geometry and introduction of physical boundary conditions in the inversion process significantly enhances the quality of GPS based inversion, as is shown by checking against independent radar altimetry data. The discrepancy resulting from near- and far-field data, which is often attributed to postseismic effects, can largely be resolved by using a continental crustal structure. GPS and satellite altimetry data of offshore tsunami wave height are compatible with splay faulting in seaward direction with several meters of slip, but data are not sufficient to make stringent conclusions. Splay faulting, if present, is likely to be a second order effect in respect to magnitude of sea floor deformation and contribution to the tsunami, at least as recorded by JASON1 satellite.

3.7 Acknowledgments

This is publication no. 18 of the GITEWS project (German Indonesian Tsunami Early Warning System). The project is carried out through a large group of scientists and engineers from GeoForschungsZentrum Potsdam (GFZ) and its partners from DLR, AWI GKSS, IFM-GEOMAR, UNU, BGR, GTZ, as well as from Indonesian and other international partners. Funding is provided by the German Federal Ministry for Education and Research (BMBF), Grant 03TSU01. We thank R. Bürgmann for careful and constructive reviews.

4 Auxiliary Material for Paper: ‘Enhanced GPS inversion technique applied to the 2004 Sumatra Earthquake and Tsunami’

Andreas Hoechner[1], Andrey Y. Babeyko[1], Stephan V. Sobolev[1,2]
[1]Deutsches GeoForschungsZentrum GFZ, Potsdam, Germany
[2]Institute of Physics of the Earth, Moscow, Russia

4.1 Engdahl's relocations, modified RUM-geometry and fault zone discretization

The fault zone discretization is performed in the following way. Data from RUM-slabs by Gudmundsson and Sambridge [1998] is interpolated with a smooth surface and isolines are extracted at the desired depths. Note, however, that the zero-depth-line from RUM is assigned 5 km depth (approximately the depth of the trench), in accordance to the relocations by Engdahl et al. [2007] for Sumatra. The topmost line is divided into equally spaced segments. The next lower layers are constructed using bisectors. Length and width of each subfault are adjusted based on the surrounding subfaults, so that the edges intersect approximately at the midpoints.

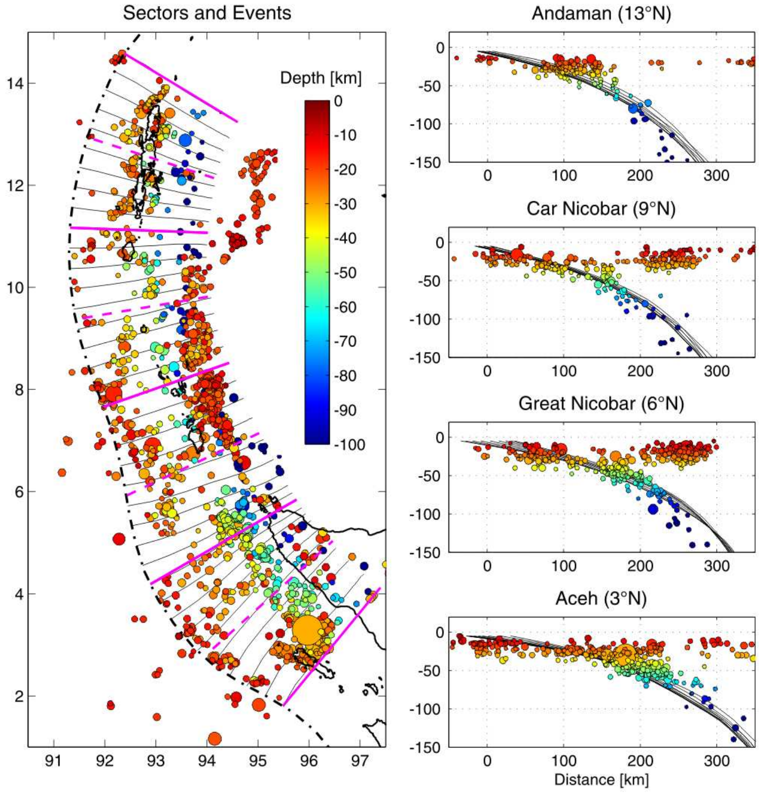

Figure 4.1 Circles: Relocated seismic events by Engdahl et al. [2007]. Size corresponds to magnitude and color to depth. Right side: Projection on profiles shown on the left side (magenta, dashed). Black lines: Fault profiles as used in this study (from 5 to 53 km depth).

4.2 GPS residuals for IASP, PREM, CRUST2

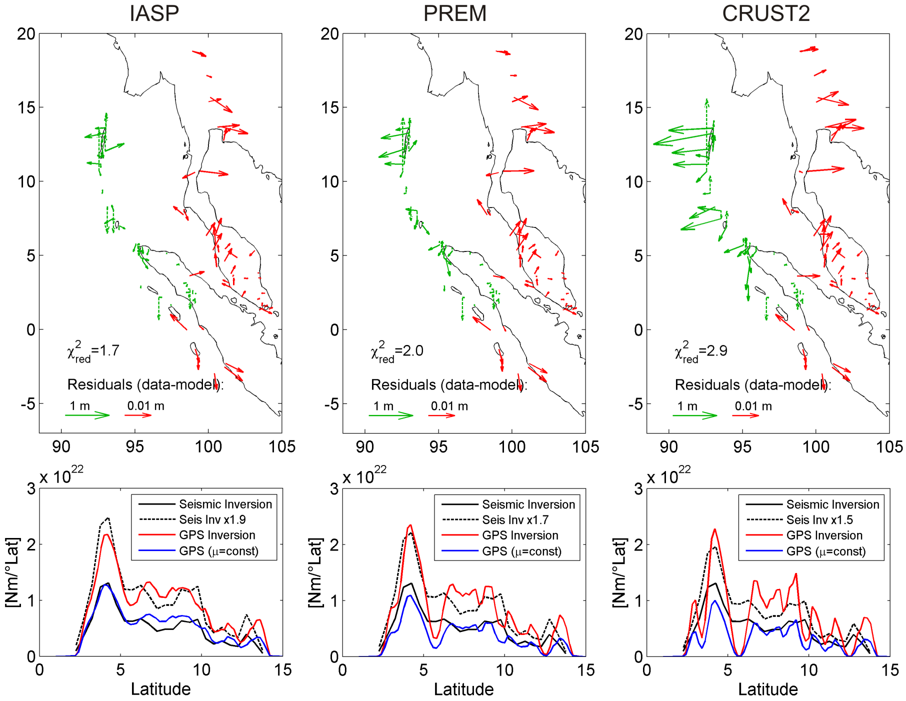

Figure 4.2 Top: Color: Observed GPS-vectors. Black: Modeled displacements for same fault geometry using different crustal models. Bottom: Plot comparing moment density (released energy per degree latitude) as determined by Ammon et al. [2005] with teleseismic methods (black solid) to geodetic inversion from this study (red: moment calculated using depth-dependent mu, blue: constant mu=30 GPa used for moment calculation (not for inversion). Dashed: seismic moment scaled with a factor to reproduce geodetic moment.

4.3 Inversions based on other geometries

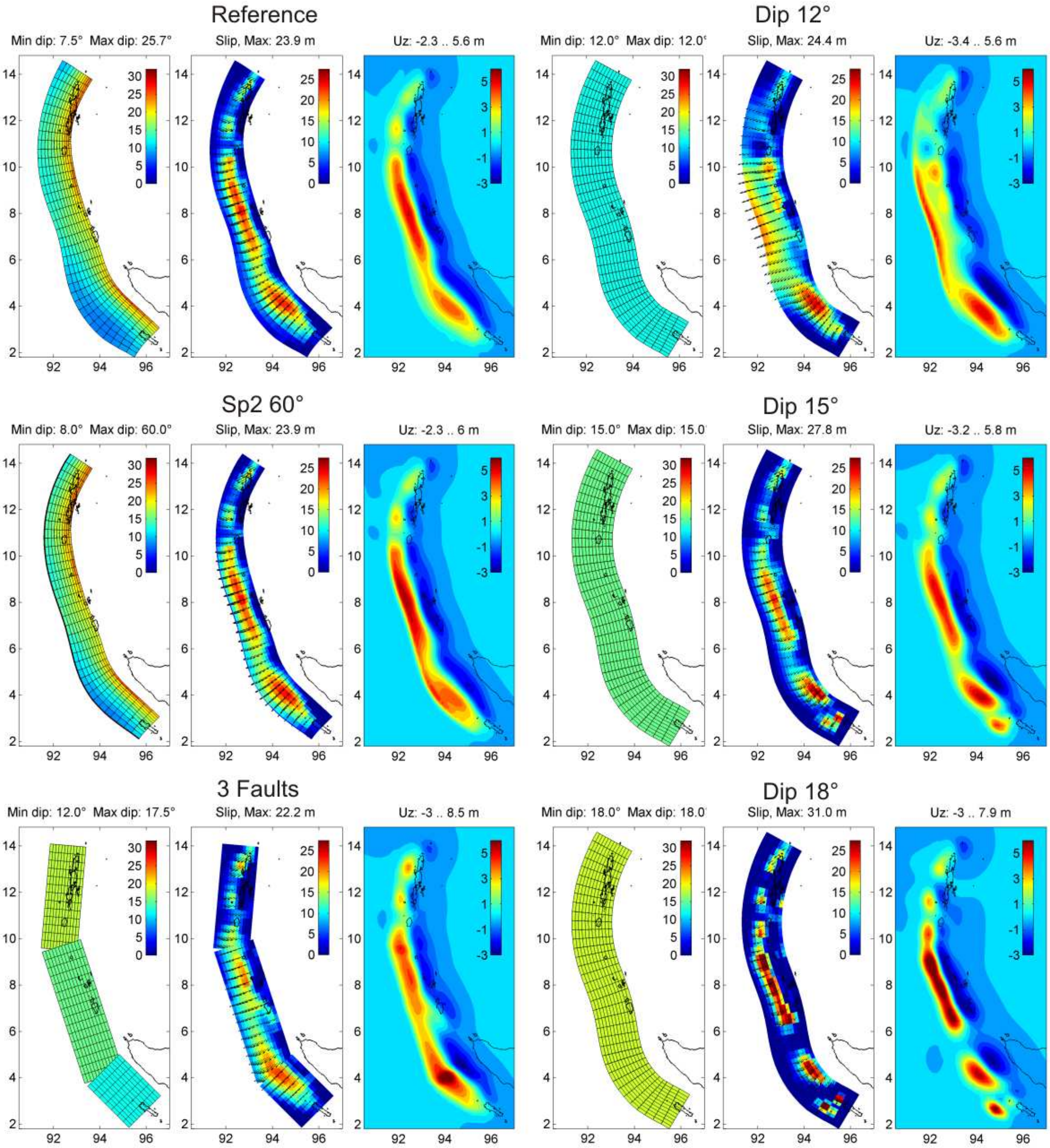

Figure 4.3 Dip angle, slip at the subduction interface and uplift of the seafloor obtained from different fault geometries using same crustal and inversion settings. Left: Top: Accurate fault geometry with dip varying between 7° and 26° used in this study. Middle: Uppermost two layers are assigned a fix dip angle of 60°. Bottom: Rectangular faults having dip angles of 12°, 15° and 17.5°, as commonly used. Right side: Constant dip angle of 12°, 15° and 18° used.

4.4 Effect of horizontal displacement and timing for tsunami modeling

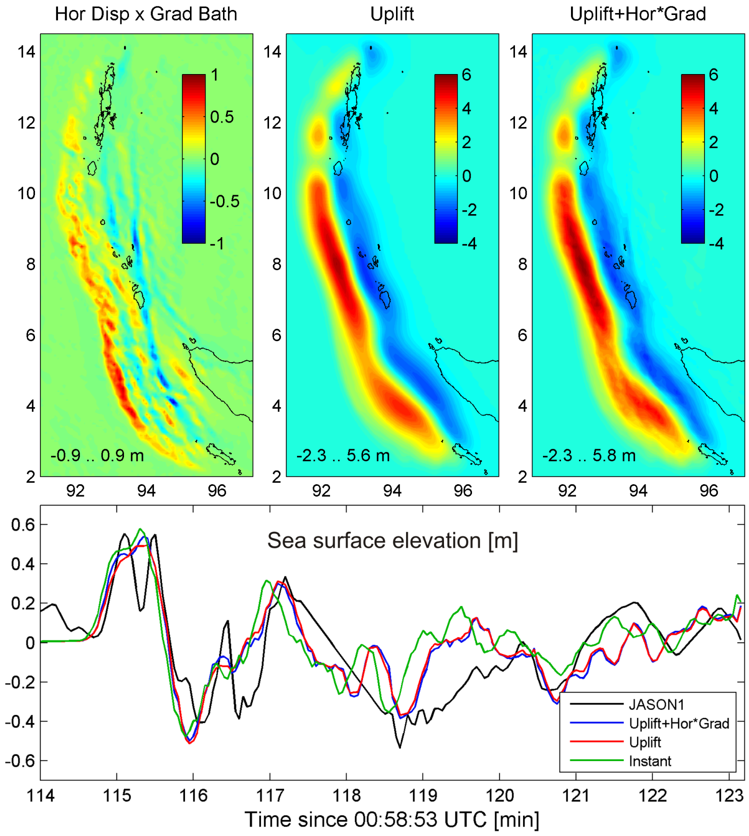

Figure 4.4 Left: Contribution to tsunamigenesis from horizontal displacements as formulated by Tanioka and Satake [1996] (horizontal displacement times gradient of bathymetry). Middle: Vertical sea floor displacement. Right: Total vertical displacement used as initial condition of tsunami. Bottom: Comparison to radar altimetry data by satellite JASON1, showing only a small effect from horizontal displacement for this event (tsunami energy increased from 6.5 to 7.1e15 J) and clearly observable influence of timing.

4.5 Earth layering models

The IASP velocities are from Kennett and Engdahl [1991], the density is from Kennett et al. [1995] (ak135). PREM is from Dziewonski and Anderson [1981]. The CRUST2 model [Bassin et al., 2000; Mooney et al., 1998] used here is as used by Chlieh et al. [2007], but continued below 346.5 km to a depth of 1400 km using PREM. Omission of this continuation leads to much higher inconsistency (~factor 2) between near- and far-field GPS-data. The lowermost layer is continued to infinity.

Table 4.1 IASP

#	D	Vp	Vs	rho
1	0.0	5.80	3.36	2720.0
2	20.0	5.80	3.36	2720.0
3	20.0	6.50	3.75	2920.0
4	35.0	6.50	3.75	2920.0
5	35.0	8.04	4.47	3320.0
6	120.0	8.05	4.50	3371.0
7	120.0	8.05	4.50	3371.0
8	210.0	8.30	4.52	3426.0
9	210.0	8.30	4.52	3426.0
10	410.0	9.03	4.87	3547.0
11	410.0	9.36	5.07	3756.0
12	660.0	10.20	5.60	4065.0
13	660.0	10.79	5.95	4371.0
14	760.0	11.06	6.21	4431.0
15	760.0	11.06	6.21	4431.0
16	1000.0	11.46	6.38	4569.8
17	1000.0	11.46	6.38	4569.8
18	1200.0	11.77	6.51	4683.9
19	1200.0	11.77	6.51	4683.9
20	1400.0	12.05	6.63	4795.1
21	1400.0	12.05	6.63	4795.1

Table 4.2 PREM

#	D	Vp	Vs	rho
1	0.0	1.45	0.00	1020.0
2	3.0	1.45	0.00	1020.0
3	3.0	5.80	3.20	2600.0
4	15.0	5.80	3.20	2600.0
5	15.0	6.80	3.90	2900.0
6	24.4	6.80	3.90	2900.0
7	24.4	8.11	4.49	3380.7
8	220.0	7.99	4.42	3359.5
9	220.0	8.56	4.64	3435.8
10	400.0	8.91	4.77	3543.3
11	400.0	9.13	4.93	3723.7
12	600.0	10.16	5.52	3975.8
13	600.0	10.16	5.52	3975.8
14	670.0	10.27	5.57	3992.1
15	670.0	10.75	5.95	4380.7
16	771.0	11.07	6.24	4443.2
17	771.0	11.07	6.24	4443.2
18	1000.0	11.46	6.40	4580.1
19	1000.0	11.46	6.40	4580.1
20	1200.0	11.78	6.52	4694.9
21	1200.0	11.78	6.52	4694.9
22	1400.0	12.06	6.63	4805.7

23	1400.0	12.06	6.63	4805.7

Table 4.3 CRUST2

#	D	Vp	Vs	rho
1	0.0	5.00	2.50	2600.0
2	1.7	5.00	2.50	2600.0
3	1.7	6.60	3.65	2900.0
4	4.0	6.60	3.65	2900.0
5	4.0	7.10	3.90	3050.0
6	6.5	7.10	3.90	3050.0
7	6.5	8.08	4.47	3375.4
8	202.5	8.08	4.47	3375.4
9	202.5	8.59	4.66	3446.5
10	238.5	8.59	4.66	3446.5
11	238.5	8.71	4.66	3489.5
12	346.5	8.71	4.66	3489.5
13	346.5	8.71	4.66	3489.5
14	400.0	8.91	4.77	3543.3
15	400.0	9.13	4.93	3723.7
16	600.0	10.16	5.52	3975.8
17	600.0	10.16	5.52	3975.8
18	670.0	10.27	5.57	3992.1
19	670.0	10.75	5.95	4380.7
20	771.0	11.07	6.24	4443.2
21	771.0	11.07	6.24	4443.2
22	1000.0	11.46	6.40	4580.1
23	1000.0	11.46	6.40	4580.1
24	1200.0	11.78	6.52	4694.9
25	1200.0	11.78	6.52	4694.9
26	1400.0	12.06	6.63	4805.7
27	1400.0	12.06	6.63	4805.7

4.6 GPS-data

GPS-data is from Banerjee et al. [2007], selected and modified as described in the main article.

```
chi2r =   1.695
rms   =   0.208 m
```

Table 4.4 Observed GPS displacements.

Observation:

Sta	lon	lat	ux	uy	uz	sx	sy	sz
EAST	93.05	13.63	-3.5519	-2.5492	0.9355	0.0327	0.0105	0.0467
ABAY	93.03	13.28	-3.7700	-2.7277	0.5755	0.0263	0.0080	0.0401
UGRH	92.77	12.22	-2.1400	-1.5073	-0.3494	0.0451	0.0158	0.1034
GOVI	92.98	12.04	-1.3078	-0.6196	0.0508	0.0465	0.0168	0.1526
PORT	92.72	11.65	-2.8568	-0.8792	-0.8696	0.0086	0.0044	0.0182
PASG	92.68	11.18	-2.7039	-1.0313	-0.7346	0.0214	0.0101	0.0423
RAMK	92.57	10.70	-3.0830	-2.5648	0.1705	0.0139	0.0062	0.0562
CARN	92.80	9.22	-5.5943	-2.8444	-1.1110	0.0060	0.0030	0.0120
TERE	93.12	8.30	-5.6470	-3.1458	-2.7696	0.0185	0.0082	0.0386
KARD	93.55	8.04	-3.9753	-1.7205	-1.2600	0.0280	0.0079	0.0407
MERO	93.54	7.51	-4.9094	-2.8498	-2.1291	0.0241	0.0085	0.0437
CAMP	93.93	7.00	-3.9708	-2.3189	-1.4398	0.0111	0.0066	0.0194
BM12	98.94	2.64	-0.0785	-0.0224	-0.0805	0.0666	0.0238	0.0733
D962	97.45	1.69	-0.0303	-0.0261	-0.0535	0.0649	0.0253	0.0558
D972	96.62	2.17	0.0118	-0.0213	-0.5714	0.0669	0.0649	0.0669
JAHE	98.51	3.15	-0.1880	-0.0248	0.0053	0.0093	0.0882	0.0899
MART	98.68	2.52	-0.1351	-0.0150	-0.1228	0.0414	0.0240	0.0869
NIND	98.75	2.73	-0.1200	-0.0092	-0.4546	0.0326	0.0230	0.0916
PAND	98.82	1.68	-0.0359	-0.0367	-0.0264	0.0418	0.0397	0.0277
PISU	99.15	2.45	-0.0733	-0.0167	-0.0129	0.0277	0.0311	0.0617
SIPA	99.09	2.10	-0.0954	-0.0606	-0.1144	0.0662	0.0631	0.0699
TIGA	98.56	2.92	-0.1297	-0.0069	0.0452	0.0228	0.0236	0.0305
K504	95.24	5.43	-1.8514	-1.7419	-0.1717	0.1057	0.0882	0.0597
K505	95.27	5.48	-1.8014	-1.7223	-0.0611	0.1034	0.0873	0.0807
K515	95.49	5.57	-1.4279	-1.3178	-0.0462	0.0830	0.0671	0.0637
LANG	98.00	4.43	-0.3330	-0.1015	-0.0119	0.0411	0.0426	0.0608
LHOK	97.16	5.09	-0.5126	-0.2179	0.0765	0.0434	0.0478	0.1054
PIDI	95.93	5.33	-1.2542	-0.9440	0.0354	0.0405	0.0388	0.0490
R171	95.39	2.96	-3.8165	-4.3094	2.0988	0.0191	0.2161	0.0458
R173	95.52	4.61	-2.7440	-2.3525	-0.6010	0.1427	0.1188	0.0420
R174	95.37	4.84	-2.6288	-2.3894	-0.5838	0.1386	0.1200	0.0841
R175	95.20	5.24	-2.2079	-2.0578	-0.2266	0.1217	0.1038	0.1211
R176	95.06	5.71	-1.8049	-1.6644	-0.1421	0.1087	0.0855	0.0908
ABGS	99.39	0.22	-0.0042	-0.0051	null	0.0037	0.0023	null
ARAU	100.28	6.45	-0.1303	-0.0338	null	0.0091	0.0040	null
BNKK	100.61	13.67	-0.0609	-0.0425	null	0.0043	0.0026	null
CHMI	98.97	18.77	-0.0158	-0.0249	null	0.0049	0.0030	null
CMU	98.90	18.80	-0.0140	-0.0258	null	0.0070	0.0039	null
CPN	99.40	10.70	-0.1274	-0.0675	null	0.0044	0.0025	null
KMI	100.80	13.70	-0.0564	-0.0443	null	0.0051	0.0031	null
KUAL	103.14	5.32	-0.0567	-0.0056	null	0.0077	0.0041	null
LNGG	101.16	-2.29	0.0055	-0.0040	null	0.0043	0.0025	null
MKMK	101.09	-2.54	0.0061	-0.0059	null	0.0044	0.0025	null
MSAI	99.09	-1.33	0.0029	-0.0085	null	0.0036	0.0023	null
NGNG	99.27	-1.80	0.0016	-0.0079	null	0.0040	0.0024	null
NTUS	103.68	1.35	-0.0146	0.0017	null	0.0032	0.0022	null
PBAI	98.53	-0.03	-0.0063	-0.0007	null	0.0182	0.0047	null
PHKT	98.31	8.11	-0.2393	-0.1077	null	0.0046	0.0026	null
PRKB	100.40	-2.97	0.0013	-0.0072	null	0.0043	0.0024	null
SAMP	98.72	3.62	-0.1325	-0.0191	null	0.0054	0.0025	null
SIS2	99.87	17.16	-0.0304	-0.0321	null	0.0042	0.0026	null
BEHR	101.52	3.77	-0.0559	0.0023	null	0.0028	0.0019	null
KUAN	103.35	3.83	-0.0392	0.0011	null	0.0037	0.0022	null
USMP	100.30	5.36	-0.1151	-0.0144	null	0.0048	0.0029	null
UTMJ	103.64	1.57	-0.0195	0.0046	null	0.0037	0.0022	null

BANT	101.54	2.83	-0.0450	0.0035	null	0.0039	0.0025	null
GMUS	101.96	4.86	-0.0705	-0.0024	null	0.0046	0.0030	null
GRIK	101.13	5.44	-0.0909	-0.0109	null	0.0037	0.0026	null
JHJY	103.80	1.54	-0.0179	0.0038	null	0.0039	0.0024	null
JUIP	101.09	4.60	-0.0775	-0.0019	null	0.0036	0.0025	null
JUML	102.26	2.21	-0.0277	0.0052	null	0.0038	0.0024	null
KKBH	101.66	3.56	-0.0521	0.0010	null	0.0040	0.0027	null
KLUG	103.32	2.03	-0.0229	0.0036	null	0.0041	0.0025	null
KUKP	103.45	1.33	-0.0170	0.0038	null	0.0042	0.0025	null
LGKW	99.85	6.33	-0.1489	-0.0350	null	0.0035	0.0027	null
MERS	103.83	2.45	-0.0267	0.0031	null	0.0044	0.0026	null
MERU	101.41	3.14	-0.0504	0.0023	null	0.0040	0.0026	null
PEKN	103.39	3.49	-0.0352	0.0017	null	0.0041	0.0026	null
PUPK	100.56	4.21	-0.0856	-0.0018	null	0.0040	0.0025	null
SELM	100.70	5.22	-0.1023	-0.0120	null	0.0035	0.0025	null
SGPT	100.49	5.64	-0.1164	-0.0140	null	0.0035	0.0026	null
TGPG	104.11	1.37	-0.0162	0.0038	null	0.0040	0.0023	null
TLOH	102.42	3.45	-0.0415	0.0015	null	0.0046	0.0032	null
UPMS	101.72	2.99	-0.0426	0.0045	null	0.0044	0.0028	null
UUMK	100.51	6.46	-0.1225	-0.0231	null	0.0043	0.0031	null
BANH	99.08	10.61	-0.1551	-0.0748	null	0.0040	0.0024	null
CHON	101.05	13.12	-0.0684	-0.0384	null	0.0027	0.0020	null
NAKH	100.12	15.67	-0.0394	-0.0440	null	0.0041	0.0027	null
PHUK	98.30	7.76	-0.2525	-0.1019	null	0.0025	0.0019	null
RYNG	101.03	12.76	-0.0743	-0.0371	null	0.0024	0.0018	null
UTHA	100.01	15.38	-0.0471	-0.0395	null	0.0024	0.0019	null

Table 4.5 Modeled GPS displacements.

Model: (IASP, no splay fault)

Sta	lon	lat	ux	uy	uz
EAST	93.05	13.63	-3.2990	-2.5315	0.6027
ABAY	93.03	13.28	-3.2883	-2.6262	0.1613
UGRH	92.77	12.22	-2.1634	-1.2910	-0.5739
GOVI	92.98	12.04	-1.7349	-0.7938	-0.3243
PORT	92.72	11.65	-2.7641	-0.9147	-0.9701
PASG	92.68	11.18	-2.3875	-1.0580	-0.6537
RAMK	92.57	10.70	-3.1174	-2.4602	-0.7635
CARN	92.80	9.22	-5.5760	-2.8394	-1.1819
TERE	93.12	8.30	-5.6495	-3.0796	-2.1645
KARD	93.55	8.04	-3.9330	-1.8393	-0.9785
MERO	93.54	7.51	-4.7073	-2.7296	-1.8008
CAMP	93.93	7.00	-4.1056	-2.2482	-1.3479
BM12	98.94	2.64	-0.0695	-0.0058	-0.0012
D962	97.45	1.69	-0.0225	-0.0135	-0.0234
D972	96.62	2.17	-0.0601	-0.0172	-0.0609
JAHE	98.51	3.15	-0.1178	-0.0152	0.0030
MART	98.68	2.52	-0.0685	-0.0068	-0.0034
NIND	98.75	2.73	-0.0792	-0.0077	-0.0011
PAND	98.82	1.68	-0.0294	-0.0049	-0.0077
PISU	99.15	2.45	-0.0568	-0.0038	-0.0020
SIPA	99.09	2.10	-0.0434	-0.0035	-0.0044
TIGA	98.56	2.92	-0.0982	-0.0112	0.0002
K504	95.24	5.43	-1.9191	-1.6824	-0.2203
K505	95.27	5.48	-1.8034	-1.5600	-0.1738
K515	95.49	5.57	-1.4496	-1.1641	-0.0498
LANG	98.00	4.43	-0.2764	-0.0775	0.0270
LHOK	97.16	5.09	-0.5135	-0.2285	0.0498
PIDI	95.93	5.33	-1.2146	-0.8487	0.0042
R171	95.39	2.96	-3.8162	-4.2541	2.0978
R173	95.52	4.61	-2.8627	-2.1847	-0.6478
R174	95.37	4.84	-2.8217	-2.3309	-0.6253
R175	95.20	5.24	-2.3348	-2.0849	-0.4058
R176	95.06	5.71	-1.7450	-1.5120	-0.1677
ABGS	99.39	0.22	-0.0058	-0.0038	null
ARAU	100.28	6.45	-0.1335	-0.0326	null
BNKK	100.61	13.67	-0.0693	-0.0433	null
CHMI	98.97	18.77	-0.0195	-0.0240	null

```
  CMU   98.90   18.80  -0.0192 -0.0239    null
  CPN   99.40   10.70  -0.1381 -0.0662    null
  KMI  100.80   13.70  -0.0669 -0.0416    null
 KUAL  103.14    5.32  -0.0547 -0.0036    null
 LNGG  101.16   -2.29  -0.0011 -0.0007    null
 MKMK  101.09   -2.54  -0.0007 -0.0007    null
 MSAI   99.09   -1.33   0.0013 -0.0036    null
 NGNG   99.27   -1.80   0.0013 -0.0028    null
 NTUS  103.68    1.35  -0.0181  0.0032    null
 PBAI   98.53   -0.03  -0.0001 -0.0065    null
 PHKT   98.31    8.11  -0.2410 -0.1036    null
 PRKB  100.40   -2.97   0.0005 -0.0011    null
 SAMP   98.72    3.62  -0.1380 -0.0206    null
 SIS2   99.87   17.16  -0.0323 -0.0314    null
 BEHR  101.52    3.77  -0.0576 -0.0007    null
 KUAN  103.35    3.83  -0.0395  0.0012    null
 USMP  100.30    5.36  -0.1185 -0.0207    null
 UTMJ  103.64    1.57  -0.0196  0.0033    null
 BANT  101.54    2.83  -0.0415  0.0020    null
 GMUS  101.96    4.86  -0.0671 -0.0046    null
 GRIK  101.13    5.44  -0.0928 -0.0129    null
 JHJY  103.80    1.54  -0.0191  0.0032    null
 JUIP  101.09    4.60  -0.0802 -0.0068    null
 JUML  102.26    2.21  -0.0290  0.0030    null
 KKBH  101.66    3.56  -0.0523  0.0003    null
 KLUG  103.32    2.03  -0.0237  0.0033    null
 KUKP  103.45    1.33  -0.0183  0.0032    null
 LGKW   99.85    6.33  -0.1521 -0.0399    null
 MERS  103.83    2.45  -0.0253  0.0030    null
 MERU  101.41    3.14  -0.0479  0.0012    null
 PEKN  103.39    3.49  -0.0361  0.0019    null
 PUPK  100.56    4.21  -0.0850 -0.0070    null
 SELM  100.70    5.22  -0.1019 -0.0147    null
 SGPT  100.49    5.64  -0.1159 -0.0212    null
 TGPG  104.11    1.37  -0.0175  0.0032    null
 TLOH  102.42    3.45  -0.0430  0.0015    null
 UPMS  101.72    2.99  -0.0426  0.0019    null
 UUMK  100.51    6.46  -0.1245 -0.0290    null
 BANH   99.08   10.61  -0.1503 -0.0726    null
 CHON  101.05   13.12  -0.0709 -0.0409    null
 NAKH  100.12   15.67  -0.0476 -0.0384    null
 PHUK   98.30    7.76  -0.2487 -0.1050    null
 RYNG  101.03   12.76  -0.0752 -0.0417    null
 UTHA  100.01   15.38  -0.0518 -0.0406    null
```

4.7 Subfault-parameters for reference model (IASP, no splay fault)

Table 4.6 Model parameterization.

```
Mw = 9.30    Mo = 1.13e+023 Nm (layered)
Mw = 9.15    Mo = 6.71e+022 Nm (with mu=30GPa)

Smean  =  8.21 m
Smax   = 23.90 m
Uxymax = 11.99 m
Uzmax  =  5.64 m

Col. 1   : subfault number
Col. 2- 4: longitude, latitude, depth of upper southern corner
Col. 5- 6: strike and dip angle
Col. 7- 8: length and width [km]
Col. 9-10: magnitude [m] and rake angle of slip

Nr   lon      lat   dep  str   dip   len   wid   sli   rak
  1  95.487  1.800  5.0 300.9  9.9  45.1  23.2  0.25  74.3
  2  95.588  1.968  9.0 303.8  9.9  45.7  23.2  0.02  77.0
  3  95.696  2.130 13.0 307.0 10.8  46.2  21.4  0.15  80.3
  4  95.803  2.272 17.0 310.1 12.1  46.5  19.1  1.76  83.6
  5  95.906  2.394 21.0 312.6 13.0  46.7  17.8  3.41  85.9
  6  96.008  2.505 25.0 313.9 14.2  46.8  16.3  4.56  87.0
  7  96.104  2.605 29.0 314.9 15.5  46.9  14.9  2.73  88.5
  8  96.195  2.695 33.0 315.4 16.8  46.9  13.9  0.01  90.3
  9  96.280  2.779 37.0 315.4 18.5  47.0  12.6  0.00  91.4
 10  96.358  2.856 41.0 315.0 18.7  47.0  12.5  0.00  91.4
 11  96.434  2.932 45.0 314.7 20.4  47.1  11.4  0.01  91.6
 12  96.503  3.002 49.0 314.1 21.9  47.2  10.7  0.00  91.3
 13  95.144  2.006  5.0 297.6  8.9  43.8  25.9  0.01  70.9
 14  95.249  2.195  9.0 301.6  9.0  44.2  25.7  1.50  74.8
 15  95.367  2.378 13.0 304.6  9.5  44.4  24.3  6.08  78.0
 16  95.484  2.541 17.0 308.8 10.8  45.0  21.3  8.95  82.4
 17  95.597  2.678 21.0 311.9 12.3  45.4  18.8 11.09  85.4
 18  95.705  2.797 25.0 313.3 13.5  45.7  17.1 12.21  86.9
 19  95.806  2.902 29.0 314.3 15.2  45.9  15.3  7.90  88.6
 20  95.898  2.996 33.0 314.7 16.7  46.1  13.9  0.93  90.1
 21  95.983  3.080 37.0 314.8 18.9  46.3  12.3  0.01  91.1
 22  96.058  3.155 41.0 314.5 19.2  46.5  12.2  0.01  91.1
 23  96.132  3.230 45.0 314.0 21.4  46.6  11.0  0.00  91.2
 24  96.198  3.298 49.0 313.5 23.3  46.7  10.1  0.00  90.9
 25  94.789  2.192  5.0 300.4  8.1  43.6  28.4  0.16  73.3
 26  94.907  2.405  9.0 303.2  8.2  42.5  27.9  2.92  76.3
 27  95.035  2.607 13.0 306.2  8.6  41.8  26.8  7.87  79.5
 28  95.169  2.795 17.0 308.8  9.9  41.2  23.4 11.26  82.5
 29  95.293  2.950 21.0 311.2 11.7  41.3  19.7 13.63  85.5
 30  95.407  3.078 25.0 312.2 12.9  41.5  17.9 15.73  87.2
 31  95.511  3.191 29.0 313.2 14.9  41.8  15.5 12.51  88.7
 32  95.604  3.287 33.0 313.5 16.5  42.1  14.1  6.01  89.7
 33  95.688  3.374 37.0 313.9 19.3  42.3  12.1  0.41  90.6
 34  95.760  3.448 41.0 313.7 19.7  42.5  11.9  0.02  90.9
 35  95.831  3.521 45.0 313.3 22.0  42.7  10.7  0.01  90.9
 36  95.893  3.587 49.0 313.0 24.4  42.8   9.7  0.01  91.0
 37  94.444  2.394  5.0 303.7  7.7  42.2  30.0  2.21  76.6
 38  94.583  2.617  9.0 305.3  7.7  39.7  29.9  3.69  78.2
 39  94.729  2.831 13.0 307.8  8.1  38.3  28.4  7.37  81.0
 40  94.877  3.028 17.0 309.8  9.4  37.6  24.5 11.19  83.5
 41  95.014  3.195 21.0 310.8 11.3  37.5  20.4 14.67  85.4
 42  95.130  3.329 25.0 311.7 12.5  37.6  18.5 17.44  87.2
 43  95.237  3.448 29.0 312.5 14.9  37.7  15.6 17.02  88.7
 44  95.330  3.548 33.0 312.3 16.1  37.9  14.4 13.58  89.3
 45  95.414  3.638 37.0 312.9 19.7  38.0  11.9  8.23  90.5
 46  95.484  3.712 41.0 312.5 20.0  38.1  11.7  4.76  90.5
 47  95.552  3.785 45.0 312.3 22.0  38.2  10.7  1.42  90.6
```

48	95.612	3.849	49.0	312.6	25.3	38.2	9.4	0.16	91.0
49	94.111	2.617	5.0	312.2	7.6	43.0	30.4	1.37	84.7
50	94.279	2.832	9.0	311.8	7.5	39.6	30.5	3.88	84.4
51	94.450	3.047	13.0	311.3	8.0	36.8	28.9	8.33	84.2
52	94.615	3.247	17.0	311.0	9.3	35.2	24.8	13.08	84.5
53	94.758	3.415	21.0	310.6	11.0	34.3	20.9	17.31	85.0
54	94.878	3.554	25.0	311.3	12.2	33.9	18.9	20.49	86.8
55	94.987	3.677	29.0	312.0	15.0	33.8	15.5	21.12	88.6
56	95.078	3.777	33.0	311.9	15.5	33.6	14.9	19.23	89.4
57	95.163	3.871	37.0	313.0	20.0	33.5	11.7	14.13	91.0
58	95.230	3.944	41.0	312.8	20.0	33.4	11.7	8.93	91.5
59	95.297	4.017	45.0	313.0	21.5	33.3	10.9	3.63	91.8
60	95.358	4.083	49.0	313.5	25.7	33.3	9.2	0.49	92.6
61	93.814	2.886	5.0	317.7	7.7	43.4	29.8	2.18	89.6
62	94.005	3.077	9.0	316.5	7.7	41.1	30.0	4.91	88.5
63	94.194	3.272	13.0	315.3	8.0	39.2	28.6	9.80	87.7
64	94.371	3.459	17.0	314.6	9.4	37.8	24.5	15.11	87.6
65	94.520	3.620	21.0	314.2	11.0	36.8	20.9	19.61	88.0
66	94.646	3.758	25.0	313.6	12.0	36.0	19.2	22.58	88.4
67	94.759	3.882	29.0	313.9	15.0	35.5	15.4	22.88	90.0
68	94.851	3.980	33.0	313.9	15.1	35.0	15.3	20.81	91.2
69	94.941	4.078	37.0	314.2	20.2	34.6	11.6	15.94	92.3
70	95.009	4.149	41.0	313.9	20.3	34.2	11.5	10.05	92.8
71	95.077	4.221	45.0	313.3	21.0	33.5	11.2	4.67	92.5
72	95.141	4.289	49.0	313.7	25.6	33.1	9.3	2.08	93.1
73	93.545	3.182	5.0	321.9	8.0	43.2	28.7	3.07	92.6
74	93.745	3.351	9.0	320.1	8.0	40.7	28.8	5.86	91.4
75	93.942	3.527	13.0	317.9	8.3	38.0	27.8	10.84	89.5
76	94.126	3.701	17.0	316.4	9.5	36.0	24.2	16.44	88.6
77	94.280	3.853	21.0	315.8	11.3	34.5	20.3	20.66	88.9
78	94.410	3.982	25.0	314.4	11.9	32.9	19.4	22.78	88.3
79	94.528	4.105	29.0	314.9	14.8	31.9	15.6	22.49	90.2
80	94.622	4.201	33.0	315.6	14.9	31.0	15.6	20.19	92.4
81	94.716	4.296	37.0	316.2	20.0	30.4	11.7	16.09	93.9
82	94.786	4.365	41.0	317.0	19.6	29.9	11.9	11.20	95.5
83	94.854	4.432	45.0	319.3	20.8	29.5	11.2	7.01	98.0
84	94.923	4.498	49.0	319.0	25.1	29.0	9.4	4.76	97.6
85	93.297	3.497	5.0	327.2	8.3	43.2	27.7	3.70	97.2
86	93.501	3.642	9.0	326.2	8.3	40.8	27.8	6.53	96.4
87	93.702	3.793	13.0	325.4	8.6	38.4	26.7	11.47	96.0
88	93.893	3.944	17.0	323.2	9.7	35.9	23.8	16.56	94.3
89	94.057	4.082	21.0	322.3	11.6	34.0	19.9	20.36	94.1
90	94.190	4.198	25.0	322.4	12.0	32.6	19.2	22.18	95.0
91	94.319	4.313	29.0	320.8	14.5	30.9	16.0	21.24	94.9
92	94.422	4.405	33.0	321.5	15.1	29.8	15.3	18.81	97.0
93	94.524	4.496	37.0	319.9	19.3	28.8	12.1	14.99	96.4
94	94.600	4.564	41.0	320.6	18.9	28.0	12.4	11.24	98.0
95	94.680	4.634	45.0	320.1	21.4	27.2	11.0	7.46	97.9
96	94.751	4.695	49.0	319.2	24.5	26.5	9.7	4.96	97.0
97	93.080	3.833	5.0	332.7	8.6	43.5	26.7	5.10	101.6
98	93.292	3.956	9.0	331.0	8.5	41.3	26.9	6.97	100.0
99	93.501	4.084	13.0	329.1	9.1	39.2	25.2	11.06	98.5
100	93.696	4.209	17.0	326.9	10.0	37.3	23.0	15.93	96.7
101	93.867	4.328	21.0	325.4	11.8	35.6	19.6	19.28	95.9
102	94.009	4.432	25.0	324.3	12.5	34.0	18.5	20.58	95.6
103	94.142	4.531	29.0	323.2	14.2	32.7	16.3	19.31	95.9
104	94.252	4.618	33.0	323.8	15.7	31.6	14.8	16.53	97.8
105	94.356	4.696	37.0	323.1	18.6	30.7	12.6	12.74	98.1
106	94.437	4.761	41.0	324.3	18.5	29.8	12.6	9.01	100.1
107	94.520	4.825	45.0	325.8	21.5	29.3	10.9	5.87	101.7
108	94.592	4.879	49.0	326.4	23.1	28.7	10.2	3.51	102.2
109	92.896	4.189	5.0	336.8	9.0	43.3	25.5	4.94	104.5
110	93.107	4.288	9.0	335.0	8.9	40.8	25.9	6.79	102.8
111	93.316	4.395	13.0	334.1	9.6	38.8	24.0	10.53	102.1
112	93.507	4.498	17.0	332.7	10.5	36.8	21.9	14.91	101.1
113	93.680	4.599	21.0	330.5	11.8	34.7	19.6	17.75	99.5
114	93.824	4.689	25.0	331.7	12.9	33.4	17.9	18.52	101.5
115	93.960	4.774	29.0	330.6	14.3	31.9	16.2	16.97	101.6

116	94.080	4.853	33.0	329.6	16.1	30.5	14.5	13.66	101.8
117	94.186	4.922	37.0	329.1	17.9	29.4	13.0	9.25	102.3
118	94.278	4.984	41.0	329.6	18.7	28.4	12.5	5.63	103.3
119	94.371	5.044	45.0	327.4	21.0	27.2	11.2	2.92	101.5
120	94.448	5.095	49.0	327.9	21.4	26.4	10.9	1.41	102.2
121	92.739	4.557	5.0	342.3	9.3	43.5	24.8	4.65	108.5
122	92.946	4.634	9.0	342.2	9.3	41.8	24.8	6.46	108.6
123	93.158	4.718	13.0	339.7	10.0	39.7	23.0	10.20	106.3
124	93.351	4.800	17.0	337.8	11.1	38.2	20.7	13.90	104.8
125	93.522	4.879	21.0	336.3	11.9	36.8	19.4	16.27	103.8
126	93.679	4.958	25.0	334.5	13.4	35.2	17.3	16.50	102.9
127	93.817	5.027	29.0	333.6	14.8	34.2	15.7	14.46	103.1
128	93.940	5.092	33.0	332.9	16.4	33.2	14.2	10.42	103.4
129	94.048	5.152	37.0	332.4	17.6	32.3	13.3	5.78	103.8
130	94.146	5.207	41.0	332.9	18.8	31.4	12.4	2.07	104.9
131	94.236	5.256	45.0	334.6	20.5	30.8	11.4	0.63	106.6
132	94.319	5.302	49.0	335.3	20.6	29.9	11.4	0.03	107.7
133	92.617	4.939	5.0	347.0	9.6	44.1	23.9	4.58	111.9
134	92.830	4.997	9.0	344.7	10.0	42.7	23.0	6.30	109.6
135	93.033	5.057	13.0	342.2	10.7	41.6	21.6	9.75	107.4
136	93.220	5.122	17.0	340.3	11.6	40.5	19.9	13.19	105.9
137	93.387	5.186	21.0	339.4	12.5	39.6	18.5	15.36	105.7
138	93.541	5.249	25.0	338.3	13.6	38.6	17.0	15.32	105.4
139	93.677	5.308	29.0	338.0	15.0	37.7	15.5	12.93	106.1
140	93.800	5.364	33.0	338.0	16.8	36.8	13.9	8.52	107.0
141	93.911	5.414	37.0	337.3	17.2	35.8	13.5	3.64	107.1
142	94.015	5.463	41.0	337.7	18.1	34.9	12.9	0.55	107.9
143	94.116	5.509	45.0	337.8	20.0	34.0	11.7	0.17	108.5
144	94.205	5.549	49.0	338.3	20.3	33.3	11.5	0.19	108.9
145	92.527	5.329	5.0	348.9	10.4	44.1	22.3	4.69	112.3
146	92.727	5.371	9.0	346.9	10.7	43.5	21.6	6.32	110.4
147	92.917	5.419	13.0	345.7	11.3	43.0	20.3	9.71	109.3
148	93.095	5.471	17.0	343.9	12.0	42.3	19.2	13.24	108.0
149	93.260	5.524	21.0	342.8	13.0	41.8	17.8	15.46	107.5
150	93.410	5.575	25.0	341.8	14.1	41.2	16.5	15.66	107.4
151	93.549	5.626	29.0	340.6	15.0	40.7	15.4	13.61	107.3
152	93.676	5.674	33.0	340.4	16.7	40.3	13.9	9.57	108.0
153	93.785	5.715	37.0	341.2	17.2	40.0	13.5	4.91	109.6
154	93.895	5.757	41.0	341.0	17.7	39.5	13.2	1.65	110.0
155	93.999	5.796	45.0	341.7	19.1	39.2	12.2	0.48	110.8
156	94.093	5.831	49.0	342.8	19.8	38.9	11.8	0.12	111.9
157	92.450	5.722	5.0	350.6	11.2	44.7	20.7	4.73	112.4
158	92.638	5.755	9.0	348.5	11.4	44.6	20.3	6.39	110.4
159	92.821	5.795	13.0	346.1	12.1	44.4	19.0	9.71	108.2
160	92.989	5.838	17.0	344.4	12.7	44.4	18.2	13.70	106.9
161	93.148	5.883	21.0	342.7	13.5	44.4	17.1	16.51	105.9
162	93.294	5.928	25.0	341.9	14.7	44.5	15.8	17.48	106.1
163	93.427	5.972	29.0	341.1	15.2	44.5	15.2	16.48	106.5
164	93.553	6.016	33.0	340.8	16.0	44.6	14.5	13.44	107.2
165	93.669	6.057	37.0	341.6	17.3	44.8	13.5	9.88	108.8
166	93.779	6.094	41.0	341.5	17.6	45.1	13.2	6.88	109.4
167	93.888	6.130	45.0	341.2	18.2	45.2	12.8	4.26	109.3
168	93.990	6.165	49.0	341.7	18.9	45.5	12.3	1.61	109.6
169	92.385	6.117	5.0	349.0	12.0	44.8	19.3	4.22	109.3
170	92.558	6.148	9.0	347.6	12.4	45.3	18.6	6.35	107.9
171	92.724	6.183	13.0	345.6	13.0	45.6	17.8	9.95	106.2
172	92.881	6.223	17.0	344.1	13.7	45.9	16.9	14.37	105.0
173	93.029	6.265	21.0	342.5	14.2	46.0	16.3	17.67	104.1
174	93.170	6.309	25.0	341.0	15.1	46.0	15.3	19.38	103.7
175	93.298	6.351	29.0	340.7	15.7	46.2	14.8	19.09	104.6
176	93.422	6.394	33.0	339.9	16.2	46.4	14.4	16.83	105.1
177	93.542	6.437	37.0	338.9	17.1	46.5	13.6	13.31	105.0
178	93.651	6.476	41.0	339.3	17.7	47.0	13.2	9.58	105.9
179	93.757	6.514	45.0	339.5	18.3	47.5	12.8	6.05	106.3
180	93.862	6.551	49.0	339.0	18.7	47.8	12.5	2.51	105.7
181	92.309	6.510	5.0	346.6	12.5	44.8	18.5	3.78	105.5
182	92.470	6.545	9.0	346.1	13.3	45.7	17.4	6.06	104.9
183	92.623	6.580	13.0	344.8	14.0	46.3	16.5	10.06	103.8

184	92.768	6.619	17.0	343.0	14.5	46.6	15.9	14.92	102.3
185	92.905	6.659	21.0	342.0	15.2	46.9	15.3	18.75	102.0
186	93.035	6.701	25.0	341.1	15.7	46.9	14.8	20.97	102.2
187	93.160	6.744	29.0	339.8	16.4	46.7	14.2	20.74	102.3
188	93.278	6.786	33.0	339.2	16.9	46.7	13.8	17.88	103.0
189	93.391	6.828	37.0	338.6	17.3	46.6	13.4	12.55	103.4
190	93.502	6.871	41.0	337.9	17.9	46.4	13.0	6.53	102.9
191	93.608	6.913	45.0	337.2	18.6	46.3	12.6	2.96	102.1
192	93.708	6.952	49.0	337.2	19.1	46.3	12.3	0.91	102.0
193	92.216	6.899	5.0	344.1	13.1	45.0	17.7	3.27	101.5
194	92.372	6.940	9.0	342.5	13.8	45.6	16.7	5.75	100.0
195	92.514	6.980	13.0	342.1	14.7	46.3	15.7	9.94	99.6
196	92.646	7.019	17.0	342.0	15.1	46.7	15.3	15.01	99.8
197	92.775	7.060	21.0	341.4	15.7	46.8	14.8	18.96	99.7
198	92.898	7.101	25.0	341.2	16.2	46.8	14.3	20.83	100.4
199	93.015	7.140	29.0	341.3	17.0	46.7	13.7	20.19	101.6
200	93.128	7.181	33.0	340.7	17.3	46.4	13.4	15.94	102.0
201	93.238	7.221	37.0	340.3	17.8	46.0	13.1	8.71	102.4
202	93.344	7.260	41.0	340.1	18.3	45.6	12.7	2.09	102.6
203	93.446	7.299	45.0	339.9	18.9	45.2	12.3	0.19	102.5
204	93.545	7.339	49.0	339.4	19.6	44.8	12.0	0.09	101.9
205	92.107	7.285	5.0	340.3	13.4	44.5	17.2	3.15	96.4
206	92.249	7.330	9.0	340.8	13.9	45.2	16.6	5.80	97.1
207	92.386	7.376	13.0	340.9	14.6	45.4	15.9	10.15	97.1
208	92.516	7.419	17.0	341.4	15.2	45.6	15.2	15.47	97.8
209	92.640	7.460	21.0	341.9	15.8	45.6	14.7	19.69	98.7
210	92.762	7.501	25.0	341.8	16.0	45.4	14.5	21.90	99.5
211	92.879	7.540	29.0	342.2	17.2	45.3	13.5	20.72	101.0
212	92.990	7.576	33.0	342.3	17.6	45.0	13.2	15.05	102.0
213	93.098	7.612	37.0	342.1	18.1	44.6	12.9	6.98	102.1
214	93.203	7.648	41.0	341.9	18.6	44.3	12.5	1.12	102.1
215	93.305	7.683	45.0	341.6	19.5	44.0	12.0	0.14	101.6
216	93.403	7.717	49.0	341.3	20.4	43.7	11.5	0.86	101.5
217	91.972	7.662	5.0	339.8	13.1	44.4	17.6	3.51	94.8
218	92.115	7.714	9.0	340.3	13.8	44.5	16.8	6.20	95.2
219	92.253	7.762	13.0	340.5	14.2	44.5	16.3	10.61	95.4
220	92.385	7.809	17.0	341.2	14.5	44.4	15.9	16.18	96.2
221	92.513	7.852	21.0	342.6	15.8	44.4	14.7	20.88	97.7
222	92.634	7.890	25.0	342.7	15.9	44.0	14.6	23.86	98.6
223	92.754	7.929	29.0	342.7	16.6	43.6	14.0	23.58	99.5
224	92.866	7.964	33.0	343.9	17.6	43.5	13.2	18.95	101.2
225	92.974	7.997	37.0	344.0	18.6	43.3	12.5	10.69	101.6
226	93.079	8.029	41.0	343.2	19.0	42.8	12.3	3.58	101.1
227	93.180	8.061	45.0	342.9	19.7	42.5	11.9	0.35	100.7
228	93.276	8.091	49.0	342.8	21.3	42.3	11.0	0.03	100.9
229	91.833	8.037	5.0	339.8	12.9	44.1	17.9	4.47	93.6
230	91.980	8.091	9.0	340.1	13.3	43.7	17.5	6.60	93.9
231	92.119	8.141	13.0	341.6	13.7	43.4	16.9	10.93	95.4
232	92.256	8.188	17.0	342.5	13.9	43.0	16.6	16.28	96.2
233	92.393	8.233	21.0	342.9	15.0	42.6	15.5	20.09	96.9
234	92.515	8.271	25.0	344.8	15.9	42.5	14.6	21.71	99.3
235	92.637	8.306	29.0	344.9	16.3	42.1	14.3	19.78	100.0
236	92.757	8.341	33.0	344.4	17.3	41.8	13.4	14.74	99.8
237	92.866	8.372	37.0	345.0	18.7	41.7	12.5	9.27	100.4
238	92.967	8.400	41.0	345.6	19.9	41.6	11.8	5.65	101.2
239	93.066	8.428	45.0	344.4	20.3	41.3	11.5	3.81	100.3
240	93.163	8.456	49.0	343.5	21.7	41.0	10.8	2.49	99.6
241	91.695	8.413	5.0	342.2	12.6	43.9	18.3	4.83	95.2
242	91.845	8.465	9.0	342.9	12.7	43.2	18.3	7.09	95.8
243	91.995	8.515	13.0	343.6	13.2	42.5	17.6	11.57	96.4
244	92.139	8.560	17.0	344.5	13.8	42.0	16.8	16.99	97.4
245	92.280	8.602	21.0	344.7	14.2	41.5	16.3	21.32	97.8
246	92.415	8.641	25.0	345.1	15.6	41.2	14.9	22.41	98.6
247	92.538	8.674	29.0	345.8	16.6	41.1	14.0	19.15	99.8
248	92.656	8.705	33.0	345.4	17.2	40.9	13.5	13.04	99.7
249	92.769	8.735	37.0	345.2	18.2	40.8	12.8	8.17	99.5
250	92.874	8.763	41.0	345.4	20.4	40.8	11.5	6.70	99.6
251	92.966	8.787	45.0	345.7	21.6	40.7	10.9	5.92	100.0

252	93.058	8.811	49.0	344.7	22.2	40.5	10.6	3.37	99.2
253	91.573	8.794	5.0	345.6	12.5	44.0	18.5	4.15	97.8
254	91.730	8.840	9.0	345.4	12.5	43.0	18.5	6.74	97.6
255	91.886	8.884	13.0	345.3	12.8	42.1	18.1	11.27	97.5
256	92.038	8.926	17.0	345.9	13.7	41.6	16.9	16.80	98.0
257	92.180	8.964	21.0	346.1	14.3	41.0	16.2	20.81	98.4
258	92.320	9.000	25.0	345.3	14.9	40.4	15.5	21.33	98.1
259	92.447	9.034	29.0	346.5	16.9	40.3	13.8	17.35	99.8
260	92.563	9.062	33.0	346.4	17.8	39.9	13.1	11.23	100.0
261	92.675	9.090	37.0	345.3	18.3	39.6	12.8	8.12	99.2
262	92.781	9.118	41.0	345.1	19.4	39.3	12.0	8.42	98.9
263	92.876	9.143	45.0	346.4	22.9	39.4	10.3	7.94	100.0
264	92.961	9.164	49.0	345.7	23.4	39.1	10.1	2.09	99.5
265	91.473	9.182	5.0	348.4	12.6	43.8	18.4	3.67	100.1
266	91.631	9.219	9.0	348.3	12.5	42.6	18.5	5.96	100.1
267	91.789	9.255	13.0	348.4	12.7	41.6	18.2	10.07	100.1
268	91.946	9.292	17.0	348.0	13.4	40.7	17.3	14.85	99.8
269	92.091	9.326	21.0	348.9	14.7	40.1	15.8	17.99	101.0
270	92.226	9.356	25.0	348.4	14.8	39.5	15.6	18.23	101.2
271	92.362	9.387	29.0	347.5	16.5	38.9	14.1	14.71	100.9
272	92.477	9.414	33.0	348.5	18.4	38.7	12.7	9.42	102.1
273	92.584	9.438	37.0	348.2	18.9	38.3	12.4	5.39	101.9
274	92.689	9.463	41.0	347.2	19.3	37.8	12.1	4.01	100.9
275	92.793	9.488	45.0	346.2	22.3	37.4	10.6	4.02	99.7
276	92.873	9.508	49.0	347.9	24.1	37.3	9.8	2.61	101.0
277	91.393	9.574	5.0	352.8	12.6	43.9	18.3	2.88	104.0
278	91.552	9.601	9.0	352.7	12.6	42.9	18.3	5.13	104.0
279	91.713	9.627	13.0	352.1	13.1	41.8	17.7	9.12	103.6
280	91.869	9.654	17.0	351.1	13.3	40.9	17.4	13.92	102.8
281	92.021	9.682	21.0	350.7	15.0	40.2	15.5	17.35	102.9
282	92.154	9.706	25.0	350.3	15.5	39.7	15.0	18.31	103.4
283	92.285	9.731	29.0	349.2	16.1	39.2	14.5	16.27	103.2
284	92.408	9.756	33.0	349.4	18.4	38.9	12.7	10.58	103.5
285	92.513	9.777	37.0	349.7	19.8	38.6	11.8	4.33	103.6
286	92.614	9.796	41.0	349.0	20.0	38.2	11.7	0.58	102.7
287	92.712	9.817	45.0	348.6	20.8	37.9	11.2	0.03	102.1
288	92.802	9.837	49.0	349.1	23.5	37.6	10.0	0.00	102.3
289	91.342	9.972	5.0	356.1	12.8	44.1	18.0	1.87	107.1
290	91.503	9.987	9.0	355.3	13.0	43.2	17.8	3.99	106.5
291	91.661	10.004	13.0	354.5	13.7	42.3	16.9	8.01	105.7
292	91.811	10.021	17.0	353.4	13.7	41.4	16.9	12.56	105.0
293	91.962	10.042	21.0	352.2	15.0	40.5	15.5	16.67	104.4
294	92.094	10.062	25.0	352.4	16.2	39.8	14.3	19.28	105.6
295	92.219	10.081	29.0	351.5	16.3	39.0	14.2	18.93	105.8
296	92.343	10.102	33.0	350.6	17.6	38.2	13.2	13.58	105.2
297	92.451	10.121	37.0	351.8	20.5	37.7	11.4	5.14	105.9
298	92.547	10.136	41.0	351.4	20.7	37.1	11.3	0.03	105.0
299	92.644	10.153	45.0	350.6	20.8	36.5	11.3	0.01	103.7
300	92.738	10.170	49.0	350.1	22.1	35.9	10.6	0.00	103.0
301	91.315	10.371	5.0	358.7	13.3	43.9	17.4	0.90	109.7
302	91.470	10.378	9.0	357.8	13.1	42.9	17.6	2.28	108.8
303	91.624	10.387	13.0	358.0	14.2	41.9	16.3	4.85	108.9
304	91.768	10.397	17.0	357.4	14.3	41.0	16.2	7.69	108.6
305	91.911	10.408	21.0	356.9	15.0	39.9	15.5	9.93	108.6
306	92.046	10.421	25.0	356.7	16.9	39.0	13.8	11.15	109.1
307	92.166	10.433	29.0	356.1	16.9	38.2	13.7	10.75	109.3
308	92.286	10.446	33.0	355.5	17.2	37.3	13.5	7.65	109.1
309	92.402	10.460	37.0	355.3	20.5	36.5	11.4	3.48	108.4
310	92.497	10.471	41.0	355.6	21.3	36.0	11.0	1.05	108.4
311	92.589	10.481	45.0	355.4	21.2	35.5	11.0	0.08	107.7
312	92.682	10.492	49.0	355.1	21.4	34.9	11.0	0.29	107.5
313	91.306	10.771	5.0	2.2	13.4	43.9	17.3	0.77	112.8
314	91.456	10.770	9.0	2.6	13.3	43.0	17.3	1.25	113.2
315	91.610	10.770	13.0	1.8	14.5	41.9	15.9	2.73	112.4
316	91.751	10.770	17.0	1.2	14.6	41.0	15.8	4.14	111.9
317	91.892	10.772	21.0	0.5	15.3	40.0	15.1	4.61	111.6
318	92.026	10.775	25.0	359.6	17.4	39.0	13.4	4.66	111.3
319	92.143	10.778	29.0	359.0	17.5	38.1	13.3	4.30	111.4

320	92.259	10.783	33.0	358.3	17.5	37.1	13.3	4.91	111.2
321	92.375	10.790	37.0	357.6	20.3	36.1	11.5	6.58	110.3
322	92.472	10.796	41.0	357.7	21.5	35.3	10.9	7.80	109.9
323	92.564	10.801	45.0	357.5	21.6	34.6	10.9	7.55	109.3
324	92.656	10.807	49.0	357.1	21.7	33.8	10.8	5.31	108.6
325	91.321	11.171	5.0	6.0	13.4	44.1	17.3	1.05	116.4
326	91.473	11.161	9.0	5.6	13.9	43.1	16.7	1.98	116.1
327	91.622	11.150	13.0	4.6	14.8	42.1	15.6	4.09	114.9
328	91.759	11.142	17.0	4.2	14.9	40.9	15.6	6.61	114.5
329	91.895	11.136	21.0	4.1	15.6	39.7	14.9	8.57	114.4
330	92.024	11.131	25.0	4.2	17.6	38.7	13.2	9.57	114.6
331	92.136	11.127	29.0	4.4	17.6	37.6	13.2	9.00	115.3
332	92.249	11.124	33.0	4.7	17.8	36.5	13.1	7.00	116.1
333	92.361	11.121	37.0	4.8	20.7	35.4	11.3	4.28	116.2
334	92.459	11.119	41.0	4.0	21.8	34.4	10.8	3.41	115.3
335	92.550	11.118	45.0	3.7	21.8	33.5	10.8	3.53	114.9
336	92.640	11.117	49.0	3.8	21.8	32.6	10.8	2.77	115.0
337	91.362	11.570	5.0	8.5	13.5	44.0	17.1	1.17	119.2
338	91.511	11.551	9.0	8.5	14.0	43.1	16.6	2.95	118.8
339	91.653	11.533	13.0	9.1	14.6	42.1	15.9	6.10	118.9
340	91.787	11.517	17.0	10.2	14.8	41.2	15.6	10.08	119.8
341	91.921	11.500	21.0	10.6	16.0	40.1	14.5	13.37	119.8
342	92.049	11.484	25.0	9.6	17.4	39.0	13.4	15.03	118.5
343	92.163	11.470	29.0	9.8	17.6	38.0	13.2	13.97	119.2
344	92.276	11.456	33.0	9.7	18.3	37.1	12.8	8.81	119.7
345	92.388	11.442	37.0	8.3	21.4	36.2	10.9	2.53	119.0
346	92.481	11.431	41.0	7.8	21.8	35.5	10.8	0.07	118.8
347	92.570	11.422	45.0	8.1	21.9	34.8	10.7	0.06	119.2
348	92.659	11.413	49.0	7.8	22.4	33.9	10.5	0.07	119.0
349	91.422	11.966	5.0	11.4	13.2	43.9	17.5	1.55	122.0
350	91.569	11.940	9.0	12.5	13.7	43.1	16.9	2.60	122.9
351	91.713	11.913	13.0	13.0	14.1	42.2	16.4	5.67	123.0
352	91.853	11.886	17.0	13.3	14.9	41.3	15.6	9.24	122.7
353	91.988	11.858	21.0	12.8	16.5	40.6	14.1	12.10	121.6
354	92.108	11.833	25.0	12.5	17.1	39.8	13.6	13.03	121.1
355	92.222	11.810	29.0	12.9	17.6	38.9	13.2	11.01	121.8
356	92.333	11.788	33.0	13.0	19.6	38.2	11.9	4.78	122.6
357	92.436	11.767	37.0	11.6	21.2	37.3	11.1	0.05	122.1
358	92.525	11.752	41.0	12.5	21.3	36.5	11.0	0.00	123.3
359	92.614	11.736	45.0	13.1	21.7	35.7	10.8	0.00	124.1
360	92.701	11.719	49.0	13.8	24.2	35.0	9.7	0.01	124.3
361	91.501	12.358	5.0	14.8	12.8	44.0	18.1	1.44	125.9
362	91.654	12.322	9.0	15.2	13.4	43.2	17.2	1.59	126.0
363	91.800	12.286	13.0	15.6	14.0	42.3	16.5	3.48	126.1
364	91.940	12.251	17.0	15.7	15.1	41.4	15.3	5.55	125.9
365	92.070	12.217	21.0	15.5	15.8	40.4	14.7	6.69	125.4
366	92.187	12.188	25.0	17.3	16.8	39.7	13.8	6.40	127.2
367	92.301	12.157	29.0	17.8	17.9	38.9	13.0	4.02	128.3
368	92.411	12.127	33.0	17.1	20.0	38.1	11.7	0.13	127.9
369	92.505	12.102	37.0	17.9	20.4	37.5	11.5	0.03	129.1
370	92.597	12.077	41.0	18.5	21.5	36.8	10.9	0.00	129.6
371	92.688	12.052	45.0	17.5	21.9	36.1	10.7	0.00	128.6
372	92.777	12.028	49.0	16.5	25.6	35.6	9.2	0.01	126.8
373	91.603	12.745	5.0	17.3	12.5	44.0	18.4	0.07	128.9
374	91.757	12.701	9.0	17.7	12.9	43.0	17.9	0.71	129.2
375	91.903	12.658	13.0	19.2	13.8	42.1	16.8	2.48	130.6
376	92.042	12.614	17.0	19.8	14.8	41.2	15.6	4.76	131.1
377	92.168	12.574	21.0	21.0	15.4	40.4	15.1	6.57	132.4
378	92.295	12.532	25.0	20.4	16.7	39.5	13.9	7.47	132.1
379	92.409	12.493	29.0	20.2	18.4	38.9	12.7	6.26	132.1
380	92.513	12.457	33.0	19.8	19.4	38.3	12.0	2.78	131.7
381	92.609	12.425	37.0	20.1	19.9	37.7	11.8	0.22	132.1
382	92.702	12.393	41.0	20.4	22.7	37.3	10.3	0.02	131.7
383	92.786	12.363	45.0	19.5	23.6	36.8	10.0	0.03	130.7
384	92.868	12.336	49.0	18.0	25.1	36.1	9.4	0.09	128.9
385	91.722	13.127	5.0	20.0	11.9	43.9	19.4	1.19	132.1
386	91.877	13.075	9.0	22.1	12.4	43.1	18.6	0.46	134.1
387	92.030	13.020	13.0	22.6	13.5	42.1	17.1	2.46	134.8

388	92.169	12.967	17.0	22.8	14.3	41.2	16.1	5.71	135.1
389	92.299	12.916	21.0	23.1	15.8	40.5	14.7	9.39	135.9
390	92.419	12.867	25.0	22.5	16.9	39.7	13.7	12.88	135.9
391	92.531	12.823	29.0	22.1	18.0	38.9	13.0	13.10	135.9
392	92.631	12.785	33.0	23.3	19.2	38.2	12.2	8.32	136.8
393	92.726	12.747	37.0	23.5	20.0	37.5	11.7	1.96	136.4
394	92.820	12.710	41.0	22.9	22.7	36.9	10.4	0.03	134.9
395	92.897	12.679	45.0	23.9	23.9	36.4	9.9	0.01	135.4
396	92.970	12.650	49.0	25.1	24.3	36.0	9.7	0.02	136.4
397	91.859	13.504	5.0	23.2	11.2	44.0	20.7	0.88	135.9
398	92.024	13.438	9.0	24.6	12.2	43.1	19.0	0.03	137.3
399	92.177	13.373	13.0	25.0	13.4	42.2	17.3	0.83	137.9
400	92.314	13.312	17.0	25.4	14.1	41.0	16.4	3.48	138.7
401	92.444	13.254	21.0	25.8	15.6	40.1	14.9	7.18	139.7
402	92.558	13.202	25.0	27.1	16.8	39.3	13.8	12.00	141.9
403	92.664	13.153	29.0	27.8	17.6	38.5	13.3	14.25	143.1
404	92.768	13.105	33.0	27.5	19.2	37.7	12.2	10.22	142.1
405	92.862	13.060	37.0	27.3	20.7	37.1	11.3	3.02	140.7
406	92.950	13.018	41.0	26.7	22.0	36.5	10.7	0.04	139.2
407	93.031	12.981	45.0	26.8	22.9	35.9	10.3	0.01	139.0
408	93.108	12.945	49.0	26.9	24.1	35.5	9.8	0.01	138.4
409	92.017	13.872	5.0	25.5	10.6	43.9	21.7	0.49	138.6
410	92.188	13.794	9.0	27.0	11.7	42.6	19.7	0.04	140.1
411	92.339	13.721	13.0	28.4	12.6	41.3	18.3	0.03	141.9
412	92.476	13.652	17.0	31.0	14.1	40.3	16.5	0.57	145.0
413	92.603	13.584	21.0	30.7	15.1	39.2	15.3	3.98	146.1
414	92.721	13.521	25.0	30.8	16.8	38.2	13.9	10.21	147.1
415	92.827	13.462	29.0	30.2	18.0	37.4	12.9	15.92	146.8
416	92.926	13.407	33.0	29.4	19.4	36.8	12.0	16.03	144.7
417	93.016	13.358	37.0	29.2	20.9	36.2	11.2	10.48	142.8
418	93.099	13.314	41.0	29.4	21.7	35.7	10.8	4.90	142.1
419	93.178	13.272	45.0	29.7	22.6	35.3	10.4	0.86	141.9
420	93.254	13.231	49.0	30.0	23.9	34.9	9.9	0.22	141.7
421	92.189	14.233	5.0	28.6	9.8	44.4	23.6	0.03	141.9
422	92.365	14.143	9.0	32.0	11.0	43.9	21.0	0.03	145.5
423	92.520	14.055	13.0	34.3	12.0	43.1	19.2	0.00	148.1
424	92.665	13.967	17.0	34.4	14.4	42.1	16.1	0.07	148.9
425	92.785	13.890	21.0	33.5	15.1	41.7	15.3	2.06	149.4
426	92.898	13.819	25.0	33.4	17.0	41.3	13.7	7.09	149.7
427	92.998	13.756	29.0	33.5	18.5	41.0	12.6	11.36	149.9
428	93.091	13.699	33.0	33.2	19.4	40.7	12.0	10.66	148.6
429	93.177	13.646	37.0	33.4	20.9	40.3	11.2	6.56	147.4
430	93.258	13.597	41.0	33.3	22.3	39.9	10.5	3.24	146.2
431	93.336	13.550	45.0	32.2	23.1	39.6	10.2	2.59	144.4
432	93.411	13.505	49.0	31.2	24.1	39.4	9.8	2.56	142.7

4.8 Summarizing Table

Mw (magnitude) and Mo (moment) are computed using shear modulus from layered earth model, Mwh and Moh assuming homogeneous rigidity of 30 GPa. Sme: mean slip, Sma: maximum slip, Ssd: standard deviation of slip, Dme: mean depth of slip, ETs: Tsunami Energy.

Table 4.7 Summarizing table.

Model	Mw	Mo e22J	Mwh	Moh e22J	chi2	rms m	Sme m	Sma m	Ssd m	Dme km	ETs e15J
IASP	9.30	11.3	9.15	6.7	1.69	0.21	8.2	23.9	6.6	-25.2	7.1
PREM	9.27	10.1	9.05	4.7	2.04	0.24	5.8	26.9	7.1	-27.9	5.8
CRUST2	9.23	8.9	9.00	3.9	2.92	0.38	4.8	31.8	7.9	-29.0	6.0
Sp260	9.29	10.9	9.13	6.3	1.68	0.20	9.5	23.9	6.9	-26.5	8.0
Sp845add	9.26	9.9	9.11	5.8	1.64	0.19	5.8	23.9	6.0	-25.5	7.2
3faults	9.29	10.9	9.15	6.7	1.67	0.26	7.9	22.2	6.1	-23.4	7.8
Dip12	9.35	13.3	9.20	8.0	1.59	0.23	9.1	24.4	6.2	-24.1	7.7
Dip15	9.28	10.5	9.09	5.5	2.01	0.20	6.2	27.8	6.5	-32.3	7.0
Dip18	9.25	9.4	9.05	4.7	3.51	0.34	5.3	31.0	7.9	-37.0	7.7

5 Investigation on afterslip and steady state and transient rheology based on postseismic deformation and geoid change caused by the Sumatra 2004 earthquake

Andreas Hoechner[1], Stephan V. Sobolev[1,2], Indridi Einarsson[1,3], Rongjiang Wang[1]
[1]German Research Centre For Geosciences, Potsdam, Germany
[2]Institute of Physics of the Earth, Moscow, Russia
[3]Technical University of Denmark, Copenhagen, Denmark

An edited version of this paper was published in: Geochemistry Geophysics Geosystems, 12, Q07010, doi: 10.1029/2010GC003450. Received 30 November 2010; revised 11 May 2011; accepted 11 May 2011; published 14 July 2011. Edited by T. Becker.

5.1 Abstract

The commonly used rheological model for the Earth's mantle when considering geological time scales (mantle convection) is the viscoelastic Maxwell model, which assumes a steady state creep process. However, application of this model to phenomena on shorter time scales, such as postglacial rebound or postseismic relaxation, leads to difficulties in finding a consistent interpretation of obtained viscosities. Using standard Maxwell viscosity of 1e19 Pa•s to analyze postseismic near field GPS time series from the 2004 Sumatra-Andaman Earthquake requires large time dependent afterslip with a relaxation time of about one year. We show that using linear biviscous Burgers rheology for the asthenosphere, together with a refined coseismic slip model, we can drastically reduce the amount of apparent afterslip. Comparison of predicted geoid change to observations by the GRACE satellite mission shows that a univiscous Maxwell model with afterslip is not compatible with observations, since even large afterslip has a more localized effect than transient relaxation due to the main earthquake, which in turn is in agreement with observations. Thus, a combination of ground- and space based geodetic observations is very useful in differentiating between rheological models. An additional independent discrimination between afterslip and biviscous relaxation could be obtained by installing ocean bottom pressure gauges close to the trench.

5.2 Introduction

The relation between deformation and forces in the Earth is described by rheology, which therefore comprises a fundament of geodynamics. Recent studies employ a number of methods to constrain rock rheology [Bürgmann and Dresen, 2008] including monitoring of deformation using high precision GPS measurements. GPS observations provide a wealth of information and physical insight on very different time scales: they are used to monitor the relative motions of the tectonic plates, to measure intraplate deformations or buildup of strain at plate boundaries and thus inferring locking conditions [Chlieh et al., 2008]. Abrupt coseismic displacements can readily be extracted from time series and be used to construct earthquake slip models which are better in capturing static moment and determining deformation at the sea floor than seismic inversions [Menke et al., 2006], making them useful for tsunami early warning

[Sobolev et al., 2006; Sobolev et al., 2007; Babeyko et al., 2010]. A more exotic application of GPS for tsunami early warning is given by [Stosius et al., 2010, 2011], where it is proposed to observe GPS reflections at the sea surface from space in order to enable global monitoring of sea surface height anomalies. On very short time scales, GPS has been used to reconstruct rupture propagation [Vigny et al., 2005] and can be used as a low frequency seismometer not suffering from clipping, tilting or hysteresis effects. However, interpretation of postseismic GPS time series in terms of rheology often remains ambiguous [Bürgmann and Dresen, 2008], partially because such poorly constrained processes as afterslip and poroelastic rebound are involved.

As was shown by Paul et al. [2007], the temporal characteristics of postseismic GPS data from the Andaman Islands cannot be interpreted by means of viscoelastic relaxation if assuming Maxwell rheology. Using a typical viscosity of 1e19 Pa·s for the upper mantle leads to modeled displacements being much too small. Using a viscosity of 2e18 Pa·s brings the amplitudes of the model 1.5 years after the earthquake to the right value, but the modeled relaxation time is much too large, and the model clearly overshoots the data. Thus, Paul et al. [2007] concluded that the largest contribution to the observations stems from exponentially time dependent afterslip at the subduction interface down dip of the coseismic slip.

Another interpretation was given by Pollitz et al. [2006; 2008], who analyzed postseismic GPS data from far-field stations in Singapore and Thailand and proposed to apply biviscous Burgers rheology, which can be represented by a Maxwell- and a Kelvin element in series (section 5.11). In that model, the Maxwell element is responsible for the long-term behavior, whereas the Kelvin element dominates on shorter time scales. In fact, most of the signal observed up to now can be attributed to this transient process. Note that Burgers rheology is considered to be the simplest rheology which incorporates a transient creep regime, whose contribution to relatively low-strain (typically less than 10^{-5}) and short-term deformation processes, like postglacial rebound (thousands of years) has often been suggested [Karato, 2008]. Even more it has to be considered for postseismic analysis, as it is associated with similarly low strains on even shorter time scales.

GRACE (Gravity Recovery And Climate Experiment) is a twin satellite mission launched in March 2002, whose goal is to map variations in the Earth's gravity field with a spatial resolution of about 400 km and a temporal resolution of one month [Tapley et al., 2004]. Several studies have used GRACE data to analyze the effect of the Sumatra earthquake on the geoid. The strong coseismic depression in the Andaman Sea was demonstrated e.g. by Han et al. [2006], Han and Simons [2008] and de Viron et al. [2008], the postseismic recovery was shown e.g. by Ogawa and Heki [2007], Panet et al. [2007], Chen et al. [2007], Han et al. [2008] and Cannelli et al. [2008] compared postseismic observations to modeling results assuming univiscous Maxwell rheology. Recently, Panet et al. [2010] combined the analysis of GRACE observations with far field GPS data in order to infer viscosity parameters for biviscous Burgers rheology of the upper mantle and to quantify the amount of afterslip.

In this study we consider GRACE data together with near field GPS time series to constrain viscosity of the asthenosphere for both standard Maxwell and biviscous Burgers rheology, enabling us to discriminate between the two. Concerning Burgers rheology, we also analyze a rheological parameter which has not been addressed in previous studies: the ratio γ between the Kelvin- and the Maxwell shear moduli. We show that afterslip has only a second order effect on the postseismic geoid evolution as compared to viscous relaxation stemming from the fast transient response of a biviscous asthenosphere.

5.3 Data and Modeling

We use postseismic GPS time series from the Andaman Islands by Paul et al. [2007], the locations are shown in Figure 5.4. Only those sites are used, which have at least three sets of measurements with some time in between. After subtraction of the interseismic velocity of v_{is}=(3.59/3.02/0.0) cm/y (east/north/up) as estimated by Paul et al. [2007], we fit exponential relaxation curves with common relaxation time to all time series obtaining a relaxation time τ_0 of about 13 months. A similar value is obtained if using longer time series available from Paul's web page (http://www.ceri.memphis.edu/people/jpuchkyl/) as PDF document, but not yet in digital form. In section 5.3 we compute rmsd of our rheological models to the observations, and we use the relaxation time as an additional constraint to quantify the match between model and observation. Fitting of exponential decays is a phenomenological approach, actually the situation is more complex for geometrical and rheological reasons, but for the relatively short period of time of interest here, the fit well captures the transient behavior. Figure 5.3 (circles) shows the time series. The interpolated postseismic displacement after 18 months is used for the optimization of the coseismic slip model in section 5.5 and alternatively for the inversion of the afterslip model in section 5.6.

We use a coseismic slip model of the M_w=9.3 Sumatra-Andaman earthquake of 2004 by Hoechner et al. [2008] as starting point. Modeling of the postseismic response is performed for a layered viscoelastic half space using code PSGRN/PSCMP by Wang et al. [2006] testing several hundred rheological models. Maxwell rheology can be represented by a spring in series with a dashpot, where exponential relaxation is the response to a strain step. Burgers rheology comprises an additional Kelvin-Voigt element (spring in parallel with a dashpot) in series with the Maxwell element (see 5.11). Here, the strain step response basically consists of two superposed exponential decays. The Burgers body is the simplest rheological model accounting for elastic, transient and steady state deformation [Ranalli, 1995, p. 222]. As was shown by Pollitz et al. [2006], Burgers rheology is better suited than Maxwell rheology for explaining postseismic time series of GPS stations several hundred kilometers away from the rupture. We perform a similar analysis for near field data and additionally investigate the ratio between the shear moduli in the Burgers model.

5.4 Selection of the rheological Earth model: Thickness of the elastic layer and viscosities

We follow Pollitz et al. [2008] assuming a purely elastic lithosphere, underlain with Burgers rheology in the asthenosphere (pure Maxwell asthenosphere alternatively) to 210 km depth and Maxwell rheology in the mantle below. We vary the thickness of the elastic layer d_e. In the asthenosphere, we vary the transient viscosity η_1 (Kelvin-Voigt), the steady state viscosity η_2 (Maxwell), as well as the ratio between the shear moduli $\gamma=\mu_1/\mu_2$. Viscosity is 1e20 Pa·s below 210 km and 1e21 Pa·s deeper than 660 km according to Pollitz et al., [2006]. Shear modulus is from the IASP velocity model

[Kennett and Engdahl, 1991]. Details are listed in section 5.11. The viscosities control timing of the processes, while the thickness of the elastic layer d_e determines the spatial pattern of deformation

To quantify the compliance of the various rheological models with GPS data, we first compute root mean square deviation of modeled and observed displacement time series (Figure 5.1, upper left panel). The preference for d_e= 40 km is evident, as well as η_2=1e19 Pa·s (solid lines). The parameters η_1 and γ are not as easy to choose, having all similar rmsd. In order to get an additional constraint for model selection, we fit exponentials to the models and compare the relaxation times to the phenomenological value of τ_0=13 months obtained for the observations in the previous section. $\Delta\tau$ is the absolute value of the difference between model relaxation time and observed relaxation time (Figure 5.1, right side). We now see, that of the models with η_2=1e19 Pa·s, the best ones have η_1=1e18 Pa·s. The choice of γ is still not clear. We select d_e=40 km, γ=0.43 (α=0.30), η_1=1e18 Pa·s, η_2=1e19 Pa·s (magenta, solid line, stars) as our preferred model, because it has smallest rmsd of all models, (3rd smallest $\Delta\tau$) and yields best accordance with geoid data, as we show in section 5.7.

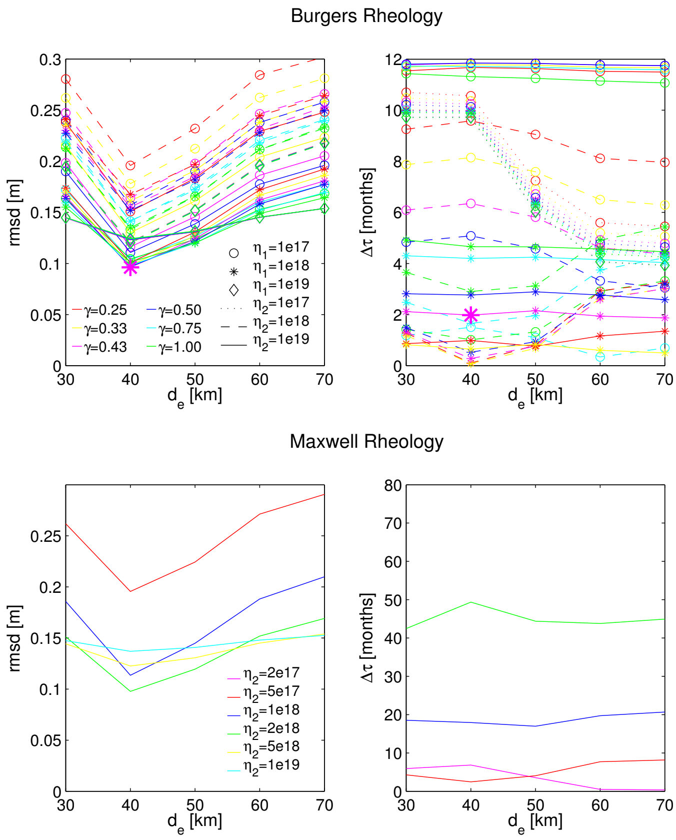

Figure 5.1 Left side: Root mean square deviation between modeled and observed GPS time series for various rheological parameters. Right side: Difference $\Delta\tau$ of the phenomenological relaxation time in model and observation. Top: Burgers rheology. Preference for an elastic thickness of 40 km as well as steady state viscosity η_2 of 1e19 Pa·s (solid lines) is evident. The large magenta star indicates the preferred model, selected as explained in the text. Bottom: Maxwell rheology. Here, rmsd and $\Delta\tau$ mutually contradict each other.

However, models with γ between 0.25 and 0.5 and viscosity combinations within a factor of 2 or so (not computed in this study) would probably also be an acceptable choice and cannot be discarded on the basis of these data. Observed and modeled vertical displacement for the best sampled station (CARI) is shown in Figure 5.2. Time series for all stations and components are shown in Figure 5.3 (dashed lines). It is interesting to note that the obtained thickness of the elastic layer d_e corresponds well to the maximum depth of significant slip of about 45 km in the coseismic slip model, and to a locking depth of 40-50 km inferred from analysis of interseismic GPS data [Chlieh et al., 2008].

We perform the same analysis for pure Maxwell rheology in the asthenosphere, so viscosity η_2 is the only free parameter. Smallest rmsd is obtained for η_2=2e18 Pa·s and is comparable to that using Burgers rheology. But the relaxation time is much too large (75 months). A viscosity value of η_2=5e17 Pa·s results in a correct relaxation time but very large rmsd due to too large amplitude. Both models have to be rejected, as illustrated in Figure 5.2 exemplarily for the vertical component at CARI. A standard asthenosphere viscosity of η_2=1e19 Pa·s leads to a relaxation time of more than 1000 months and much too small amplitudes. We thus confirm the conclusion by Paul et al. [2007], that it is not possible to reproduce the observed behavior using Maxwell rheology without large afterslip. However, Burgers rheology can overcome the mentioned problems. We look at the remaining discrepancies between observation and model, especially at station RMNG, in the next section and further improve conformance.

Figure 5.2 (lower left panel) also shows that saturation of the Kelvin-Voigt relaxation process should clearly become visible in time series of about 8 years length. After 10 years, uplift rate is about 5 mm/y for the Burgers model and 13 mm/y for standard Maxwell asthenosphere (η_2=1e19 Pa·s). After more than 100 years the behavior of the two rheological models becomes similar. After 200 years the subsidence rate is still more than 2 mm per year, which may play some role when estimating locking conditions at the plate interface.

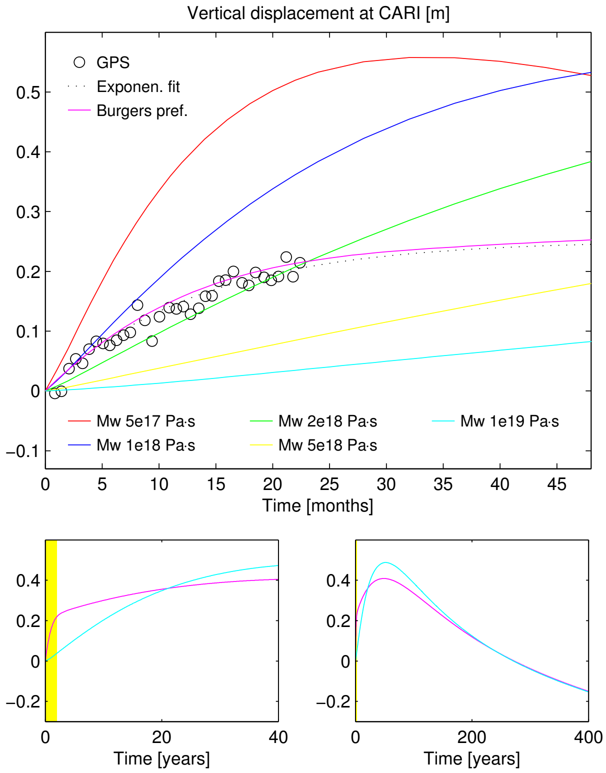

Figure 5.2 Upper panel: Postseismic vertical displacement at station CARI. Circles: observations (down sampled for better visibility). Dotted black line: exponential fit to data. Magenta: Preferred Burgers rheology model with η_1=1e18 Pa·s, η_2=1e19 Pa·s, γ=0.43. Other colors: Maxwell models. The Maxwell models are incompatible with observations due to inadequate timing and/or asymptotic amplitude. Lower panels: Long term prediction. The yellow area denotes the range covered by the data used in this study and which corresponds approximately to the transient response period of the Burgers rheology.

In section 5.10 we compare model GPS time series to observations in Thailand, showing that transient rheology performs better than univiscous rheology (even if including afterslip) also in the far field.

5.5 Coseismic slip model fitting co- and postseismic displacements

As can be seen in Figure 5.3, the observations are qualitatively reproduced by the model using Burgers rheology (dashed lines), with exception of the horizontal components at station RMNG. Inspection of Figure 5.4 (upper middle and right panel) reveals that the Andaman Islands are located close to a postseismic displacement tilt line: horizontal component changes from ‘north-east’ to ‘south-west’, vertical component from ‘down’ to ‘up’ around RMNG. Hence it can be expected that the modeled time series can be significantly altered by a slight change in coseismic slip distribution. Thus, we perform a joint inversion for slip based on co- as well as postseismic data (time point 18 months after the earthquake) after removing the contribution stemming from relaxation processes according to our preferred Burgers model from the postseismic GPS data, This solution does not deteriorate the quality of the fit to coseismic displacements, and at the same time is in agreement with the postseismic response.

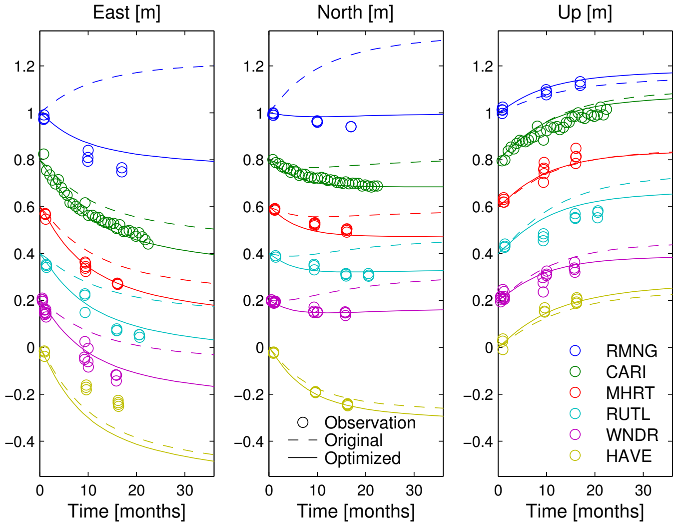

Figure 5.3 Time series of postseismic displacement interpreted using Burgers rheology. Circles: observations (CARI has been down sampled), dashed line: original slip model, solid line: optimized coseismic slip model taking into account displacement after 18 month.

The resulting slip distribution as well as the postseismic deformation of the original and the optimized slip model are shown in Figure 5.3. The solid lines in Figure 5.3 depict the time series corresponding to the optimized slip distribution. The total moment of the coseismic model is not affected, but the slight shifting of the zero-displacement isoline changes direction of the modeled postseismic response at station RMNG, bringing it to agreement with the observations and improving conformance of the time series at the other stations, except for a small deterioration at the east component of station HAVE.

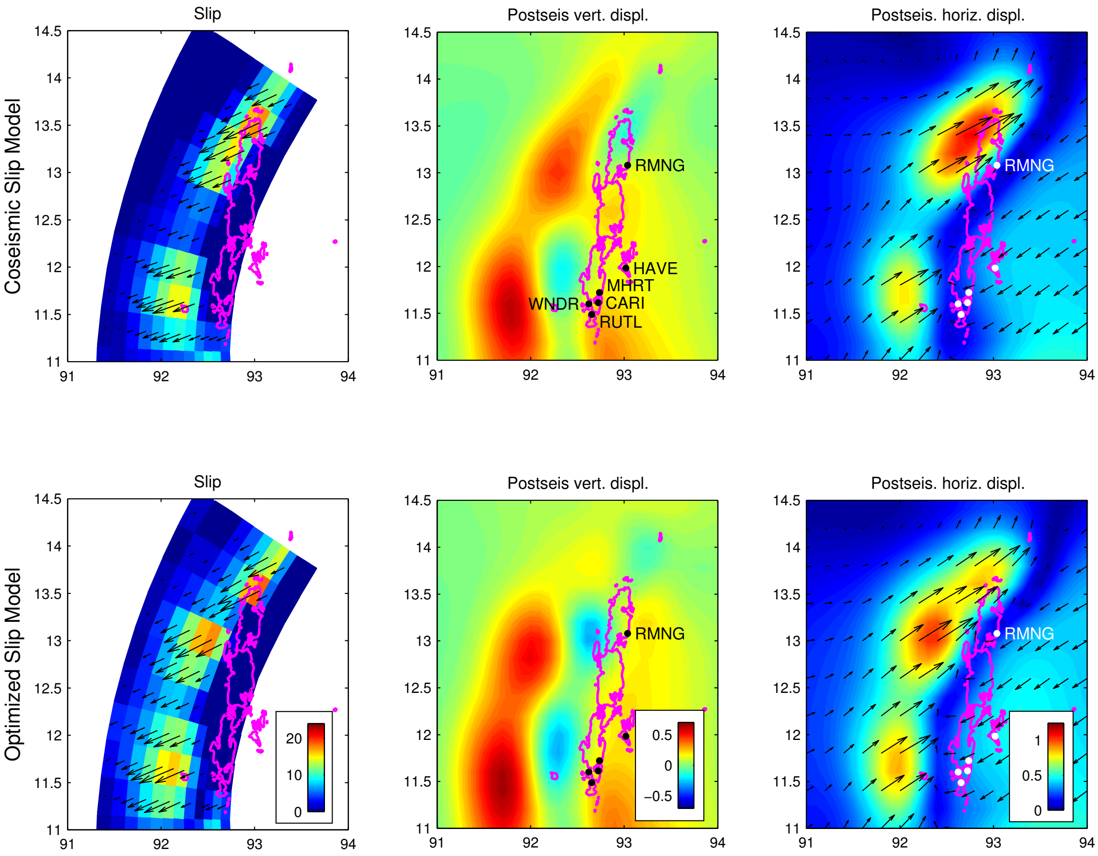

Figure 5.4 Top: original, bottom: optimized coseismic slip model. Labels indicate the positions of the GPS stations. The slight change in slip distribution has noticeable effect on the postseismic displacement pattern, e.g. direction of horizontal displacement is reversed at RMNG. Total moment and fit to coseismic GPS data are not significantly affected.

5.6 Maxwell rheology and afterslip model

In the previous section, we showed that Burgers rheology in the asthenosphere, together with an improved coseismic slip model, can explain the postseismic displacements of the GPS stations very well. An alternative explanation is time-dependent postseismic slip (afterslip), mostly down-dip of the coseismic slip [Banerjee et al., 2007; Paul et al., 2007]. We investigate this explanation using Maxwell rheology also for the asthenosphere with a typical viscosity of η_2=1e19 Pa·s and thus being responsible only for the long term behavior, and invert for afterslip to obtain the postseismic signal after 18 months. Following Paul et al. [2007], we consider postseismic slip with an exponential decay shape function and apply a relaxation time of 13 months corresponding to the analysis of the GPS data in section 5.3.

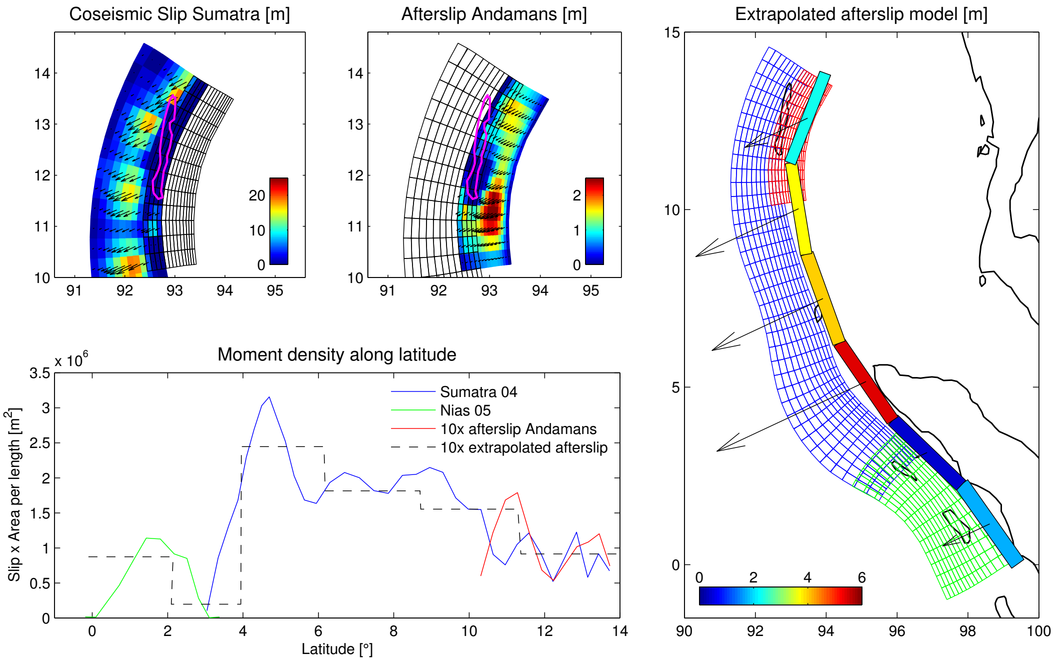

Figure 5.5 Upper left: Coseismic slip model of the Sumatra 2004 earthquake. Upper middle: Postseismic slip model inverted from postseismic GPS data from the Andaman Islands. Bottom left: Moment as a function of latitude, used to extrapolate afterslip to the whole area of the Sumatra 2004 and Nias 2005 earthquakes. Right: Blue mesh: Extension of the Sumatra earthquake model, Green: Nias, Red: postseismic slip model at the Andaman Islands. Filled rectangles: extrapolated afterslip model used for the computation of the geoid change in section 5.7.

The amount of thus estimated afterslip for the Andaman Islands is about 10% of coseismic slip, as is shown in Figure 5.5 (lower left panel). Conformance of the time series, shown in Figure 5.6, has roughly the same quality as that from the Burgers model from the section before (Figure 5.3). Thus, based on this GPS data alone, a discrimination of the main contributor to postseismic displacement is not possible.

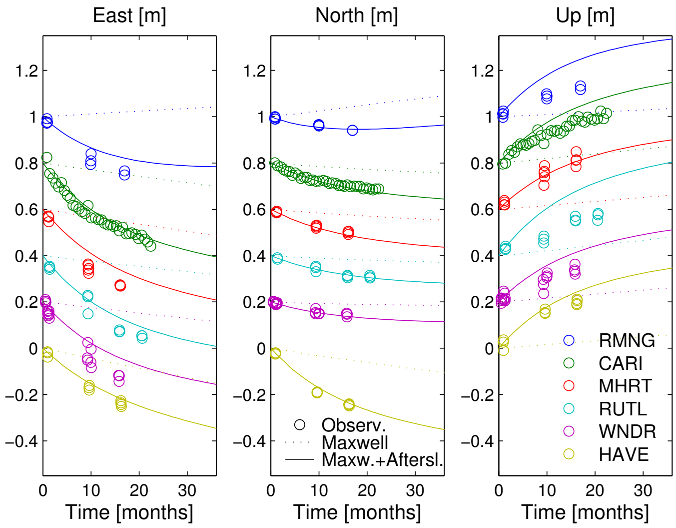

Figure 5.6 Time series of postseismic displacement interpreted using Maxwell rheology. Circles: observations, dotted line: Maxwell rheology in the asthenosphere with a viscosity of 1e19 Pa·s, solid line: Maxwell rheology plus exponentially time dependent afterslip.

5.7 Comparison to geoid change by GRACE

Since both the Burgers- as well as the Maxwell model with afterslip are in agreement with postseismic GPS displacements, we need an additional independent observation to distinguish between the two explanations. Therefore we calculate postseismic geoid change for the two and compare to observations by the GRACE satellites. We use the GFZ-RL04 monthly GRACE Stokes coefficients [Schmidt et al., 2008] convolved with an anisotropic filter and smoothing parameter a=10^{11} [Kusche, 2007]. The filtered coefficients are mapped to residual geoid heights on a grid with 0.25° resolution around the area of interest. For details concerning processing of GRACE data we refer to [Einarsson et al., 2010], where also possible contributions from other sources like hydrology variations are considered. Computation of the model geoid is done with PSGRN/PSCMP [Wang et al., 2006] and an additional tool (POTCON by R. Wang), to extrapolate the geopotential changes from the solid Earth surface (i.e. the ocean bottom) to the geoid and then filter them with a Gaussian of 250 km smoothing radius.

In order to be able to compute geoid change due to afterslip, we need an afterslip model for the region of the Sumatra 2004 and Nias 2005 earthquakes. Published afterslip models e.g. by Banerjee et al., [2007] and Chlieh et al., [2007] are constrained by 1 month of postseismic GPS data. Since we need 18 months of afterslip to fit our near-field data, we extrapolate our model to the required region as follows. Based on Figure 5.5 (lower left panel), we assume that slip times area of the afterslip model is 10% of that for the earthquake. We place six subfaults at the depth of relevant inverted postseismic slip, which is between 57 and 77 km depth. Dip angle is between 20° and 30°. It is not necessary to use more subfaults, since spatial smoothing is applied anyway to the geoid in order to compare it to GRACE. The afterslip model is listed in section 5.12. Comparison of this model to the ones mentioned above shows that the slip pattern is actually quite similar, but our total moment is about twice as high, so that it can be considered an end member model. Afterslip is activated exponentially decaying with relaxation time of 13 months corresponding to the analysis of the GPS data in section 5.3.

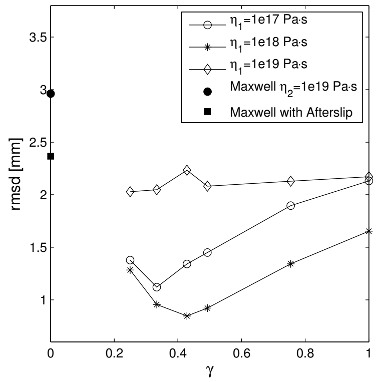

Figure 5.7 Fit of modeled postseismic geoid change time series (4 years) to GRACE observations. Shown are models with varying η_1 and γ, which are poorly constrained by GPS data alone (see Figure 5.1).

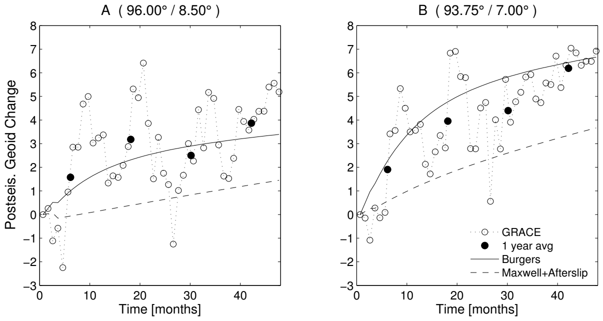

Figure 5.8 Time series of geoid change for points A and B. The small step after three months is caused by the Nias earthquake.

Figure 5.7 shows fit between models and observations for the parameters η_1 and γ which are not well constrained by the analysis of GPS data in Figure 5.1. rmsd is computed using 9 points in space around the central region of the postseismic signal (92°, 94°, 96° of longitude, 5°, 7°, 9° of latitude) and yearly averages of postseismic geoid change for the first four years. Preference for η_1=1e18 Pa·s and γ=0.43 results clearly. On the left axis are the Maxwell models with and without afterslip, both having significantly larger rmsd than the Burgers models. Figure 5.8 shows geoid time series for points A and B indicated in Figure 5.9, where geoid difference between the first and fourth year is displayed. We thus confirm the finding of Han et al. [2008] and Panet et al., [2010], that a biviscous (Burgers) rheology is more adequate for modeling the postseismic geoid response to the Sumatra earthquake.

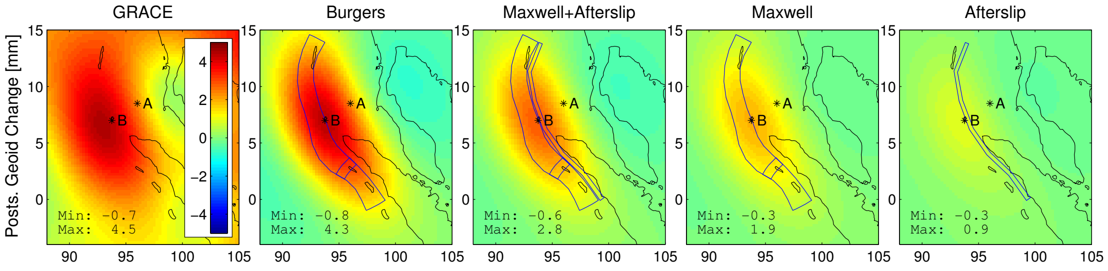

Figure 5.9 Postseismic geoid change, shown as average of fourth year minus first year after the Sumatra earthquake. Burgers rheology is in accordance with GRACE, Maxwell rheology plus afterslip model under predicts the observed effect.

The reason why there is a significantly larger impact on the geoid resulting from Burgers relaxation than from Maxwell relaxation plus afterslip, even though their vertical deformation pattern at the Andaman Islands is very similar, is that most of the postseismic deformation in the Burgers case is actually happening in the ocean west of the Andaman Islands (Figure 5.10) and is much smaller (slower) in the Maxwell case and not affected at all by afterslip. Unfortunately it cannot be monitored by GPS there, but we suggest that it could be observed with appropriately located sea floor pressure gauges.

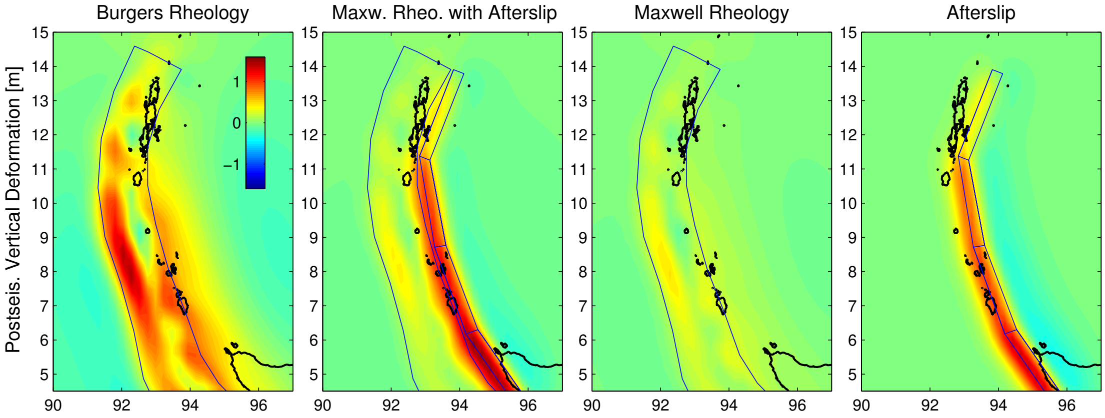

Figure 5.10 Postseismic uplift after 4 years as caused by the different models.

5.8 Summary and Conclusions

We use postseismic surface deformation caused by the Sumatra-Andaman earthquake of 2004 recorded by GPS stations at the Andaman Islands and geoid change observed by the GRACE satellites together with our previous model of coseismic slip to constrain the rheology of the crust and mantle in the region.

We show that a model implementing Burgers transient rheology in the asthenosphere, together with a slightly refined coseismic slip model, is able to reproduce postseismic GPS time series very well. The inferred thickness of the purely elastic upper layer is 40 km, which coincides with the maximum depth of relevant slip in the coseismic model. Below, the Maxwellian viscosity contributing to the long-term behavior has a typical value of 1e19 Pa·s, whereas the Kelvin-Voigt viscosity originating the transient response is ten times smaller. Variation of the ratio γ of the shear moduli in Burgers rheology, which has been assumed to be equal to 1 in previous studies, results in an optimum of γ=0.43. However, this result is not unique, in a sense that models with γ between 0.25 and 0.5 and viscosity combinations within a factor of two or so, which were not computed in this study, would probably also be good solutions.

As an alternative, we construct an afterslip model for the Sumatra and Nias earthquakes using a typical Maxwell rheology for the asthenosphere. This model also very well explains the GPS observations, and suggests large afterslip yielding about 10% of the coseismic moment.

Although both the Burgers and the Maxwell plus afterslip models explain near field GPS data equally well, they do significantly differ in their prediction of far-field deformation on the offshore side of the trench and thus also in geoid change. The Burgers model predicts large postseismic geoid change that is consistent with the observations from the GRACE satellites. In contrary, the Maxwell model with afterslip predicts much smaller postseismic geoid change. In order to be in accordance with geoid data for Maxwell rheology with afterslip, we would require afterslip amounting to a moment of about 35 % of the co-seismically released moment, which appears to be quite unrealistic and is not compatible with GPS time series.

The Burgers model is the simplest model showing elastic, transient- and steady-state viscous behavior. Being linear, it allows semi-analytical computation of a large number of rheological earth layer models. Going one step further, one could employ a generalized Burgers or Maxwell model which exhibits a continuous spectrum of relaxation times. Such models have successfully been used to interpret postglacial rebound [Müller, 1986], but not yet for postseismic deformation. Another approach to tackle complex postseismic behavior is to apply non-linear rheology such as power-law dependence of viscosity on stress using finite element modeling. These models result in a time and space-dependent effective viscosity and have been used to study postseismic deformation for strike-slip earthquakes [Freed and Burgmann, 2004; Freed et al., 2006]. However, as Freed et al. [2010] showed recently, steady-state power-law flow laws alone cannot fully explain GPS observations following the 1999 Hector Mine earthquake, which implies some sort of transient weakening phase in response to the earthquake. Nevertheless, it would be desirable to apply power-law viscosity modeling to very large subduction earthquakes, and especially comparing predictions of geoid change to those by biviscous linear models.

We conclude that satellite observations of geoid change after large earthquakes appear to be very useful to discriminate between rheological models. In the case of the Sumatra-Andaman earthquake of 2004, geoid data clearly favor a transient type of rheology in the upper mantle. An independent discrimination between afterslip and relaxation contributions to postseismic deformation could be provided by analyzing data from ocean bottom pressure gauges located about 50 km landwards from the trench after a large subduction earthquake, like the recent Tohoku earthquake on March 11, 2011.

5.9 Acknowledgments

This is publication no. 101 of the GITEWS project (German Indonesian Tsunami Early Warning System). The project is carried out through a large group of scientists and engineers from GFZ (German Research Centre for Geosciences) and its partners from DLR, AWI GKSS, KDM, IFM-GEOMAR, UNU, BGR, GTZ, as well as from Indonesian and other international partners. Funding is provided by the German Federal Ministry for Education and Research (BMBF), Grant 03TSU01.

5.10 Appendix A: Comparison to far field GPS

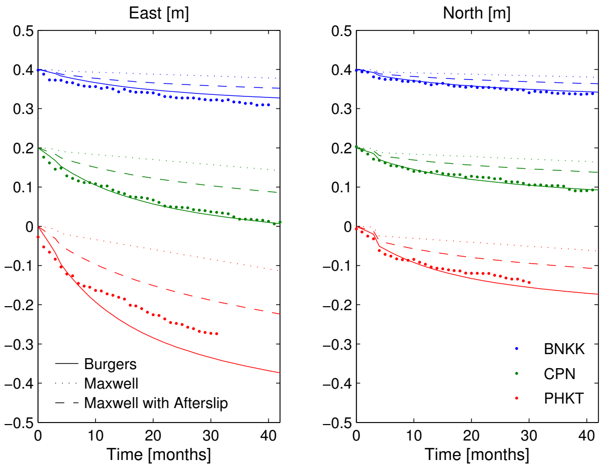

Figure 5.11 East and north displacements at Bangkok, Chumphon and Phuket (Thailand). GPS observations are from Panet et al. [2010] (down sampled). Model time series are computed for Burgers and Maxwell rheology and include the effect of the Sumatra 2004 and Nias 2005 earthquakes. The afterslip model is listed in section 5.12.

The afterslip model with Maxwell rheology, which is in accordance with near field observations from the Andaman Islands, yields too small amplitudes for the observations in Thailand. Burgers rheology (without afterslip) results in good agreement, only the east component at PHKT is slightly overestimated (Figure 5.11).

5.11 Appendix B: Rheological Earth model

The co- and postseismic surface deformation and geoid changes induced by the earthquake models are computed using code PSGRN/PSCMP [Wang et al., 2006] implementing Burgers rheology (a Kelvin-Voigt body and a Maxwell body in series connection, see Figure 5.12) for relaxation of shear modulus. No relaxation of compressional modulus is considered. An additional tool (POTCON) by R. Wang is used to extrapolate the theoretical co- and post-seismic geopotential changes from the solid Earth surface (i.e. the ocean bottom) to the geoid and then filter them with a Gaussian of 250 km. Table 5.1 contains the parameterization of the viscoelastic, gravitational half-space. Elastic parameters correspond to IASP [Kennett and Engdahl, 1991], viscous parameters are derived as described in section 5.4. In our preferred model, the elastic layer has a thickness of 40 km, the transient (Burgers) zone goes to 210 km depth (asthenosphere), below is Maxwell rheology.

η_1= Transient viscosity (dashpot of the Kelvin-Voigt body; $\eta_1 \leq 0$ means infinite) [Pa·s]
η_2 = Steady-state viscosity (dashpot of the Maxwell body; $\eta_2 \leq 0$ means infinite) [Pa·s]
α = Ratio between the effective and the unrelaxed shear modulus
= $((\mu_1 \cdot \mu_2)/(\mu_1+\mu_2))/\mu_2=\mu_1/(\mu_1+\mu_2)$, $0<\alpha<=1$, $\alpha=1$ corresponds to Maxwell rheology
$\gamma = \mu 1/\mu 2=\alpha /(1- \alpha)$ (used in Figure 5.1)
$\mu_1=\alpha /(1- \alpha)\cdot\mu_2$
$\mu_2=v_s^2\rho$

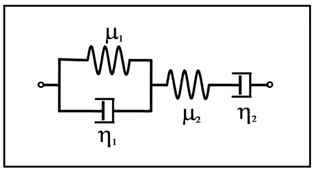

Figure 5.12 Spring-dashpot representation of a Burgers body.

The following table describes the preferred earth layer model from section 5.4. For Maxwell rheology as used in section 5.6, η_1=0 and α=1 everywhere.

Table 5.1 Earth layer model.

#	depth	v_p	v_s	ρ	η_1	η_2	α	γ	μ_1	μ_2	τ_1	τ_2
1	0	5.80	3.36	2720	0	0	1	Inf	Inf	3.1e10	0	0
2	20	5.80	3.36	2720	0	0	1	Inf	Inf	3.1e10	0	0
3	20	6.50	3.75	2920	0	0	1	Inf	Inf	4.1e10	0	0
4	35	6.50	3.75	2920	0	0	1	Inf	Inf	4.1e10	0	0
5	35	8.04	4.47	3320	0	0	1	Inf	Inf	6.6e10	0	0
6	40	8.04	4.47	3323	0	0	1	Inf	Inf	6.6e10	0	0
7	40	8.04	4.47	3323	1e18	1e19	0.33	0.43	2.2e10	6.6e10	1.4	4.8
8	120	8.05	4.50	3371	1e18	1e19	0.33	0.43	2.3e10	6.8e10	1.4	4.6
9	120	8.05	4.50	3371	1e18	1e19	0.33	0.43	2.3e10	6.8e10	1.4	4.6
10	210	8.30	4.52	3426	1e18	1e19	0.33	0.43	2.3e10	7.0e10	1.4	4.5
11	210	8.30	4.52	3426	0	1e20	1	Inf	Inf	7.0e10	0	45.3
12	410	9.03	4.87	3547	0	1e20	1	Inf	Inf	8.4e10	0	37.7
13	410	9.36	5.07	3756	0	1e20	1	Inf	Inf	9.7e10	0	32.8
14	660	10.20	5.60	4065	0	1e20	1	Inf	Inf	1.3e11	0	24.9
15	660	10.79	5.95	4371	0	1e21	1	Inf	Inf	1.5e11	0	204.9
16	760	11.06	6.21	4431	0	1e21	1	Inf	Inf	1.7e11	0	185.6
17	760	11.06	6.21	4431	0	1e21	1	Inf	Inf	1.7e11	0	185.6
18	1000	11.46	6.38	4570	0	1e21	1	Inf	Inf	1.9e11	0	170.3
19	1000	11.46	6.38	4570	0	1e21	1	Inf	Inf	1.9e11	0	170.3
20	1200	11.77	6.51	4684	0	1e21	1	Inf	Inf	2.0e11	0	159.7
21	1200	11.77	6.51	4684	0	1e21	1	Inf	Inf	2.0e11	0	159.7
22	1400	12.05	6.63	4795	0	1e21	1	Inf	Inf	2.1e11	0	150.6
23	1400	12.05	6.63	4795	0	1e21	1	Inf	Inf	2.1e11	0	150.6

5.12 Appendix C: Afterslip model used for geoid computation

Slip listed below is activated as $s(t)=sli\cdot(1-\exp(-t/\tau))$ with a relaxation rate τ of 13.3 months, according to GPS observations. The cumulated moment after 18 months is about 10 % of the Sumatra earthquake, the asymptotic value is 14 %.

```
Moment: 1.24e+022 Nm (mu=4e10 Pa)
Magnitude: 8.7
Max slip:  7.3 m
Avg slip:  3.9 m
```

Table 5.2 Extrapolated afterslip model.

Nr	lon	lat	dep	str	dip	len	wid	sli	rak
1	99.233	-0.100	57.0	324.6	22.8	304.7	51.6	2.29	80.4
2	97.672	2.097	57.0	313.7	25.1	295.2	47.1	0.56	70.6
3	95.721	3.957	57.0	325.6	26.1	294.2	45.5	7.26	81.5
4	94.190	6.177	57.0	340.3	26.2	296.0	45.3	5.41	94.7
5	93.270	8.712	57.0	350.8	28.6	289.0	41.8	5.01	103.9
6	92.829	11.372	57.0	21.0	29.7	299.8	40.4	3.05	131.9

6 Deriving Earthquake Rupture Timing from GPS Observations

Andreas Hoechner,[1] Stephan V. Sobolev[1,2]
[1]GeoForschungsZentrum Potsdam, Germany
[2]Institute of Physics of the Earth, Moscow, Russia

6.1 Abstract

We investigate the suitability of a quasi-static deformation propagation assumption for a large earthquake in order to derive rupture timing properties from coseismic GPS time series. To this purpose we convolve linear ramp source time functions with the final static value of deformation at the receiver assuming a propagation velocity corresponding to P-wave travel times. In order to calibrate the inversion procedure, we generate synthetic scenarios with different epicenter and rupture speed. We then apply the inversion to coseismic GPS time series from the Sumatra 2004 earthquake to derive onset times at the subfaults.

6.2 Introduction

The Sumatra earthquake and tsunami of 2004 are certainly among the most intensively studied events ever, and the first above magnitude 9 recorded with modern digital seismometers, GPS and various satellite instruments. Shortly after the event several publications used these data applying novel techniques to derive as much information on the source mechanism as possible. Krüger and Ohrnberger [2005a; 2005b] and Ishii et al. [2005] used teleseismic arrays to track the propagation of the rupture, Stein and Okal [2005] and Park et al. [2005] used Earth's normal modes to get a better estimate of the magnitude, which was severely under estimated in the first place. Unlike seismic methods, which are based on the analysis of seismic waves and are a measure of the seismic energy being radiated, GPS measures the static (low frequency) displacement caused by an earthquake, which is also the cause of the tsunami and thus provides information which is in many respects complementary to traditional source mechanism reconstructions. The power of GPS for near to real-time earthquake magnitude estimation and tsunami early warning was demonstrated by Blewitt et al. [2006; 2009], Sobolev et al. [2006; 2007] and Babeyko et al. [2010]. A more exotic application of GPS for tsunami early warning is given in Stosius et al. [2010], where it is proposed to observe reflections of GPS signals at the sea surface from space in order to enable global monitoring. Long term GPS time series capturing the post seismic evolution of displacement and analysis of GRACE satellite gravity observations have been used to infer rheological properties of the upper mantle [Pollitz, 2003; Pollitz, Bürgmann, et al., 2006; Pollitz et al., 2008; Einarsson et al., 2010; Hoechner et al., 2011] or locking conditions at the plate interface [Konca et al., 2008; Chlieh et al., 2008]. Vigny et al. [2005] used coseismic GPS time series from the [SEAMERGES] and [IGS] networks to qualitatively estimate the propagation of the rupture, see also the animated figure on the web page (http://www.geologie.ens.fr/~vigny/BAceh_dynamic_5.gif). In the present study we use the same GPS time series as used by Vigny et al. [2005] and try to get a more quantitative view of the rupture process. The approach is based on a wave form inversion without actually using seismic waves, but making the assumption of a quasi-static evolution and propagation of displacement.

6.3 Approach

Since static displacement caused by slip at the fault decays much faster with distance than seismic waves, especially surface waves, and since the resolving power of GPS in space and time is orders of magnitudes lower than that of seismometers, GPS receivers have to be located quite close to the source in order to produce useful data. On the other hand, the amount of permanent displacement at the surface caused by very large earthquakes can reach more than 10 meters and yet is very hard to measure with velocity or acceleration seismometers because of clipping, tilting, noise, and hysteresis effects. Unfortunately, the permanent GPS stations available at the time of the Sumatra 2004 earthquake were not located in the near field, and we have to check the assumption we make here, namely that static displacement dominates the seismograms. To this purpose we compute the ratio between peak dynamic and final static horizontal displacement for the 2004 event using code QSGRN/QSCMP by Wang et al. (to be published), see left panel of Figure 6.1. It is close to unity around the rupture area and increases steeply after some distance. The right panels show synthetic seismograms (solid lines) and the time series for our quasi-static approach (dashed) for the three locations labeled in the left panel. In case of the near field station KARD, the conformance is very good, for PHKT it is acceptable but there is a significant time lag, and for SIS2, where the static displacement is only a few cm, we clearly miss the dynamic features of the seismogram.

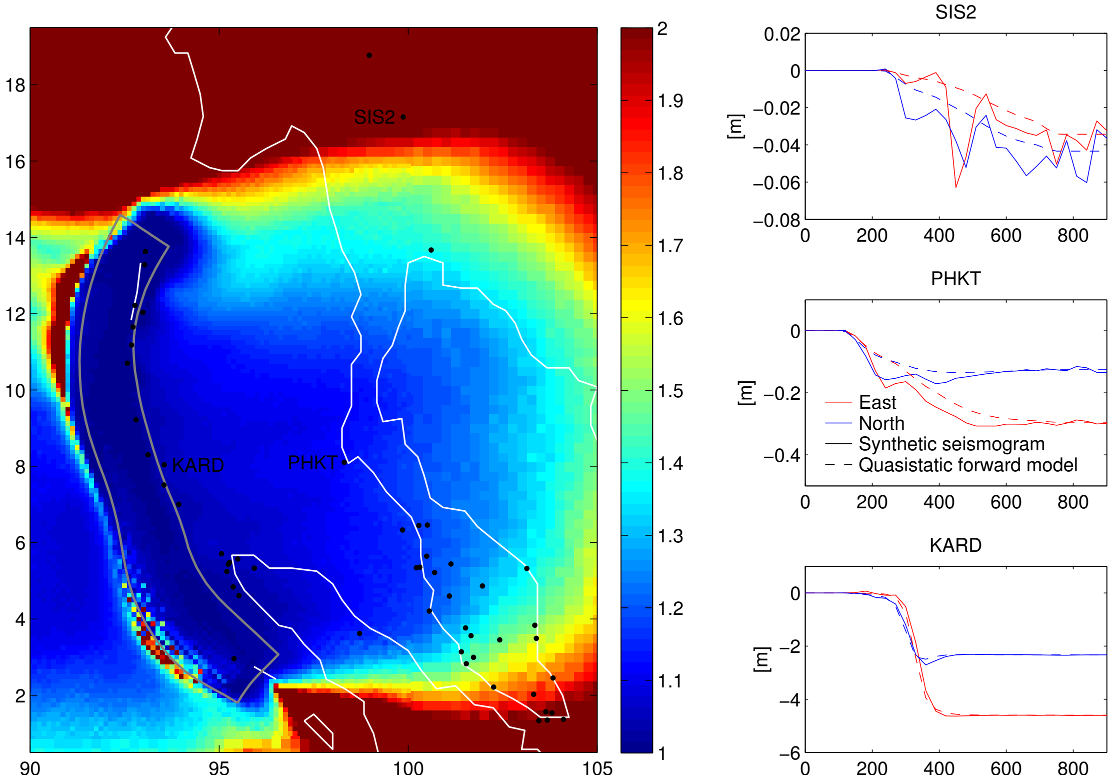

Figure 6.1 Left panel: Ratio between peak dynamic and final static horizontal displacement. Right panels: Synthetic seismograms and quasi-static time series at different distances from the rupture area.

As mentioned above, GPS is very well suited in reconstructing slip distribution at the fault [Subarya et al., 2006; Chlieh et al., 2007], given the receivers are located close enough to the source. Since this is not the case here, we will use the slip distribution by Hoechner et al. [2008], which is based on GPS data as published by Banerjee et al.

[2007], and only try to derive the rupture propagation characteristics from the 30 seconds sampling rate GPS time series from the far field. The goal is to obtain onset times for slip at every subfault. In the first place we tried to also estimate rise times, but realized that this was not possible with the far field data available, so rise time was set to 30 seconds, assuming a linear ramp until full slip is achieved. We further reduce the number of degrees of freedom by projecting the slip distribution from Hoechner et al. [2008] with 12x36 subfaults to a simpler fault model using 3x10 subfaults as shown in Figure 6.2. The propagation velocity of static displacement lies between P- and S-wave velocity [Lee et al., 2003, p. 945], we use the travel time tables for P-waves by Kennett et al. [1995] based on the Earth layer model AK135. The final static displacement at the receiver caused by slip at the fault is computed using code PSGRN/PSCMP by Wang et al. [2006], which implements a semi-analytical approach for a layered half space.

The displacement at station *l* in direction *m* (east/north) caused by slip at the faults is:

$$d_l^m(t) = \sum_{n=1}^{2} \sum_{k=1}^{N_F} f(t - t_k^O - t_{kl}^T) \cdot s_k^n \cdot G_{kl}^{mn} ,$$

where *k* is the subfault index, *n* the slip component (dip/strike), N_F the number of subfaults, t^O is onset time, t^T is P-wave travel time, *s* is the slip component and *G* are the Green's functions for static displacement.

The inversion minimizes misfit root mean square between observed and modeled time series. In order to stabilize the inversion we add a spatial smoothing constraint for the onset times with weighting term α. The cost function is:

$C = rms^2 + \alpha \cdot roughness(t^O)^2$, with

$$rms = \sqrt{\frac{1}{2N_S N_T} \sum_{l=1}^{Ns} \sum_{m=1}^{2} \sum_{t=t_0}^{t_{end}} \left(D_l^m(t) - d_l^m(t)\right)^2} .$$

N_S is the number of stations, N_T the number of time steps. The roughness of the distribution of the onset times is defined as:

$$roughness = \sqrt{\frac{1}{N_D v} \sum_{NN=1}^{N_D} diff_{NN}{}^2} ,$$

summing over all the differences between nearest neighbors, v=4·variance(T^O). It is equal to zero if all onset times are identical, equal to one for a checkerboard and ~0.7 for a random distribution.

6.4 Data

We use the far field GPS time series by Vigny et al. [2005], but only from stations which are within 1000 km from the rupture area in order not to overstress the quasi-static approach. Since there is too much noise and some correlated oscillations on the vertical component, only horizontal components are used, see blue arrows in the right panel of Figure 6.2. For the synthetic tests in the next section we also use some near field stations (red arrows). These are from Banerjee et al. [2007] with the restriction that horizontal displacement is at least one meter.

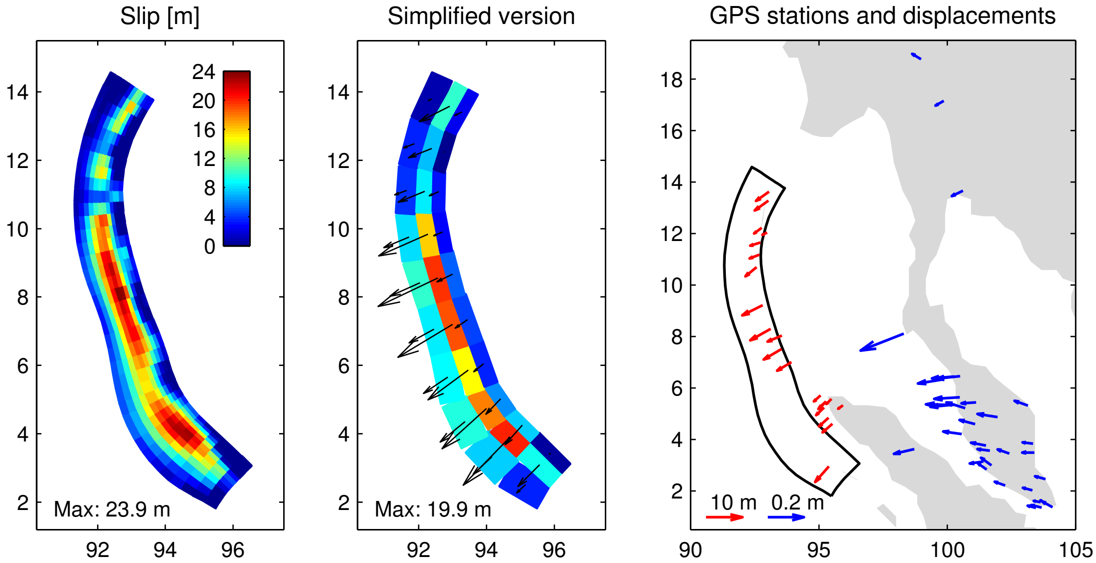

Figure 6.2 Left panel: Coseismic slip distribution of the Sumatra earthquake from Hoechner et al. [2008] with 12x36 subfaults. Central panel: Slip distribution projected on a simpler fault model with 3x10 subfaults. Right panel: Blue: GPS data from Vigny et al. [2005] no more than 1000 km from the fault, Red: GPS data from Banerjee et al. [2007] with at least 1 m of horizontal displacement.

6.5 Synthetics and Validation

In order to check the feasibility of our approach and to calibrate the weight of the smoothing constraint α we first generate two forward models using the station constellations described in the previous section. The first scenario is quite similar to the Sumatra event, having its epicenter at 95° longitude and 3° latitude and a rupture speed of 2 km/s. The second scenario has its epicenter at 93° longitude and 13° latitude and a rupture velocity of 4 km/s propagating to the south. Figure 6.3 shows the forward models in the first column. The second column shows the results of the inversion using near field stations and the third column using far field stations. As can bee seen, the reconstruction is very good for the near field, but using the far field stations, the estimated rupture velocity of the southern epicenter scenario is about two times too high. The reason therefore can be understood by looking at the middle right panel of Figure 6.1: the inversion procedure minimizes the time lag between the synthetic seismogram and the quasistatic approach of this particular scenario by lowering the onset times, a symptom we will have to keep in mind when looking at real observations in the next section.

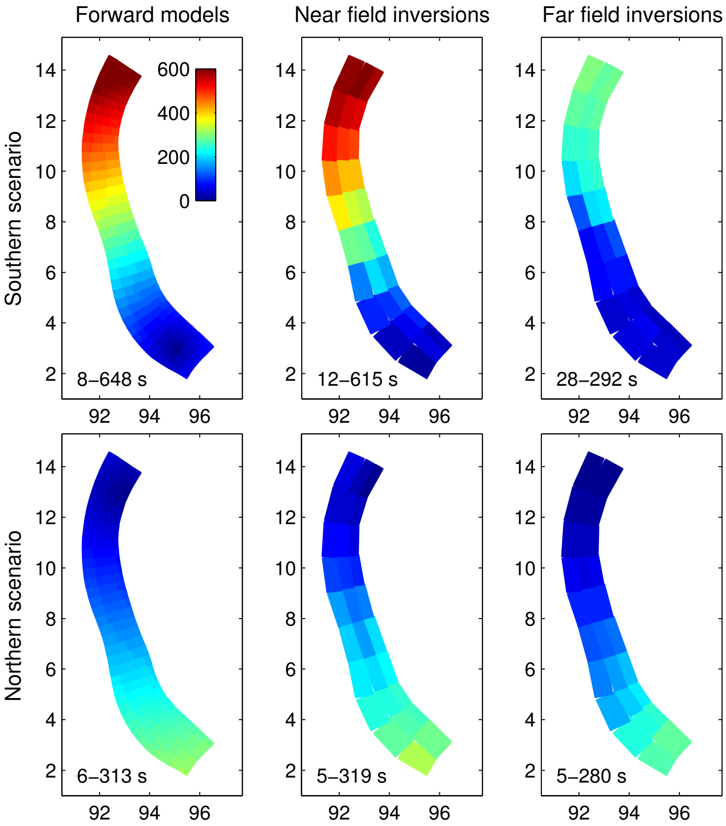

Figure 6.3 Rupture onset times at the subfaults. Top: Southern epicenter scenario, bottom: northern epicenter scenario. First column: forward models (synthetic seismograms). Second column: quasi-static inversions using near field stations. Third column: same using far field stations.

6.6 Results

The left panel on Figure 6.4 shows the obtained onset times when using the GPS time series by Vigny et al. [2005] with duration of 660 seconds. The epicenter is correctly located at the southern edge of the fault zone, the rupture propagating to the north. But the obtained rupture velocity is much too high when compared to teleseismic estimates which indicate rupture duration of about 10 minutes. This is due to the poor station coverage (large distances) and could be expected from the synthetic tests in the previous section. An additional difficulty arises from the poor signal to noise ratio which GPS stations have at this distance from the earthquake. The right two panels show for two selected stations the actual GPS time series (solid lines) and the inverted quasi-static model (dashed). The figures for all stations can be found in Appendix A.

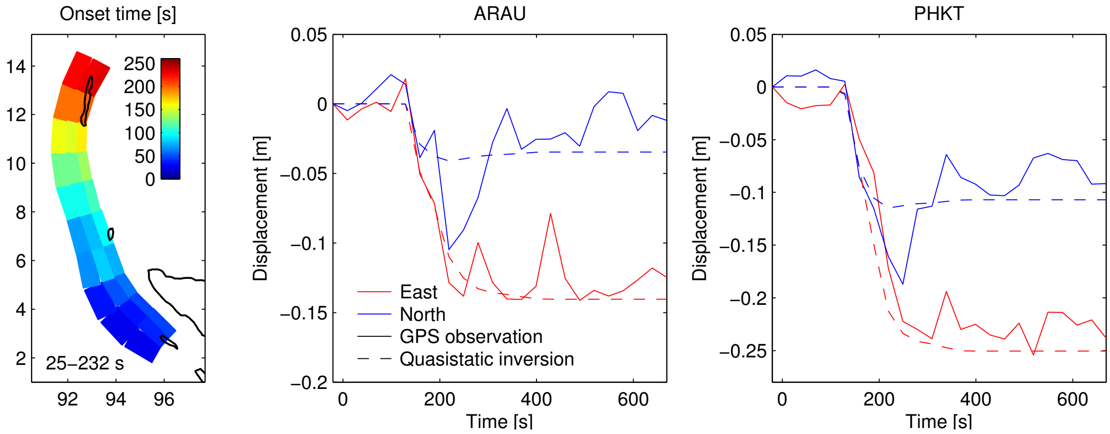

Figure 6.4 Left panel: Inverted rupture onset times based on the GPS time series by Vigny et al. [2005] of the Sumatra 2004 earthquake. Right: Time series at two selected stations

6.7 Conclusions

Using coseismic GPS time series we were able to derive the location of the epicenter and the direction of the rupture process. However, we failed to correctly determine the rupture velocity, obtaining a value about two times too high. This is due to the fact that our approach of quasi-static displacement propagation breaks down if the stations are too far away from the rupture, where static displacements become small compared to dynamic oscillations and the signal to noise ratio of GPS stations is poor. However, the synthetic tests demonstrate that given good real-time station coverage, which will be achieved quite soon e.g. for Sumatra, it is possible to invert not only for slip using GPS, but also to investigate rupture timing. Therefore we think that the approach applied here could be a valuable supplement to existing seismic methods which is simple, robust and efficient.

6.8 Acknowledgments

This is publication no. 156 of the GITEWS project (German Indonesian Tsunami Early Warning System). The project is carried out through a large group of scientists and engineers from GFZ (German Research Centre for Geosciences) and its partners from DLR, AWI GKSS, KDM, IFM-GEOMAR, UNU, BGR, GTZ, as well as from Indonesian and other international partners. Funding is provided by the German Federal Ministry for Education and Research (BMBF), Grant 03TSU01.

6.9 Appendix A

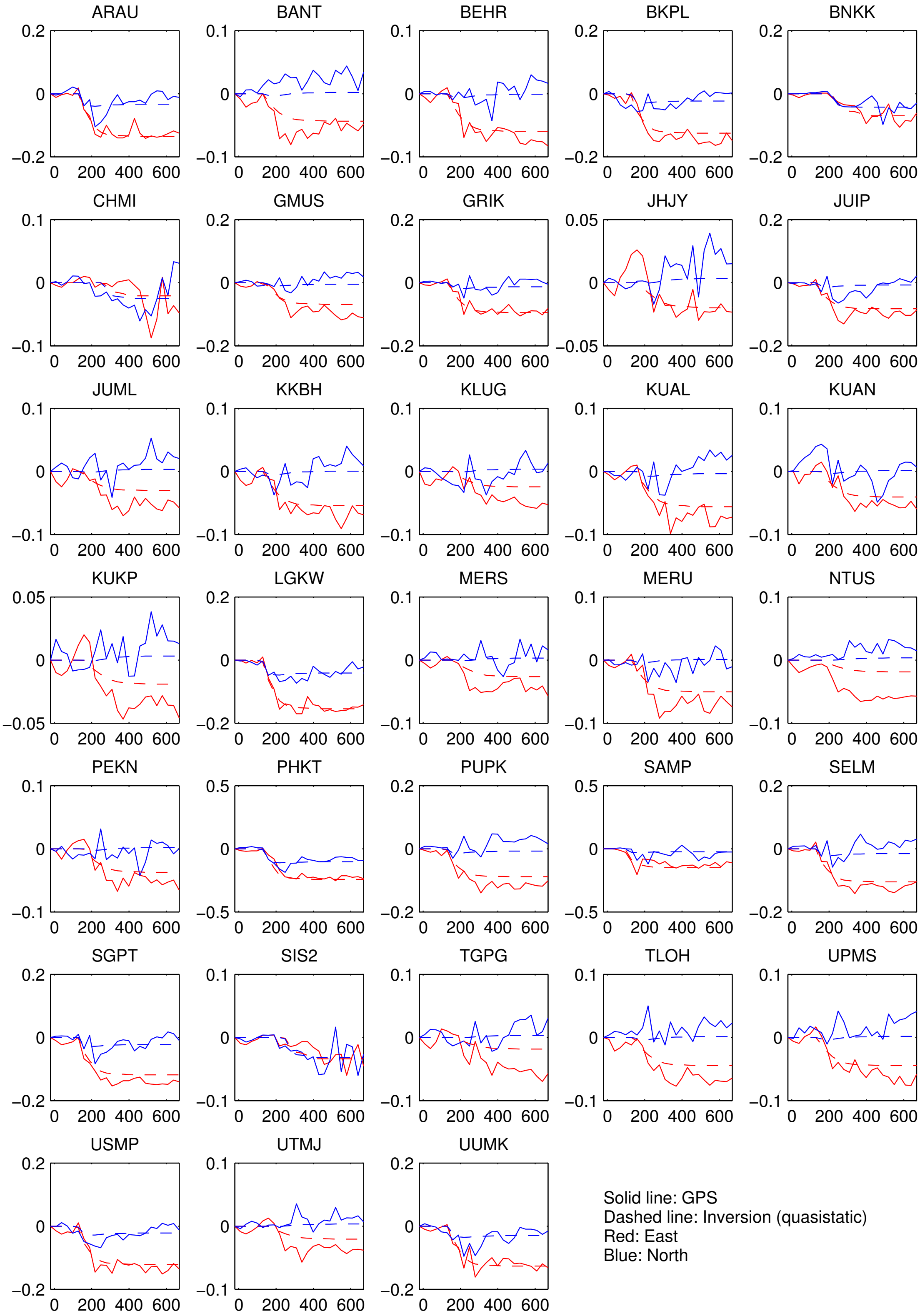

Figure 6.5 Horizontal GPS time series (solid lines) and inverted quasi-static model (dashed line) for all stations.

7 Tsunami early warning using GPS-Shield arrays

Stephan V. Sobolev[1,2], Andrey Y. Babeyko[1], Rongjiang Wang[1], Andreas Hoechner[1], Roman Galas[1], Markus Rothacher[1], Dmitry V. Sein[3], Jens Schröter[3], Joern Lauterjung[1], Cecep Subarya[4]

[1]GeoForschungsZentrum Potsdam, Germany
[2]Institute of Physics of the Earth, Moscow, Russia
[3]Alfred Wegener Institute, Bremerhaven, Germany
[4]BAKOSURTANAL, Jakarta, Indonesia

An edited version of this paper was published in: Journal of Geophysical Research, 112, B08415, doi: 10.1029/2006JB004640. Received 20 July 2006; revised 4 May 2007; accepted 24 April 2007; published 25 August 2007. Reviewed by J. Freymueller, R. Bürgmann, and H. Latief. . Copyright (2007) American Geophysical Union.

7.1 Abstract

The 2004 catastrophic Indian Ocean tsunami has strongly emphasized the need for reliable tsunami early warning systems. Another giant tsunamigenic earthquake may occur west of Sumatra, close to the large city of Padang. We demonstrate that the presence of islands between the trench and the Sumatran coast makes earthquake-induced tsunamis especially sensitive to slip distribution on the rupture plane as wave heights at Padang may differ by more than a factor of 5 for earthquakes having the same seismic moment (magnitude) and rupture zone geometry but different slip distribution. Hence reliable prediction of tsunami wave heights for Padang cannot be provided using traditional, earthquake-magnitude-based methods. We show, however, that such a prediction can be issued within 10 minutes of an earthquake by incorporating special types of near-field GPS arrays ('GPS-Shield'). These arrays measure both vertical and horizontal displacements and can resolve higher order features of the slip distribution on the fault than the seismic moment if placed above the rupture zone or are less than 100 km away of the rupture zone. Stations in the arrays are located as close as possible to the trench and are aligned perpendicular to the trench, i.e., parallel to the expected gradient of surface coseismic displacement. In the case of Sumatra and Java, the GPS-Shield arrays should be placed at Mentawai Islands, located between the trench and Sumatra and directly at the Sumatra and Java western coasts. We demonstrate that the 'GPS-Shield' can also be applied to northern Chile, where giant earthquakes may also occur in the near future. Moreover, this concept may be applied globally to many other tsunamigenic active margins where the land is located above or close to seismogenic zones.

7.2 Introduction

The international community was shocked by the catastrophic consequences of the great Andaman-Nicobar Islands earthquake occurring 26 December 2004 in which more than 250,000 casualties resulted, mostly due to the impact of the induced tsunami waves. This event triggered a number of international and national initiatives aimed at establishing modern and robust tsunami early warning systems. The specific mission of the German Indian Ocean Tsunami Early Warning System (GITEWS), led by the National Center of Geosciences (GeoForschungsZentrum) in Potsdam, Germany, is to provide early warning of tsunamis for the Indian Ocean coast of Indonesia, which is located only 200-300 km from the subduction zone trench. The proximity of the coast to the potential tsunamigenic source means that a tsunami is expected to arrive only 20-30 minutes after an earthquake. This makes early warning particularly difficult. Moreover, as we will show below, near-field tsunamis are also very sensitive to the slip heterogeneity on the fault [Geist and Dmowska, 1999; Geist, 1998]. As a consequence, even a very fast derivation of standard earthquake parameters like magnitude and hypocenter, which are usually sufficient to predict far-field tsunamis [Okal, 1988], will not solve the problem of local tsunami warning. The key task within GITEWS is therefore to quantify rupture parameters with a degree of detail that exceeds the standard set of parameters within 10 minutes of the event.

In this paper, we suggest a technique for the fast and reliable determination of the earthquake rupture parameters controlling tsunami generation at a subduction zone. First, we discuss the possible location and likely parameters of the next giant earthquake in the Indonesian region. Next, we calculate two possible earthquake and tsunami scenarios for the region of the city of Padang (Sumatra Island). We demonstrate that two earthquakes with the same magnitude, location, and fault geometry but different distribution of slip may generate tsunami waves with drastically different impacts on the coast of Padang. We then suggest an observation system based on a real-time GPS array that is able to distinguish between the two different tsunami scenarios. We analyze the potential of this observation system for resolving rupture parameters and discuss related real-time GPS accuracy issues. Finally, we demonstrate that the suggested system, hereafter called 'GPS-Shield', may also be applied to the Chilean coast, or even globally in all tsunamigenic regions at active margins where the land is located above or close to the seismogenic zone.

7.3 Scenarios of Another Giant Earthquake in Indonesia

7.3.1 Where Will Another Giant Earthquake Occur?

The 2004 Sumatra earthquake was followed by another large earthquake in March 2005 with the rupture zone directly continuing the 2004 rupture zone to the south and which approximately repeated the 1861 rupture [Briggs et al., 2006] (Figure 7.1 a). Interestingly, this second earthquake was predicted by the analyses of the regional Coulomb stress changes caused by the 2004 earthquake [McCloskey et al., 2005]. Another large earthquake in the region is expected south of the 2005 earthquake rupture zone [Nalbant et al., 2005; Pollitz, Banerjee, et al., 2006], and it may well be similar to the Mw = 8-9 earthquakes that occurred in this region in 1797 and 1833 [Sieh et al., 2004] (Figure 7.1a). The tsunami generated by this future earthquake may be very dangerous for the Indonesian city of Padang, which has a population of more than 750,000 and is located close to the expected rupture zone. Below we analyze in detail possible consequences of this particular expected earthquake for the Sumatra coast and for Padang. Interestingly, Mignan et al. [2006] suggested that the subduction fault at that location is not yet close to failure, and that it may be still required a few tens of years for preparation of the earthquake there.

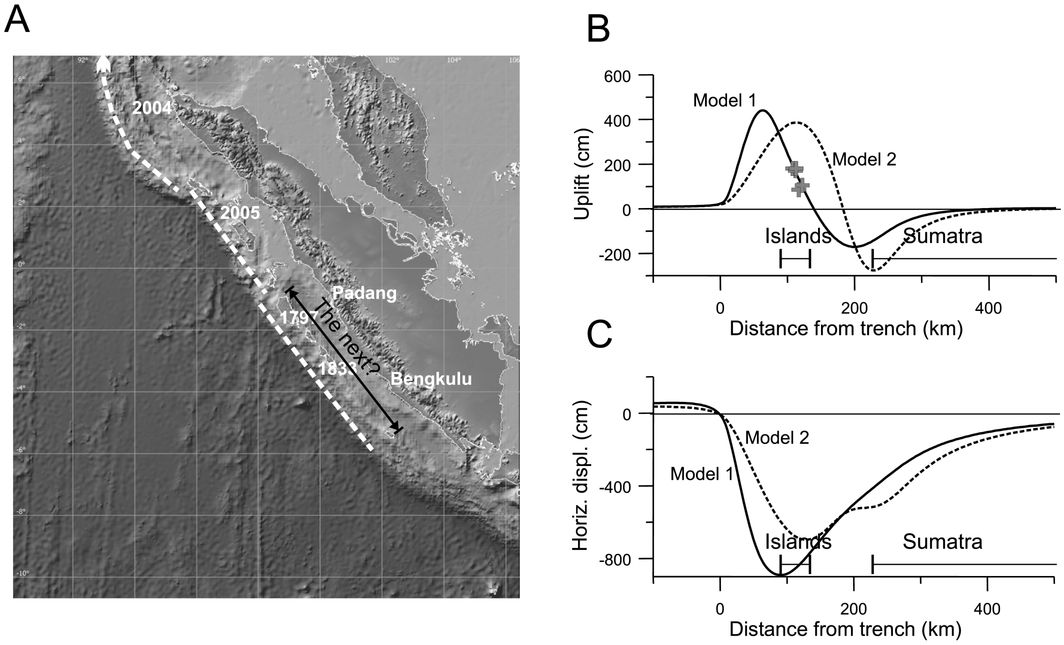

Figure 7.1 (A) Location of the rupture zones of the largest earthquakes near Sumatra. The next giant earthquake is expected where the magnitude 8-9 earthquakes occurred in the years 1797 and 1833 [K. Sieh et al., 2004]. (B) Expected static vertical displacement at the surface caused by the expected future earthquake. The rupture parameters of the earthquake (rupture model 1, solid curve) have been chosen to fit data on island uplift resulting from the 1833 event, which are based on observations of coral reefs (crosses, [Zachariasen et al., 1999]). The dashed curve indicates another possible rupture model (rupture model 2) having the same seismic moment and fault geometry as model 1, but a deeper slip maximum at the fault. (C) Horizontal (trench perpendicular) displacements caused by the possible future earthquakes. Note that the expected displacements and their trench-perpendicular gradients are very large at the islands located between the trench and Sumatra.

The possible coseismic vertical displacements at the islands during the 1833 earthquake were estimated based on data from coral reefs [Zachariasen et al., 1999]. We use these displacements to constrain fault and slip parameters of a future earthquake. To characterize the rupture, we employ the distributed-slip parameterization [Freund and Barnett, 1976; Geist and Dmowska, 1999]. The advantage of this particular parameterization is that remaining very simple, it applies physically justified conditions at the fault ends, which keep finite stress at the crack tips and allows asymmetrical slip distribution at the fault. Details of that parameterization are given in Appendix A, where we also demonstrate that such parameterization accurately describes slip distribution in natural rupture.

Using this parameterization, we invert displacement data [Zachariasen et al., 1999] for the rupture parameters using the Nelder and Mead downhill simplex method [Press et al., 1992]. The resulting range of possible solutions is very large. We use the solution that has an average downdip slip at the fault of 8.5 m, which can be expected if it is assumed that the seismogenic zone has been locked since the 1833 event. The parameters of this solution (hereafter called rupture model 1) are presented in Table 7.1.

Table 7.1 For description of used parameterization [Freund and Barnett, 1976; Geist and Dmowska, 1999] and meaning of parameters see Appendix A.

Model name	φ [°]	z1 [km]	W [km]	U_{mean} [m]	q []
Rupture model 1	12	1.3	250	8.5	0.34
Rupture model 2	12	1.3	250	8.5	0.7
Rupture Chile	20	10	150	10	0.5

Very recently, while this paper was in review, Borrero et al. [2006] have calculated possible tsunami scenarios for 1797 and 1833 events at Sumatra and analyzed most probable scenarios for the future giant earthquakes and tsunamis in this region. Their preferred models are close to our rupture model 1.

The slip distribution at the fault during a future earthquake will not necessarily be the same as for the 1833 event. Therefore we also analyze the consequence of another possible, although perhaps less probable rupture model hereafter called model 2. Rupture model 2 (see Table 7.1) has a slip maximum at a greater depth than model 1, with all other parameters being the same. Note that while models 1 and 2 have the same seismic moment (in a homogeneous elastic half-space) and fault dimensions, they generate rather different vertical (Figure 7.1b) and horizontal (Figure 7.1c) displacements. Below we demonstrate the dramatic consequences of this difference for the induced tsunamis. However, a common feature of both rupture models is that at a distance of 90-130 km from the trench, where the islands are located, they both generate very large vertical and horizontal displacements and displacement gradients (Figure 7.1b and Figure 7.1c). This feature is crucial to our study.

7.3.2 Tsunami Induced by the Expected Sumatra Earthquake

Using the vertical displacements from Figure 7.1b as the initial wave heights along the trench in the region of the expected future earthquake (Figure 7.1a), we calculate the propagation of the tsunami waves for rupture models 1 and 2. To do so, we numerically solve nonlinear shallow-water equations in spherical coordinates using an explicit-in-time finite element integration scheme [Hanert et al., 2005] on an unstructured grid and wetting-drying boundary condition at the coast. The unstructured grid allows for increasing resolution close to the coastal regions, where the maximum accuracy of solution is required [Tinti and Gavagni, 1995]. The node spacing varies from 150 m near the Sumatra coast to 15 km in the deep ocean. In our model, we employ 1 arc minute bathymetry data (GEBCO: www.ngdc.noaa.gov/mgg/gebco/) supplemented by recently obtained detailed data for the Sumatra region (E. Flüh, personal communication).

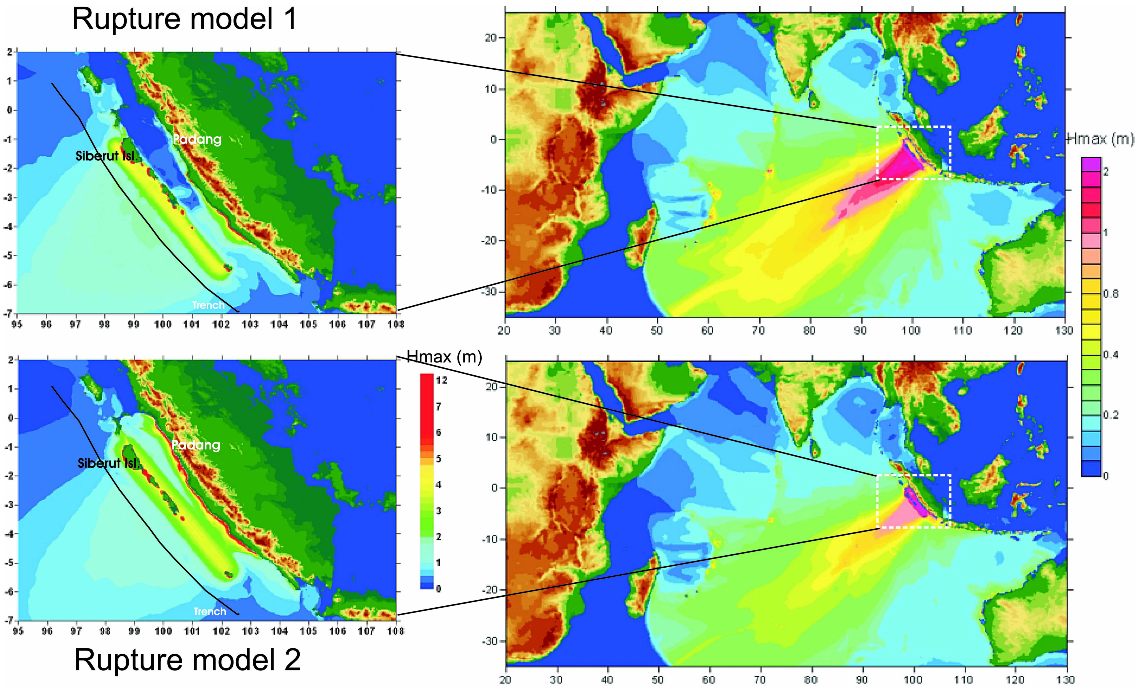

Figure 7.2 Maximum tsunami heights after the earthquake from rupture model 1 (upper panels) and rupture model 2 (lower panels).

The calculated tsunami wave fields are remarkably different for the considered rupture scenarios. More probable rupture model 1 generates a large tsunami in the seaward direction from the trench but, due to the screening effect of the islands, relatively low, but still dangerous, tsunami waves at the coast near the city of Padang (Figure 7.2, upper section). In contrast, rupture model 2, with the deeper slip maximum, generates very high tsunami waves at the Padang coast, but smaller waves traveling into the open ocean (Figure 7.2, lower section). The resulting maximum heights of the tsunami in Padang induced by rupture models 1 and 2 differ by a factor of more than 5 (Figure 7.3). We emphasize that these two rupture scenarios generating such different tsunamis at Padang have the same magnitude and may be characterized by the same hypocenter parameters. These calculations therefore demonstrate that in order to correctly predict near-field tsunami heights, it is not enough to know magnitude, epicenter location, and fault geometry of the earthquake, but it is also crucially important to know the main features of the slip distribution at depth. Moreover, due to the presence of the islands in the source, even far-field tsunamis appear to be sensitive to the slip distribution at the fault (note the difference in ocean-ward radiated tsunamis for rupture models 1 and 2, Figure 7.2).

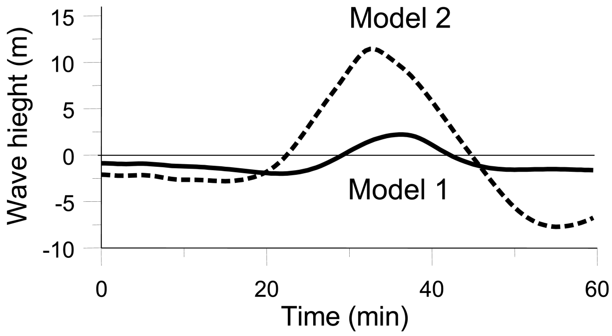

Figure 7.3 Calculated wave heights close to the city of Padang. The solid curve corresponds to rupture model 1 and the dashed curve to model 2. Note that the tsunami hitting the city of Padang is more than 5 times higher for rupture model 2 than for model 1.

Even without islands in the source, a tsunami wave is quite sensitive to the slip distribution at the fault if the distance to the source is less then several hundred kilometers, i.e., so-called local tsunami case [Geist, 1998; Geist and Dmowska, 1999]. In this case, tsunami amplitude is controlled by slip (average slip and maximum slip) at the fault rather than by seismic moment. Therefore reliable prediction of the local tsunami amplitude requires knowledge of higher order features of slip distribution than seismic moment.

7.3.3 How to Estimate Fault Parameters Shortly After the Earthquake?

The question is whether it is possible to resolve the main features of the slip distribution at the fault shortly after the earthquake. To address this question, we recall recent advances in using GPS to investigate the great Sumatran earthquakes of 2004 and 2005 [Vigny et al., 2005; Banerjee et al., 2005; Catherine et al., 2005; Jade et al., 2005; Briggs et al., 2006; Gahalaut et al., 2006; Subarya et al., 2006; Meltzner et al., 2006; Chlieh et al., 2007]. These studies clearly showed that modern GPS techniques allow the measurement of both horizontal and vertical coseismic displacements caused by a giant earthquake, and that those displacements are coherent and very large (meter scale) in the near-field [Briggs et al., 2006; Subarya et al., 2006; Gahalaut et al., 2006]. Moreover, it was also demonstrated that GPS measurements could be inverted for the rupture parameters [Vigny et al., 2005; Banerjee et al., 2005; Catherine et al., 2005; Jade et al., 2005; Briggs et al., 2006; Gahalaut et al., 2006; Subarya et al., 2006; Blewitt et al., 2006; Hoechner et al., 2006; Chlieh et al., 2007].

However, there are two factors that prevent direct use of these observations to predict tsunamis close to the source. First, differences in the inversion results [Vigny et al., 2005; Banerjee et al., 2005; Catherine et al., 2005; Jade et al., 2005; Gahalaut et al., 2006; Subarya et al., 2006] indicate that the solutions are not unique for the case of the current GPS station distribution, although seismic moment (magnitude) of the 2004 earthquake can be estimated quite well [Freymueller, 2005; Blewitt et al., 2006]. Second, tsunami early warning requires high-accuracy real-time GPS measurements, which are still uncommon.

To overcome ambiguity in resolving the rupture parameters, we propose the use of real-time 'GPS-Shield' arrays, located proximal to the expected future source, at the islands in the Sumatra case, to exploit the expected large displacements (both horizontal and vertical) and their trench-perpendicular gradients in the source near-field for tsunami prediction (see Figure 7.1b and Figure 7.1c). Note that the Caltech/LIPI SuGAR GPS network already has continuous GPS sites in some of the appropriate places, but unfortunately none of those sites are equipped to allow for real-time applications yet.

We first explain the basic functionality of the proposed technique for the simplified two-dimensional case and then demonstrate a full three-dimensional example in section 7.5.3. It is worth noting, however, that the two-dimensional approximation is sufficient for determining the deformation in the source near-field, which depends mostly on the rupture process in the closest part of the subduction zone.

In our analysis, we use the following procedure: (1) we place one or more GPS stations along a trench-perpendicular profile; (2) we calculate the input signal, i.e., synthetic surface displacements, for given rupture parameters using a dislocation model for an elastic homogeneous half-space [Okada, 1985] or layered half-space [Wang et al., 2006]; (3) we then define the accuracy for the synthetic ‘observations’ of vertical and horizontal displacements, and also for the relative displacements between the stations; (4) we next generate synthetic observations at each station by randomly perturbing the input signal; (5) the synthetic observations at all stations are then inverted for the rupture parameters using parameterization [Geist and Dmowska, 1999] and a nonlinear inversion method [Press et al., 1992]; (6) finally, we calculate the distribution of the static vertical surface displacement (simulating the initial tsunami waveform) from the obtained rupture parameters and compare the results with the input signal. The above procedure is then repeated for another set of randomly perturbed synthetic observations. As a result, we obtain a number of rupture models and the corresponding vertical displacement curves that may or may not fit the input model, depending on the resolution of the synthetic GPS array.

Let us first place a single GPS station at a distance of 270 km from the trench, which corresponds to the location of Padang. Now assuming a rather modest accuracy for real-time measurements of horizontal displacements (±5 cm) and vertical displacements (±10 cm) (see discussion below), we generate 500 sets of synthetic observations using rupture model 1 or 2. Each set is inverted for rupture parameters and the corresponding prediction for the vertical displacement is shown by the gray (rupture model 1) or black (rupture model 2) curves in Figure 7.4a. It is clear that inverting observations from a single station cannot restore the input signal with sufficient accuracy and therefore cannot issue a reliable prediction for the initial tsunami wave and distinguish between rupture models 1 and 2. Interestingly, while failing to predict the initial tsunami wave, the inversion of observations from a single station still allows us to estimate the seismic moment of the synthetic earthquake with accuracy better than 10% in accordance with estimations by Freymueller [2005] and Blewitt et al. [2006]. This again demonstrates that knowing the earthquake's seismic moment (magnitude), even with a high precision, is not sufficient to predict the local tsunami intensity.

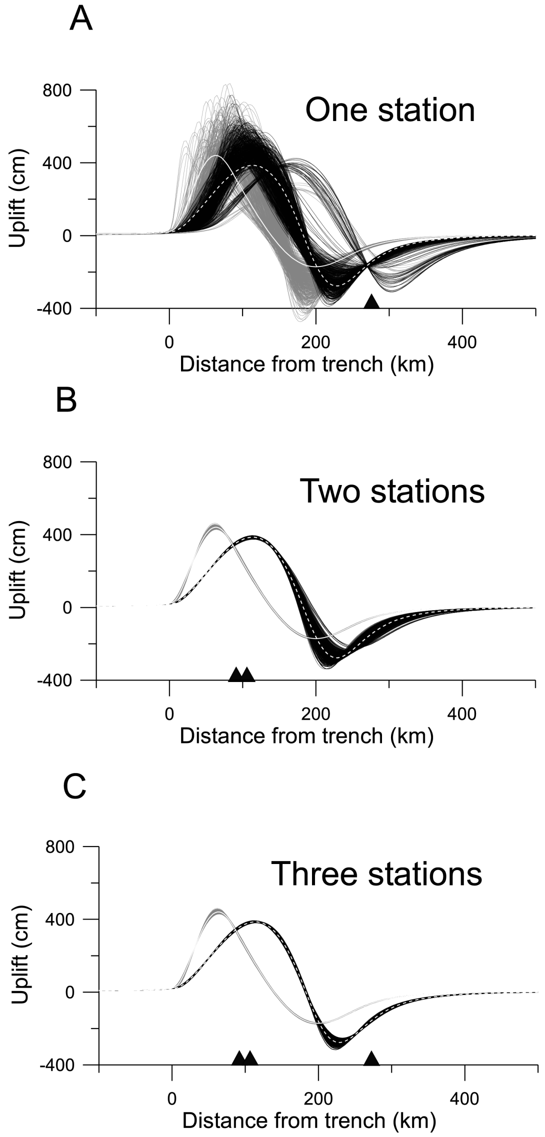

Figure 7.4 (A) Calculated vertical displacements (grey or black curves) using rupture parameters derived from inversion of the synthetic observations at single GPS station placed at Padang (filled triangle) and rupture model 1 or 2 (white solid or dashed curves, respectively). Each gray or black curve corresponds to the inversion using the single set of synthetic observations with synthetic random noise. (B, C) The same as (A), but for an array of two stations placed on Siberut Island (B) and three GPS stations, two on Siberut Island and one at Padang, (C), each shown as filled triangles.

We repeat the above procedure for two stations placed 90 km from the trench with a separation of 20 km, i.e., on Siberut Island located between the trench and Padang. The accuracy of absolute displacements at both stations is assumed to be the same as in the previous example, but the accuracy of measurements of relative displacements between closely spaced (10-30 km) stations (differential GPS) can be much better than that of the absolute displacements [Bock et al., 2000]. Here we assume the relative accuracy to be ±3 cm for vertical and ±1 cm for horizontal displacements (see next section). Using the previously defined GPS array, we performed a set of inversions for both rupture models as input signals (Figure 7.4b). It becomes clear from Figure 7.4b that the two-station array at Siberut Island is quite successful in predicting the initial tsunami height and in distinguishing between rupture models 1 and 2. If the two-station GPS array is complemented by an additional station at Padang, the input signals are restored even better (Figure 7.4c).

From the above exercises, we conclude that a near-field array of GPS stations placed on Siberut Island is able to correctly predict tsunami wave heights and to distinguish between more- and less-dangerous tsunami-generating rupture scenarios for Padang even if its real-time measuring accuracy is modest, i.e., several centimeters.

7.4 Resolving Power of the GPS-Shield Arrays

7.4.1 Expected Measurement Accuracy of the GPS-Shield Arrays

It is well known that GPS analyses based on long-term observations can attain millimeter scale accuracy in the positioning of single receivers. However, a number of problems, such as ionospheric- and tropospheric-induced errors, do not yet allow such accuracy to be achieved with single-epoch measurements in real time [Bock et al., 2000]. Nevertheless, instantaneous GPS positioning techniques [Bock et al., 2000; Bock et al., 2004], as well as the Precise Point Positioning (PPP) techniques [Zumberge et al., 1997] that are based on a combination of the original absolute positioning concept and differential positioning techniques, are rapidly progressing. It has recently been demonstrated that instantaneous GPS positioning using single-epoch measurements and a network of four stations is able to record surface wave displacements with an accuracy of a few mm [Bock et al., 2004]. Based on this result, we infer that accuracies of a few centimeters can easily be achieved for single-epoch measurements of relative displacements between stations separated by a few tens of kilometers. The accuracy of 30 s moving-window smoothed values, required for our purposes, may be even better, although the actual result of smoothing will strongly depend on the error spectrum and needs further analyses.

To access accuracy of single-epoch measurements of absolute displacements, we can use data of a high-rate (1 Hz) GPS station in Yogyakarta (Java) operated for several years by the GFZ Potsdam together with Bakosurtanal and Gadah Maja University. The station is equipped with a precise geodetic dual-frequency receiver. The typical RMS of horizontal displacements at this station is 1-1.5 cm and the RMS of vertical displacements is close to 2-3 cm. This station has continuously recorded GPS data during the catastrophic Yogyakarta earthquake of 26 May 2006 (Mw = 6.3), the epicenter of which was located at a distance of about 30 km from the GPS site. The preliminary processing of the station data clearly shows a horizontal static displacement, which is approximately 2 cm in the north component (Figure 7.5). To our knowledge, this was the first time that 1-Hz GPS observations were recorded before, during, and after an earthquake in the Indonesian region. It demonstrates that the GITEWS real-time GPS observation technique is adequate to measure absolute horizontal displacements with a precision of about 2 cm. Taking into account observed RMS of the vertical displacements of about 2-3 cm, we can also safely assume that the accuracy of ±5 cm can be achieved for the single-epoch measurements of vertical displacements using GITEWS technique.

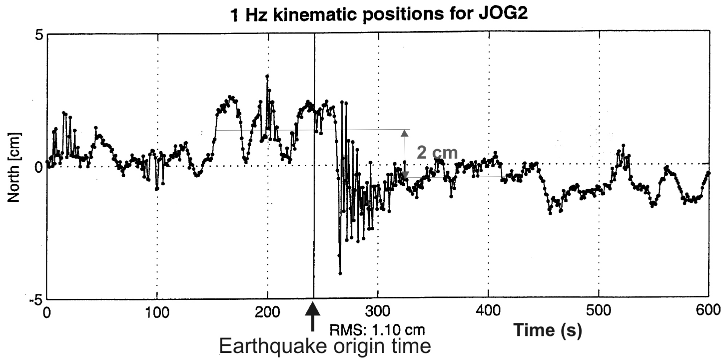

Figure 7.5 Northern displacement component at the high-rate GPS station JOG2, located near the city of Yogyakarta (Java) with the record of the Yogyakarta earthquake of May 26, 2006 (Mw=6.3).

Based on the above estimations, we use three sets of accuracy values in the following resolution tests. In set 1, hereafter called 'realistic,' the accuracies for absolute vertical and horizontal displacements are assumed to be ±5 and ±2.5 cm, respectively, while accuracies for relative displacements at closely spaced stations are assumed to be ±1.5 and ±0.5 cm for vertical and horizontal displacements, respectively. In set 2, hereafter called 'conservative,' all errors are doubled. In set 3, hereafter called 'pessimistic,' all errors are doubled again.

Table 7.2 Parameter ranges assumed in two-dimensional inversion.

Updip depth of a fault (z_l)	10.5-15 km
Rupture zone width (W)	100-300 or 225-275 km
Average slip (U_{mean})	2.5-15.5 m
Dip angle (φ)	Precise (12°) or 10°-15°
Asymmetry parameter (q)	0.1-0.9

7.4.2 Resolution Tests

We now address a question of how the resolving power of the near-field GPS (GPS-Shield) arrays depends upon (1) their distance from the trench, (2) the accuracy of displacement measurements at the stations, and (3) uncertainty of our knowledge about the fault geometry. To do so, we consider input signal according to rupture model 1 and array of two stations with 20 km spacing between the stations. Using the multiple inversion procedure as described above, we analyze how well the particular array can resolve seismic moment, average displacement at the fault and location of displacement maximum at the fault. First we assume that the dipping angle of the fault is known but other parameters can be varied over a very large range (Table 7.2). The results of this analysis are presented in Figure 7.6, which shows the normalized RMS difference between the inverted values of those parameters to their input values versus distance of the GPS array from the trench. Different curves correspond to different assumptions on the accuracy of the displacement measurements. As we see from Figure 7.6, all parameters are resolved best if the array is located just above the maximum slip at the fault (80-90 km from the trench). By moving the array landward the resolution decreases, but it remains quite good for all parameters until the array is moved away from the surface projection of the rupture zone. Arrays located still farther from the trench strongly decrease their resolution in respect to average slip and location of the slip maximum, and at distances more than 100 km landward from the down dip limit of the rupture zone, the resolution for these parameters becomes poor, similar to the resolution which can be achieved by a single GPS station. However, the resolution for the seismic moment decreases much slower with increasing distance and remains quite good even if the GPS array (or single GPS station) is located by more than 500 km away from the trench.

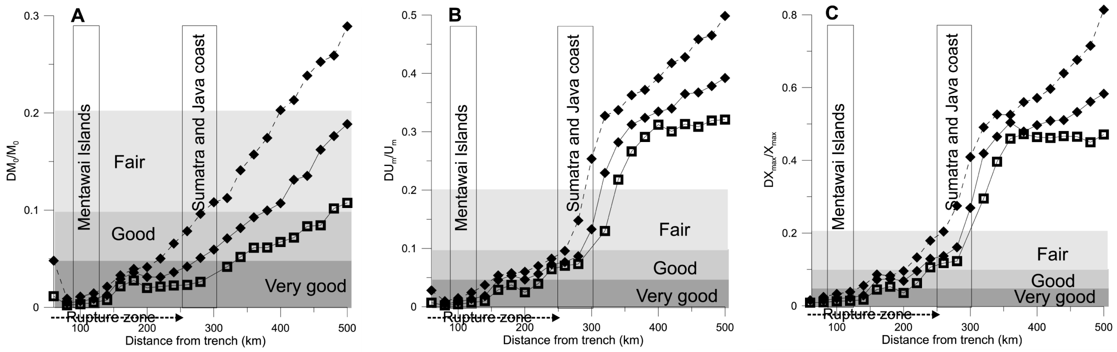

Figure 7.6 Root mean square (RMS) of the deviation of the inversion results from the input (rupture model 1) as a function of the distance from the trench for the two-station GPS array with the station separation of 20 km. (A) Normalized seismic moment; (B) Normalized average displacement at the fault and (C) normalized horizontal coordinate of the slip maximum at the fault. Different curves correspond to different assumptions about the accuracy of the GPS measurements. Solid curves with squares correspond to the "realistic" set of accuracy numbers, solid curves with rhombs to the "conservative" set and dashed curves with rhombs to the "pessimistic" set (see text for definitions). In the inversion, the dipping angle of the fault is assumed to be known (12°), and the width of the rupture zone is assumed to be poorly constrained (lying between 100 and 300 km).

The major conclusions from Figure 7.6 are as follows: (1) an array of closely spaced GPS stations aligned along a trench-perpendicular line can resolve seismic moment (magnitude) of the rupture with very high accuracy even if it is located several hundred kilometers from the trench; (2) the array can do a much better job than just estimating seismic moment, i.e., resolve the rupture parameters like average displacement at the fault and location of the displacement maximum, with accuracy sufficient for tsunami prediction, provided it is located above the rupture zone; (3) if the array is placed less than some 100 km away from the rupture zone, it still can resolve more than just the seismic moment, but the accuracy strongly reduces while the array is moved farther away from the rupture zone.

The higher the accuracy of the measurements at single GPS stations, the larger is the distance from the trench at which GPS array can resolve the rupture parameters. For instance, at the distance of array from the trench of 300 km, the resolution of the arrays measuring with 'realistic' accuracy is by two to three times higher than the resolution of the arrays measuring with 'pessimistic' accuracy (Figure 7.6).

Now let us assume that some additional data (e.g., long-term seismic and GPS observations) constrain the width of the rupture zone with relatively high accuracy of ±25 km rather than ±100 km as in the previous test. In this case, the resolution of the average slip at the fault is greatly improved, while location of displacement maximum is resolved only slightly better and resolution of seismic moment remains the same as in the previous test (compare Figure 7.7 with Figure 7.6).

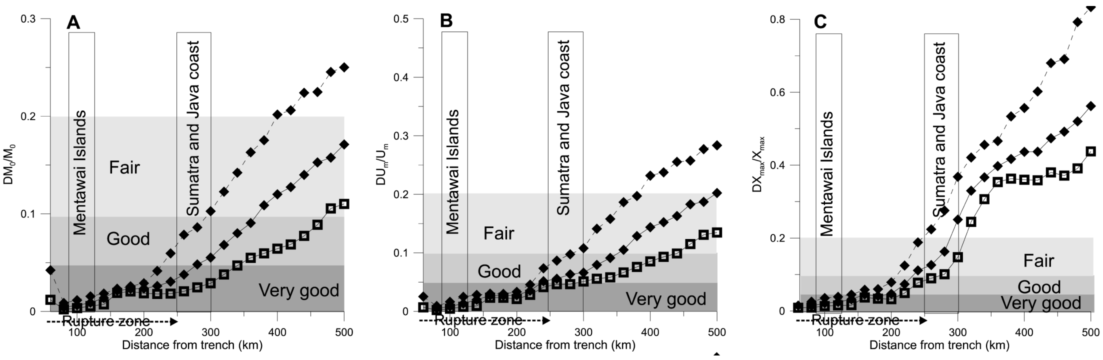

Figure 7.7 The same as Figure 7.6 but for the inversion with the better constrained (+-25 km) width of the rupture zone.

It was recently demonstrated [Banerjee et al., 2005] that slip inversions from GPS data are very sensitive to assumed fault geometry, especially when relying on the near-field data. That is, the lack of precise dip/geometry information may add significantly to the uncertainty in the slip parameters obtained. We test this possibility using similar resolution tests as before but assuming in inversion that the width of the rupture zone is poorly constrained (as in the first test) and that the angle of subduction zone is unknown and may vary in inversion between 10° and 15° (with actual value of 12°). The results of this test (Figure 7.8) confirm that uncertainty in subduction zone geometry can significantly reduce accuracy of estimating rupture parameters (especially location of slip maximum) at islands and Sumatra-Java coasts (compare Figure 7.8 with Figure 7.6).

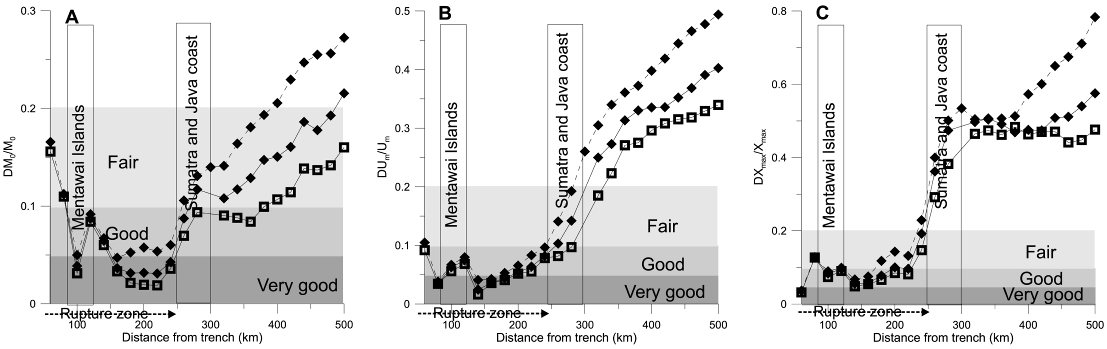

Figure 7.8 The same as Figure 7.6 but for the inversion with the unknown dip angle of the fault lying between 10-15°.

From the above tests, it is clear that the Mentawai islands in front of Sumatra are the best places to install GPS arrays. The inversion results are particularly good if fault geometry is also constrained by other observations. The GPS-Shield arrays at Sumatra and Java coasts (250-300 km from the trench) can be used to precisely estimate the seismic moment of a giant earthquake. In addition, the average displacement and location of displacement maximum could be also estimated if the fault geometry is well known and the accuracy of real-time GPS measurements is better than few centimeters. The precise mapping of the seismogenic-zone geometry can be accomplished with long-term observations using broadband seismometers and GPS stations, while the few-centimeter accuracy of real-time GPS-Shield arrays measurements is quite realistic, as discussed in the previous section.

7.5 The GPS-Shield Concept for Sumatra and Java

7.5.1 Basic Concept

Key elements of the 'GPS-Shield' concept for Sumatra are near-field GPS arrays operating in real time. Frontal part of the array consists of two (or more) GPS stations located on the Mentawai islands between the Sumatran coast and the trench (Figure 7.9). Stations in the array are closely spaced (10-20 km) and aligned perpendicular to the trench, i.e., parallel to the expected gradient of surface coseismic displacement. One master station and several slave stations are all equipped with precise geodetic dual-frequency receivers, a digital meteorological sensor, data processor unit, and radio modems. The array master station continuously receives high-rate GPS-observations at 1 Hz (and at 10 Hz in the case of an earthquake) from its slave station(s) and calculates the coordinate differences for each single measurement epoch in real time, as suggested by Bock et al. [2000; 2004].

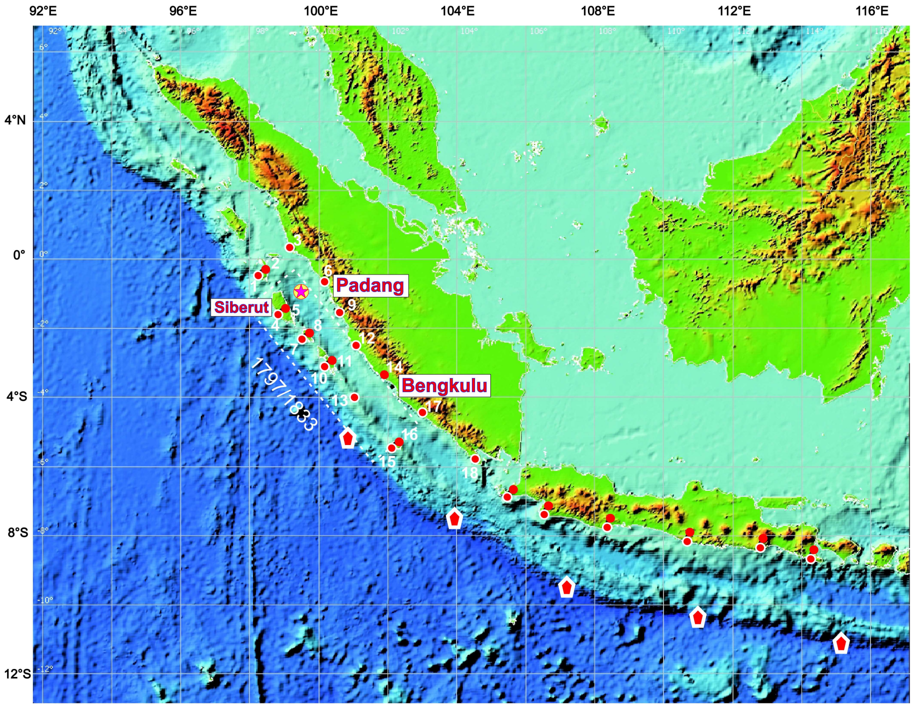

Figure 7.9 Concept of the GPS-shield system in the region of Sumatra and Java. Red circles are real-time GPS stations. Red circles with white rings are the same GPS stations that are also equipped with a broadband seismometer and strong motion recorder. The key elements of the system consist of arrays of two (or more) GPS stations (GPS-Shield arrays) located on the islands, immediately above the potential rupture zone and at the Sumatra and Java western coasts. The GPS buoys (red diamonds) are placed where no islands are located between the trench and Sumatra and along the Java trench. The zone of possible future earthquake at the site of the past 1787/1833 earthquakes is indicated. The dashed box and star indicate the rupture zone and epicenter of the modeled earthquake. The numbers mark the sites where are calculated the synthetic seismograms and which are used for 3D inversion of displacements for rupture parameters.

The island-hosted parts of arrays are complemented by GPS stations located directly at the Sumatran coast along the same lines. The latter 'control' stations, serve to improve inversion of the rupture parameters and to check the internal consistency of a solution. The GPS-Shield arrays are set along the trench with the spacing appropriate to resolve major trench-parallel slip heterogeneity, which, based on analyses of the 2004 and 2005 events, is expected to be approximately 100-200 km for the giant earthquake. In the case where there are no islands between the trench and Sumatra, we suggest the use GPS-

Shield arrays at the Sumatran coast and ocean buoys equipped with GPS devices and bottom pressure sensors. The whole system is completed with GPS tide gauges on the islands.

No islands are located between the trench and Java (Figure 7.9). However, as shown in the previous section, GPS-Shield arrays at the Java coast can still be used in this case to estimate higher order features of slip distribution at the fault than seismic moment. Important preconditions to achieve this are that the arrays are placed as close as possible to the trench and that the geometry of the rupture zone is constrained using long-term seismic and GPS observations. In the case of Java, the GPS-Shield system should consist of several GPS-Shield arrays placed along the Java western coast at a distance of about 100-200 km to resolve trench-parallel heterogeneity of the potential rupture (Figure 7.9). A number of ocean buoys equipped with GPS devices and bottom pressure sensors should be placed close to the trench to verify and specify tsunami waveform predictions derived from the land observations (Figure 7.9).

7.5.2 System Functionality Test for the Future Sumatra Earthquake

To examine the functionality of the proposed system for Sumatra, we performed a three-dimensional simulation of the entire rupture process of the earthquake largely repeating the 1797/1833 events. Synthetic seismograms for the scenario earthquake are calculated using the deterministic Green's function method [Wang, 1999] based on the IASPEI91 elastic layered-Earth model [Kennett and Engdahl, 1991]. In this simulation, the rupture starts in the deep part of the seismogenic zone northeast of Siberut Island (star in Figure 7.9) and propagates updip and southward in a trench-parallel direction circularly with a velocity of 2.5 km/s. The focal parameters and the slip distribution are listed in Table 7.1. The ruptured area (692 × 250 km) is discretized into about 2600 patches (each of 14 km × 5 km size) being treated as point sources. Each point source is composed of a set of Brune's omega-square subevents [Brune, 1970], which are distributed according to the Gutenberg-Richter law in size and randomly in time. It is necessary to introduce the randomness into the source time function so that adjacent point sources are reasonably coherent at low frequency, but incoherent at high frequency [e.g.Irikura, 1983]. The seismic moment of each point source is released within a time comparable to the rise time of the entire earthquake. By assuming an average stress drop of 20 MPa, the rise time of the present scenario earthquake (Mw ~9.1) is estimated to be ca. 100 seconds according to the empirical relation of Boore [1983].

According to this model, the first seismic signal arrives at the Siberut and Padang stations less than 20 s after the rupture begins. This signal or much more powerful S wave signal coming some 10-20 s later (Figure 7.10) can be used to switch the observational network into a high-sampling rate mode. At about 30-40 s, the GPS stations closest to the rupture zone begin to record large displacements simultaneously with arrivals of S waves and first surface waves [see also Freymueller, 2005]. After some 3 minutes, both vertical and horizontal displacements at GPS stations close to the epicenter almost approach their static values (Figure 7.11). The displacement oscillations with amplitude up to 30-50 cm continue until the rupture is propagating and generating surface waves, i.e., about 3-5 minutes in our model. Note however that these oscillations can be efficiently smoothed out by 30 s moving average. Thus, the first inversion for the rupture parameters using GPS data can already be carried out at about 3 minutes after the rupture begins. It is important that even at this early stage, two scenarios (rupture model 1 and 2) can be clearly distinguished.

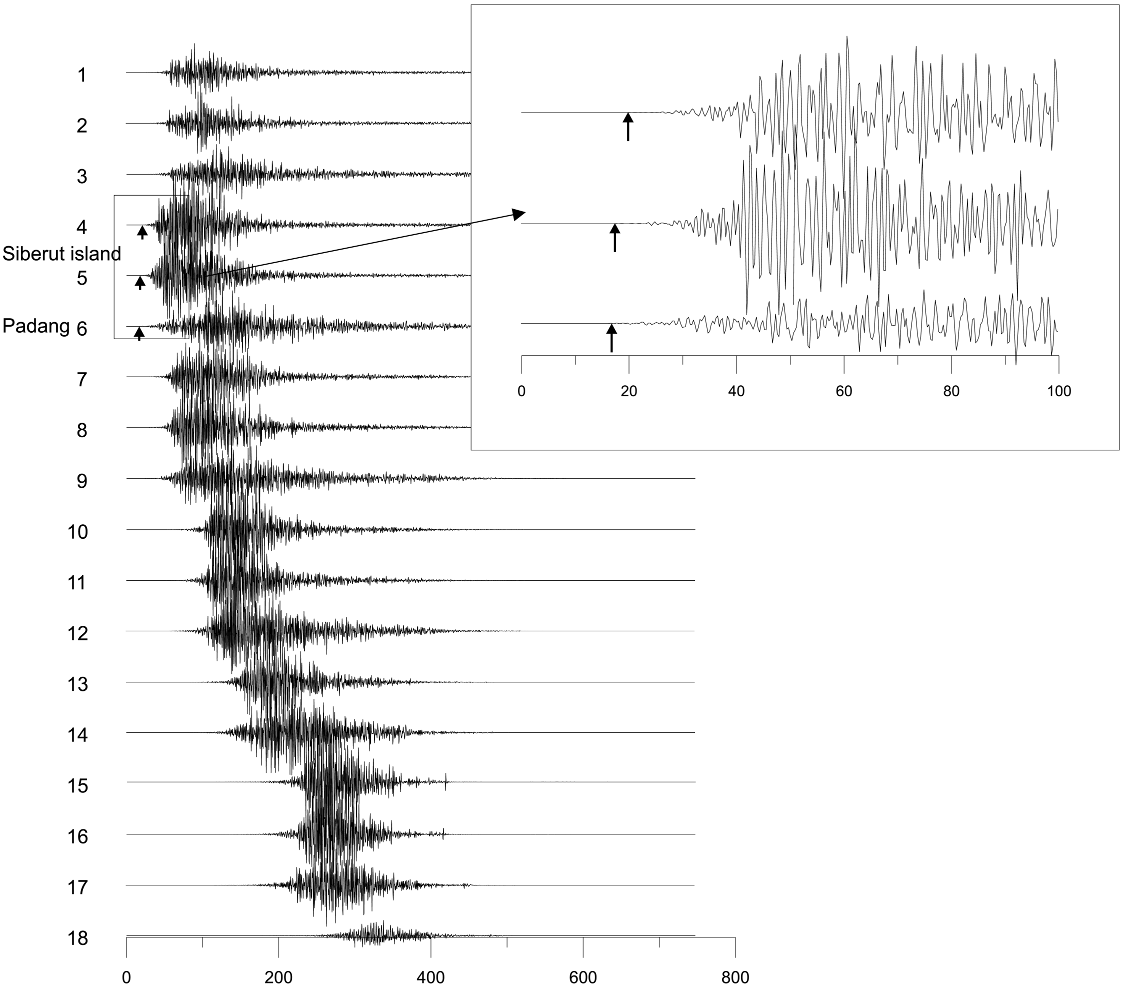

Figure 7.10 Calculated synthetic vertical acceleration seismograms (low-pass filtered) at the sites numbered in Figure 7.9.

After 6-7 minutes, static displacements are fully established at all stations, and rupture parameters can be resolved (see section 7.5.3). By this time, the tsunami wave has already passed the tide gauge at Siberut Island, allowing the further verification of the estimated rupture parameters. Therefore we expect that the qualified tsunami warning for the entire Sumatra can be issued 6-7 minutes after the rupture begins and even earlier for the region of Padang. At that time it will be possible to accurately predict the tsunami wave heights and thus distinguish between catastrophic and less dangerous scenarios. This leaves more than 18 minutes before the tsunami hits the coast at Padang.

In addition, we suggest complementing at least some of the master GPS stations in arrays with broadband seismometers and strong motion recorders (Figure 7.9). The strong motion recorders can provide additional information about the rupture parameters [Ji et al., 2002], while the broadband seismometers can be used over the long term to map the seismogenic zone topography. Moreover, the seismometers can also provide information about possible asperities by mapping the distribution of b values [Wyss and Stefansson, 2006]. It would also be useful to install tiltmeters at Sumatra and Java coasts to measure coseismic deformations where resolution of GPS-Shield arrays is relatively low.

Finally we can compare our synthetic displacement seismograms with the real data for giant earthquakes. The raw observations from the December 2004 earthquake at SAMP

(Sampali, Sumatra) show about 17 cm peak-to-peak variation after the earthquake, and this substantial variation continues for some 10-15 minutes after the main shock [Freymueller, 2005; see also Figure 1 of Blewitt et al., 2006]. In our model, station 18 (see Figure 7.9) is at the similar distance from the rupture as SAMP. As we see from Figure 7.11, the amplitude of synthetic displacement oscillations at station 18 is also about 15-20 cm peak-to-peak as at SAMP. Different is only the duration of oscillations, which is about 4 minutes instead of more than 10 minutes at SAMP. This difference is likely due to the different duration of our model rupture (5 minutes) and rupture of 26 December 2007, which is known to be longer than 10 minutes.

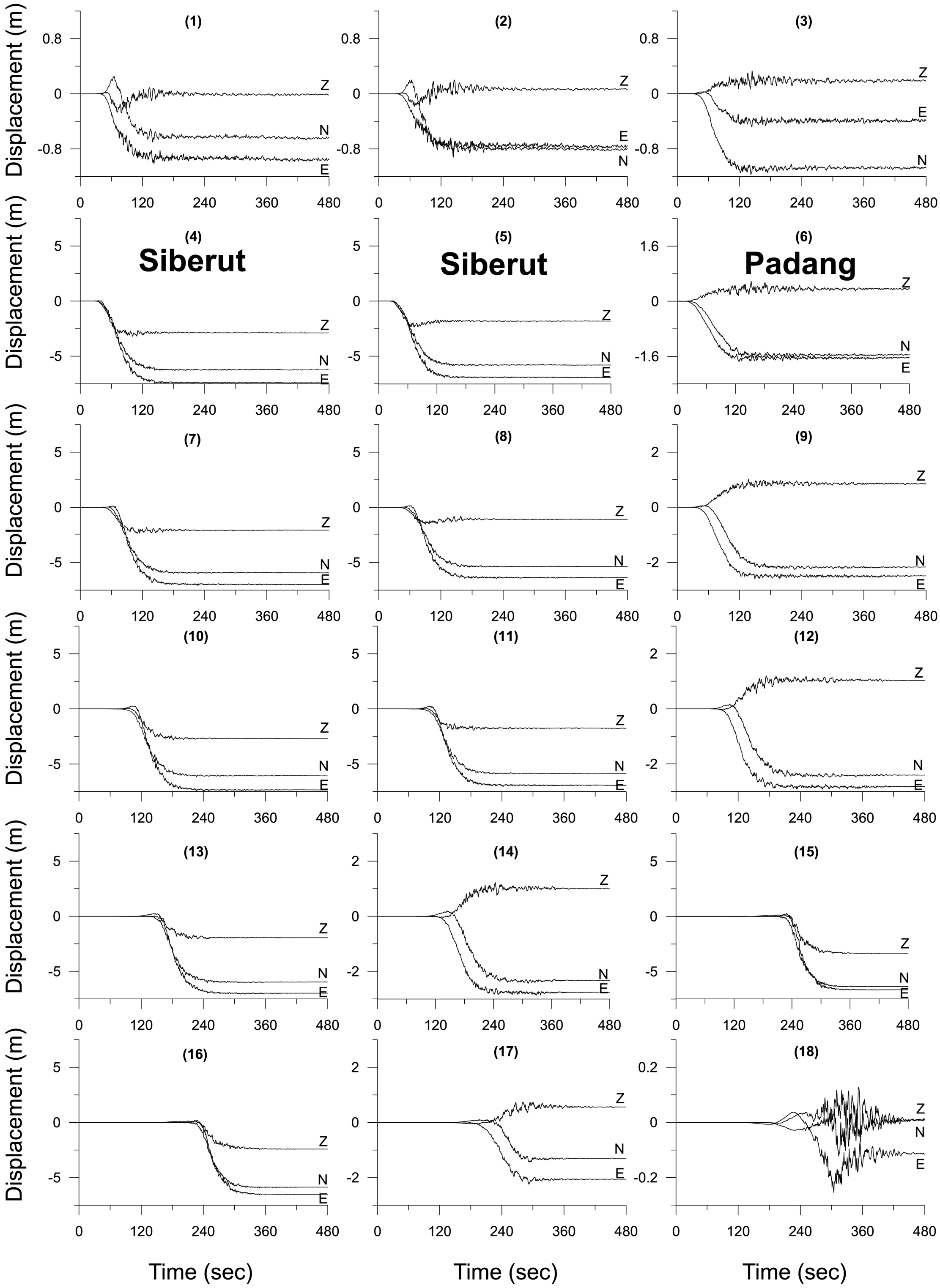

Figure 7.11 Calculated synthetic displacement seismograms at the sites numbered in Figure 7.9. The x-axis is the time in seconds since the time of the origin of the earthquake, and the y-axis is the displacement in meters. The north, east and vertical (downward positive) component are indicated by letters, N, E and Z, respectively. Note that amplitude scales are different for different figures. Seismograms at two stations on Siberut Island and in the city of Padang are especially indicated.

7.5.3 Three-Dimensional Inversion of Static Displacements for Rupture Parameters

In this section we present results of three-dimensional inversions for rupture parameters of synthetic observations at GPS stations marked by numbers in Figure 7.9. We explore three rupture models with slip distributions shown in the upper section of Figure 7.12, i.e., rupture models 1 and 2 and a model with checkerboard distribution of slip at the fault. Inversion is accomplished for distributions of amplitude of the slip vector and for the rake angle in a number of rectangular patches (subfaults), which cover the potential source region assuming that dip angle of the rupture plane is known to be 12°. We employ a quasi-Newton line search technique to minimize squares of differences of model-predicted and 'observed' (synthetic) displacements at GPS stations, simultaneously minimizing differences of slip magnitudes and rakes between adjacent subfaults. Displacements are calculated using Green's functions precomputed for the layered Earth model using technique by Wang et al. [2006], and the 'observed' (synthetic) displacements at GPS stations are perturbed with random noise of ±10 cm for vertical displacements and ±5 cm for horizontal displacements.

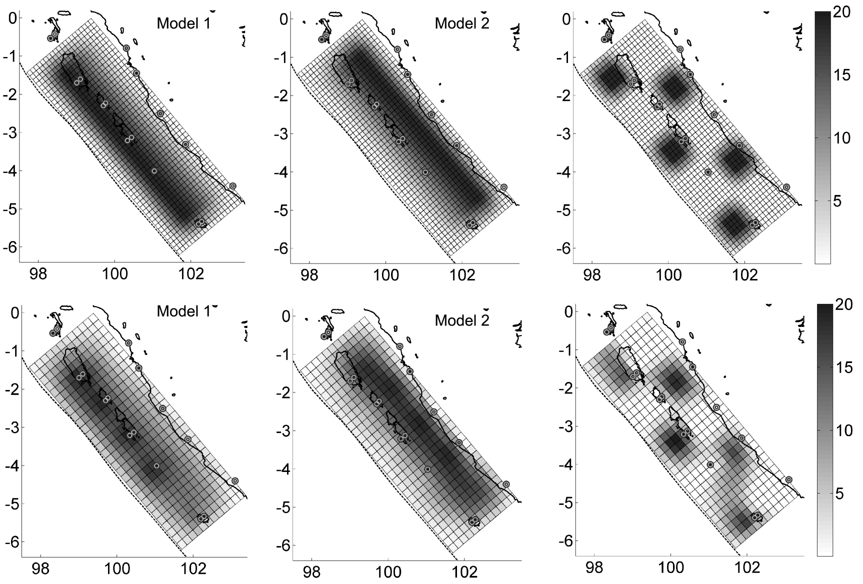

Figure 7.12 Input (upper panel) and inverted (lower panel) distributions of slip at a fault for rupture models 1 (left column), 2 (middle column) and model with checkerboard distribution of slip (right column). Circles mark locations of synthetic GPS stations.

As it is demonstrated by the results of inversion (lower section of Figure 7.12), observations at GPS-Shield stations at islands and at the Sumatran coast allow robust estimation of rupture parameters for all tested rupture models. Rupture models 1 and 2 can be distinguished very well, and in accordance with the two-dimensional tests, the best resolution is achieved where the GPS stations are closest to the source. See also Animations 1-3 of the supplementary material showing results of real-time inversions of synthetic displacements.

Based on the slip distributions derived from three-dimensional inversion (lower section of Figure 7.12), we calculate the propagation of the tsunami waves for rupture models 1 and 2 and compare results with 'observed' waves, i.e., waves calculated for the input slip distributions (upper section of Figure 7.12). Results of this comparison are presented in Figure 7.13 for synthetic tide gauges located near the cities of Padang and Bengkulu. As one can see, the predicted tsunami waves are quite similar to the 'observed' waves. It is also clear that three-dimensional inversion results allow distinguishing rupture models 1 and 2 very well.

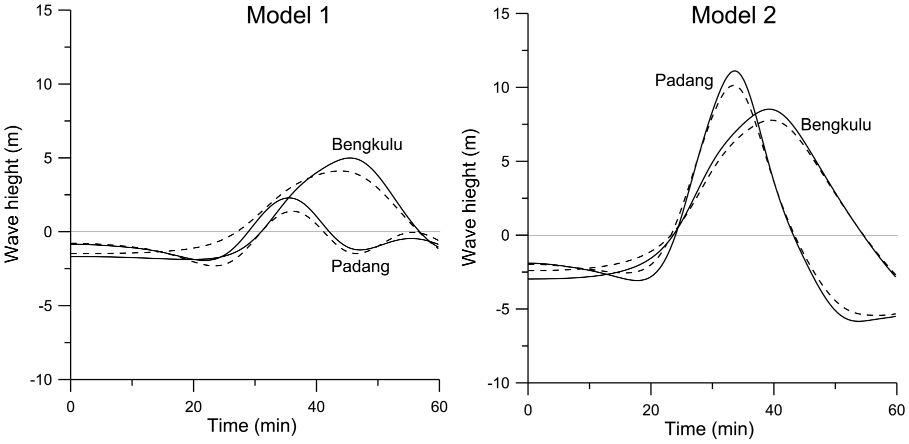

Figure 7.13 Comparison of "predicted" (dashed curves) and "observed" (solid curves) wave heights at tide gauges located near the cities of Padang and Bengkulu for rupture model 1 (left graph) and model 2 (right graph). The "predicted" wave fields are calculated based on the slip distributions derived from 3D inversion of synthetic GPS observations (lower section of Figure 7.12), while the "observed" wave fields are calculated based on the input 3D slip distributions (upper section of Figure 7.12).

We have also checked the three-dimensional resolution of GPS-Shield arrays with reduced number of stations. If no stations are installed at the islands, the resolution of the array significantly decreases, in accordance with the two-dimensional tests of section 7.3.3. On the other hand, an array with all island stations in place but no stations at the Sumatra coast (subarray A) as well as an array with single, instead of double, stations at the islands and with all stations at the Sumatra coast (subarray B), have almost the same resolution as the complete array. Thus, theoretically these reduced arrays can also be efficiently used for tsunami early warning. They, however, strongly lose their resolution if any of the stations fails. In contrast, the complete GPS-Shield configuration, presented in Figure 7.9, performs well if any station fails. Moreover, results of inversion of displacements measured by the complete array may be checked for internal consistency by comparison of independent inversions for the subarrays A and B, thus increasing solution confidence.

7.6 The GPS-Shield for Northern Chile and Elsewhere

Application of the proposed GPS-Shield concept is not limited geographically to Sumatra. As we have shown above, GPS arrays are efficient in resolving tsunami-controlling rupture parameters everywhere, provided they are placed just above or closer than 100 km to the rupture zone. Other regions where giant earthquakes and tsunamis are expected include Cascadia [Hyndman et al., 1996; Mazzotti et al., 2003; Chlieh et al., 2004] and the coast of Chile, particularly northern Chile where a giant earthquake may occur in the near future [Chlieh et al., 2004]. Using the rupture parameters of the 1960 Great Chilean Earthquake [Barrientos and Ward, 1990] (Table 7.1), the same resolution test as before demonstrates that arrays of two or three closely spaced GPS stations at the coast can provide a confident estimate of the initial tsunami height at the corresponding segment of the subduction zone along the entire north-Chilean coastline (Figure 7.14). Very high resolution can be achieved if the GPS-Shield array is placed close to the city of Antofagasta that is located only some 100 km from the trench. The lowest resolution is expected for the city of Arica that is located far most from the trench. But even in this case, initial tsunami waves can be estimated reasonably well (Figure 7.14).

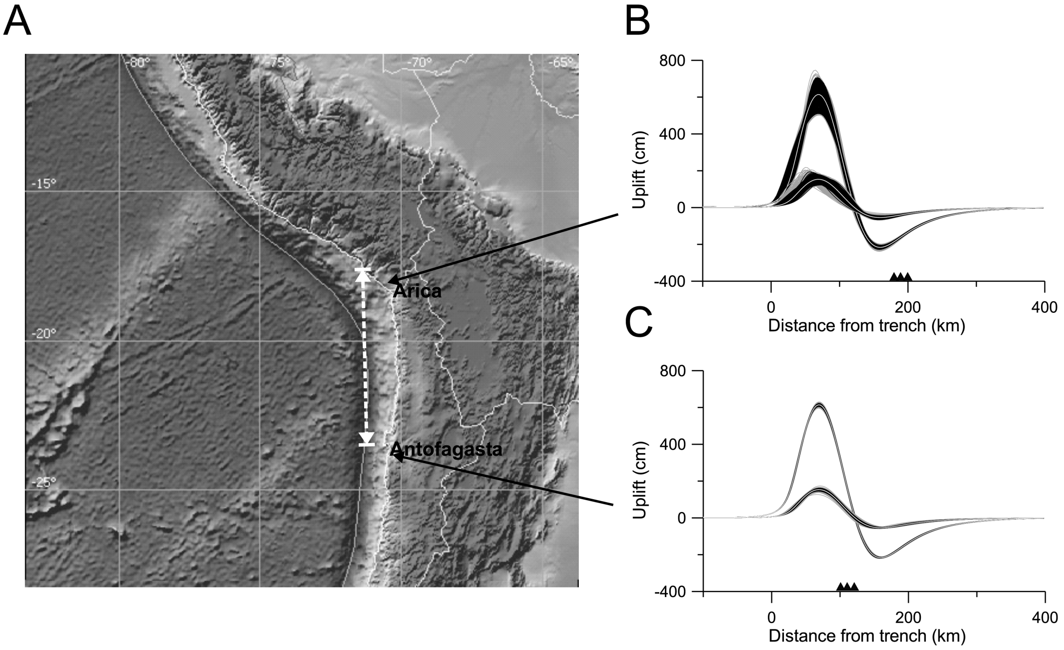

Figure 7.14 (A) The expected location of the rupture zone in northern Chile (marked by the white dashed line). (B) Static vertical displacements for the earthquake with parameters similar to those of the Great Chilean Earthquake (upper white solid curve) and an earthquake with a 5-times smaller average slip at the fault (lower white solid curve). Black curves are calculated vertical displacements using rupture parameters derived from the inversion of the synthetic observations at three stations (filled triangles) separated by 10 km, placed at the coast near the city of Arica. Each black curve corresponds to the inversion using a single set of synthetic observations with random noise of +-10 cm and +-5 cm for vertical and horizontal absolute displacements and +-3 cm and +-1 cm for vertical and horizontal relative displacements, respectively ("conservative" accuracy set). Grey curves show the same but with twice as much noise ("pessimistic" accuracy set). (C) The same as (B), but for the city of Antofagasta, which is located closer to the trench than Arica.

Preliminary analysis implies that the GPS-Shield concept can potentially also be applied to the entire coast of Chile, the Middle America subduction zone, the Pacific Northwest, Southern Japan, the Aleutian and Kuril Islands, Kamtchatka, and Alaska, as well as to the subduction zones in the Mediterranean, etc. (Figure 7.15). Moreover, by providing fast and robust estimation of the initial tsunami waveforms, GPS-Shield arrays may also be implemented for far-field tsunami warnings, thus becoming an important component of the global tsunami early warning system [Sobolev et al., 2006] (see also Figure 7.15). It looks like that the GPS-Shield arrays can be efficiently used at most of the tsunamigenic active margins. The best results in predicting tsunami waves within less than 10 minutes of an earthquake can be obtained where the land is located closer than 100 km to the seismogenic zone (solid curves in Figure 7.15). If the land is located at larger distances, but still closer than 500 km from the trench (dashed curves in Figure 7.15), the GPS-Shield arrays can be used at least for fast and precise estimation of the seismic moment of large earthquakes. It is also important to mention that the global GPS-Shield arrays will in fact serve at least two important purposes. In addition to their tsunami-warning function described above, the arrays will also allow long-term deformation monitoring in most convergent plate boundaries. This function will provide important data for constraining global geodynamics and, in particular, the processes that lead to large megathrust earthquakes.

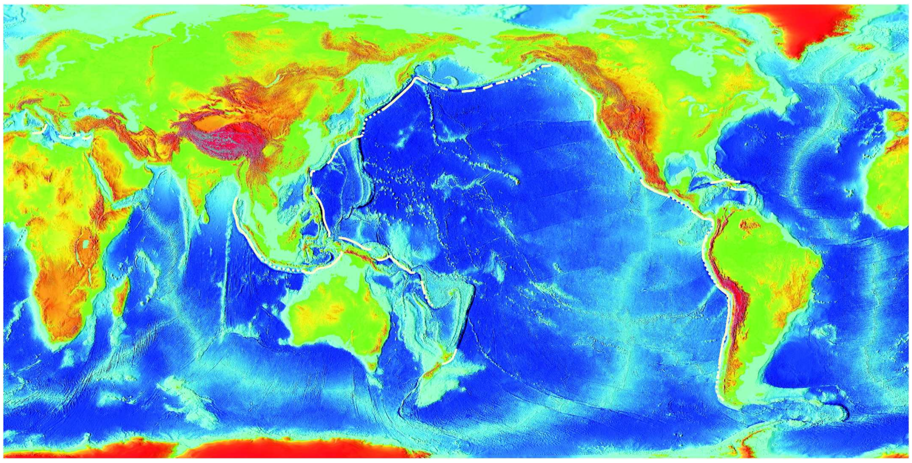

Figure 7.15 Global application of the GPS shield concept. Solid curves indicate subduction zones where the land is located closer than 100 kilometers to the seismogenic zone, i.e., where the real-time GPS shield arrays likely can resolve major features of slip distribution on the fault. Dashed curves indicate zones where the GPS shield arrays can at least resolve the seismic moment of the closest large earthquakes.

7.7 Concluding Remarks

We demonstrated that in the presence of massive islands close to the trench, the tsunami height becomes especially sensitive to slip distribution at the fault. In the case of giant earthquakes west of Sumatra, wave heights at Padang may differ by more than a factor of 5 for ruptures having the same seismic magnitude but different slip distribution. Therefore reliable prediction of tsunami wave heights in such cases cannot be provided using traditional, earthquake-magnitude-based methods. This is also true for the local tsunami in general, as the source near-field tsunami height is controlled by the slip at the fault (mean slip and maximum slip) rather than seismic moment of the earthquake.

The reliable prediction of tsunami waves can be issued within less than 10 minutes of an earthquake by incorporating special types of near-field GPS arrays (‘GPS-Shield’), which can resolve higher order features of the slip distribution at the fault than seismic moment. Frontal stations in the arrays are closely spaced (10-20 km) and all stations are aligned perpendicular to the trench, i.e., parallel to the expected gradient of surface coseismic displacement. In the case of Sumatra and Java, the GPS-Shield arrays should be placed along the trench at Mentawai Islands, located between the trench and Sumatra and directly in the Sumatra and Java western coasts. In particular, the GPS-Shield array with stations placed on Siberut Island and near Padang, even with a modest measuring accuracy of several centimeters, is able to correctly predict tsunami wave heights and to distinguish between more and less dangerous tsunami-generating rupture scenarios for Padang.

The resolution tests show that the GPS-Shield array or even single GPS station can resolve seismic moment (magnitude) of the rupture with very high accuracy even if it is located several hundred kilometers from the trench. The array can do a much better job than just estimating seismic moment and can resolve average displacement at the fault and location of the displacement maximum with accuracy sufficient for tsunami prediction, provided it is located above the rupture zone. If the array is placed less than approximately 100 km away from the rupture zone, it still can resolve more than just seismic moment, but the accuracy strongly reduces while the array is moved farther away from the rupture zone.

To improve resolution of the GPS-Shield arrays, it is important to constrain as precise as possible the geometry of the possible rupture zone. This can be accomplished with long-term observations using broadband seismometers and GPS stations.

The GPS-Shield concept is not restricted regionally to Sumatra and Java. We demonstrated that the ‘GPS-Shield’ could also be applied to northern Chile, where a giant earthquake may occur in the near future. Moreover, this concept may be applied globally to many other tsunamigenic active margins where the land is located above or close to seismogenic zones.

In fact, the global GPS-Shield arrays will serve at least two important purposes. In addition to their tsunami-warning function described above, the arrays will also allow long-term deformation monitoring in most convergent plate boundaries. This function will provide important data for constraining global geodynamics and, in particular, the processes that lead to large megathrust earthquakes.

Finally, we summarize benefits of the GPS-Shield concept for tsunami early warning in comparison to what can be achieved by traditional methods based on earthquake magnitudes.

(1) As a minimum, the GPS-Shield arrays placed along the trench will be able to estimate seismic moment (magnitude) of the corresponding sections of a rupture zone (partial magnitude) within just a few minutes of an earthquake. Traditional teleseismic methods allow estimation of the seismic magnitude for the entire rupture and then only more than 10 minutes after an event.

(2) If placed above or close to the rupture zone, the GPS-Shield arrays will be able to resolve major features of slip distribution not only parallel to the trench, but also downdip along the subduction fault, thereby doing a much better job than is possible by just estimating the seismic moment. This will allow much more reliable prediction of tsunami amplitudes, especially in the case of islands above the rupture zone that strongly affect the tsunami-generation process.

(3) The GPS-Shield is also able to capture relatively slow (tens of minutes) post-slip at the fault which is undetectable using seismic methods, but may well contribute to tsunami generation [Lay et al., 2005; Kanamori and Stewart, 1979].

7.8 Appendix A

The parameterization by Freund and Barnett [1976] and Geist and Dmowska [1999] defines the slip distribution in the local downdip fault coordinate x as

$$U = 2U_{mean} x^2 (-2x + 3q) / q^3 \quad \text{if } 0 \le x \le q$$
$$U = 2U_{mean} (2x^3 - 3x^2 - 3qx^2 + 6qx - 3q + 1) / (1 - q)^3 \quad \text{if } q < x \le 1$$

where U_{mean} is the average slip at the fault; x is the local coordinate at the fault, normalized to its width and is 0 at the fault updip edge and 1 at the fault downdip edge; q is the coordinate at which displacement achieves the maximum. In this parameterization, the single fault in two dimensions is defined by the following parameters: fault azimuth, dip angle (), updip depth of a fault (z_1), width of the rupture zone (W), average slip (U_{mean}), and a parameter q describing the asymmetry of the slip distribution.

As demonstrated in Figure 7.16, the above parameterization can accurately describe slip distribution at a cross-section through the actual rupture zone (Great Sumatran Earthquake of 26 December 2004) derived from inversion of GPS observations by Hoechner et al. [2006], which is similar to the inversion results by Chlieh et al. [2007].

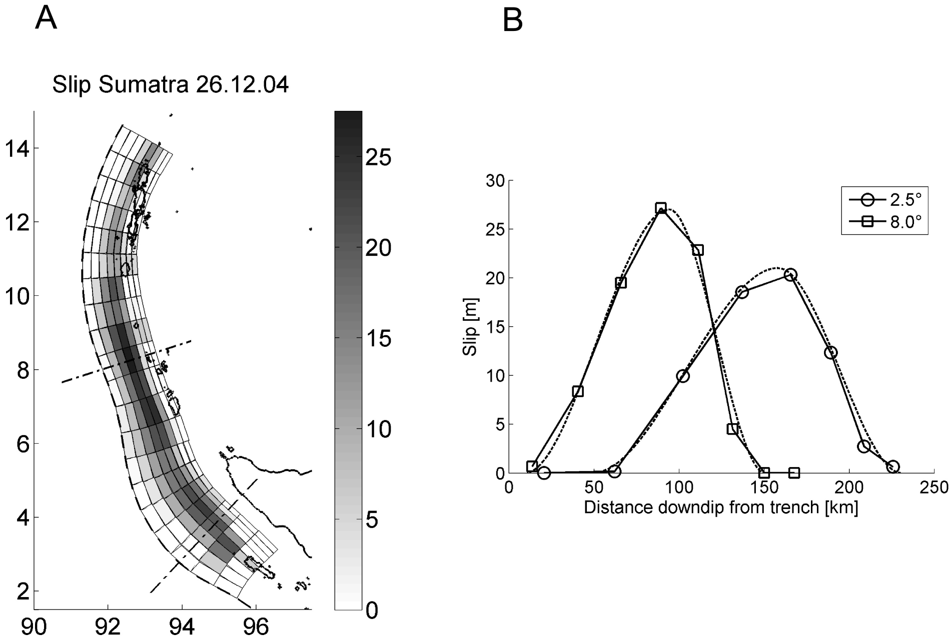

Figure 7.16 (A) Slip distribution in the rupture zone of the Great Sumatra Earthquake of December 26, 2004 from 3D inversion of GPS data after Hoechner et al. [2006]. (B) Slip distributions along cross-sections shown in (A). Solid lines present inversion results and dashed curves show their approximation using parameterization by Freund and Barnett [1976] and Geist and Dmowska [1999].

7.9 Appendix B

This section is not included in the original printed version of the publication, but an animated version of the figure below is available as dynamic content at the JGR web page.

In order to test the performance of the concept concerning timing, we inverted the synthetic displacement seismograms every 30 seconds. The result is illustrated in Figure 7.17. After about 3 minutes the rupture can be tracked almost instantly.

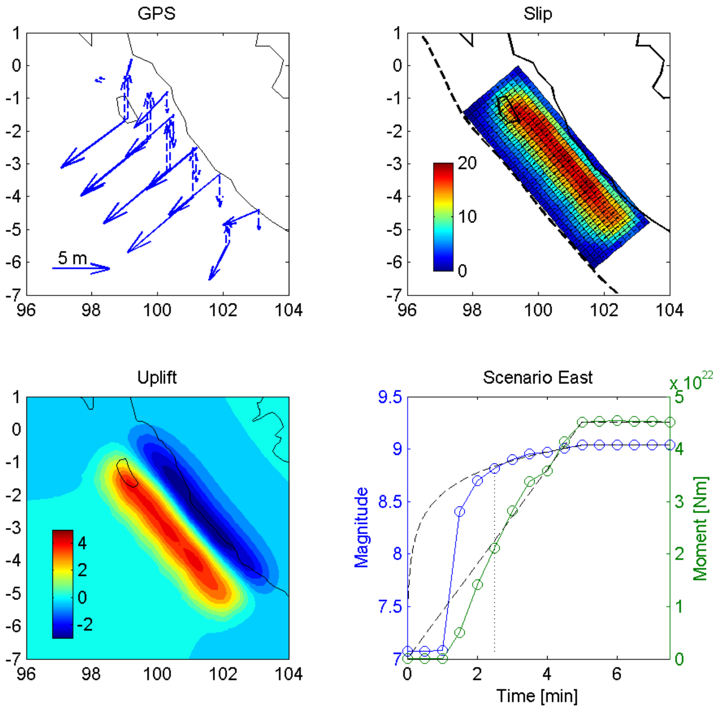

Figure 7.17 Upper left panel: final GPS displacements. Upper right: reconstructed slip distribution. Lower left: associated sea floor deformation. Lower right: dashed lines: actual- and solid lines: inverted magnitude (blue) and moment (green).

7.10 Acknowledgments

This is publication no. 12 of the GITEWS project (German Indian ocean Tsunami Early Warning System). The project is carried out through a large group of scientists and engineers from GeoForschungsZentrum Potsdam (GFZ) and its partners from the German Aerospace Centre (DLR), the Alfred Wegener Institute for Polar and Marine Research (AWI), the GKSS Research Centre, the Leibniz Institute for Marine Sciences (IFM-GEOMAR), the United Nations University (UNU), the Federal Institute for Geosciences and Natural Resources (BGR), the German Agency for Technical Cooperation (GTZ), as well as from Indonesian and other international partners. Funding is provided by the German Federal Ministry for Education and Research (BMBF), Grant 03TSU01. E. Flüh provided unpublished bathymetry data. We are grateful to R. Hackney and K. Fleming for carefully reading the manuscript and to the members of the GITEWS team for useful discussion. Reviews by J. Freymueller, R. Bürgmann, and H. Latief were very helpful to improve the manuscript.

8 Source modeling and inversion with near real-time GPS: a GITEWS perspective for Indonesia

Andrey Y. Babeyko[1], Andreas Hoechner[1], Stephan V. Sobolev[1,2]
[1]Deutsches GeoForschungsZentrum GFZ, Potsdam, Germany
[2]Institute of Physics of the Earth, Moscow, Russia

An edited version of this paper was published in: Natural Hazards and Earth System Sciences, 10, 1617-1627, doi: 10.5194/nhess-10-1617-2010. Received 24 February 2010; revised 22 June 2010; accepted 22 June 2010; published 26 July 2010. Edited by: A. Rudloff. Reviewed by: S. Lorito and another anonymous referee.

8.1 Abstract

We present the GITEWS approach to source modeling for the tsunami early warning in Indonesia. Near-field tsunami implies special requirements to both warning time and details of source characterization. To meet these requirements, we employ geophysical and geological information to predefine a maximum number of rupture parameters. We discretize the tsunamigenic Sunda plate interface into an ordered grid of patches (150×25) and employ the concept of Green's functions for forward and inverse rupture modeling. Rupture Generator, a forward modeling tool, additionally employs different scaling laws and slip shape functions to construct physically reasonable source models using basic seismic information only (magnitude and epicenter location). GITEWS runs a library of semi- and fully-synthetic scenarios to be extensively employed by system testing as well as by warning center personnel teaching and training activities. Near real-time GPS observations are a very valuable complement to the local tsunami warning system. Their inversion provides quick (within a few minutes on an event) estimation of the earthquake magnitude, rupture position and, in case of sufficient station coverage, details of slip distribution.

8.2 Introduction

The GITEWS initiative (German Indonesian Tsunami Early Warning System) was a German response to the catastrophic December 2004 Indian ocean tsunami which devastated Indonesia and other countries across the Indian Ocean. It consists of a consortium of German partners leaded by the German Research Center for Geosciences (GFZ) in close cooperation with a number of research and governmental agencies in Indonesia [Rudloff et al., 2009].

Modern tsunami early warning systems strongly rely on tsunami modeling as an integral part of the system. The Decision Support System (DSS) collects all available sensor data, usually including seismic and ocean measurements (while GITEWS additionally employs near real-time GPS data, see Falck et al. [2010]), and then asks the modeling unit for the tsunami prediction based on the collected observations. To provide such a prediction, the modeling unit of the TEWS (Tsunami Early Warning System) essentially solves an inverse problem: given available, usually sparse, observations, find the best-fitting tsunami generation and propagation model or a model set. Such best-fit model(s) could be either fully precomputed like in the Japanese operational TEWS [Kamigaichi, 2009] and in GITEWS, or constructed on-a-fly from precomputed components like in the Pacific Tsunami Early Warning System [Titov, 2009; Wei et al., 2008; Tang et al., 2009]. The derived best-fit model(s) is then believed to be an adequate representation of the actual tsunami phenomenon and could be in turn employed to provide qualified forecasting of expected tsunami arrival times and coastal runup. For detailed information on GITEWS Decision Support System and modeling unit (SIM) readers are referred to the papers of Steinmetz et al. [2010] and Behrens et al. [2010], respectively.

In this scheme, quality of the warning, thus, depends on quality of real-time data as well as quality of modeling. In GITEWS real time observations come from four main sensor types. Seismic processing of broadband station network with the original SeisComp3 software [Hanka et al., 2008] provides first information about the tsunamigenic source, namely, hypocenter and moment magnitude. Continuous near real-time GPS stations provide averaged surface displacements in two minutes intervals [Falck et al., 2010]. Together with seismic data, GPS-displacements allow for the direct inversion to get more detailed source parameters in a few minutes after the earthquake [Sobolev et al., 2006; Sobolev et al., 2007]. Later on, wave propagation is tracked by ocean-based sensors. They include deep ocean buoys which combine bottom pressure sensors [Boebel et al., 2010] with the GPS-equipped floating part [Schöne et al., 2008]. Finally, operational sensor subsystems are completed with a network of coastal tide gauges [Schöne et al., 2008] checking the incoming leading wave depression (which is a normal case for the Indian Ocean coast of Indonesia) and, thus, leaving another 5–15 min for the evacuation.

Tsunami modeling is usually separated into source modeling which provides initial conditions for tsunami and modeling of tsunami wave propagation. Within GITEWS, the operational wave propagation model TsunAWI was developed at the Alfred-Wegener-Institute (AWI), Bremerhaven [Harig et al., 2008] and also includes simulation of coastal inundation.

In the present paper we describe the source modeling approach implemented in GITEWS.

Although there are several sources of modeling uncertainty in the local tsunami early warning, the main uncertainty comes from the source. GITEWS is a near-field TEWS. Near-field TEWS have special requirements to the warning time and quality of the source characterization. Whereas a ‘classical’ far-field tsunami early warning system like the Pacific Tsunami Warning Center operates with some hours of warning time, the warning time for Indonesia is generally shorter than 10 min – taking into account some 30 min of the tsunami travel time from source to the coast minus at least 15-20 min for evacuation (see also Lauterjung et al. [2010]).

A local TEWS also has special demands to the source parameters. Reliable tsunami forecasting for the far-field can be done with primary seismic parameters including magnitude, epicenter and directivity. Other rupture parameters like focal mechanism or depth are not so important [Okal, 1988]. Slip distribution is generally not important as well – an assumption of uniform slip and epicenter in the middle of the rupture works quite well. Directivity can be with reasonable accuracy estimated from the trench geometry.

In contrast, reliable near-field prediction requires a much more detailed source model – a point source assumption is far not enough, just because source dimensions become comparable to the tsunami travel distance to the coast. This means that exact position, dimension and orientation of the source become extremely important. This is even more true if there are additional off-shore bathymetric features comparable or larger than a typical tsunami source. The Mentawai islands located some 200 km off-shore Sumatra exemplify such a pronounced bathymetric barrier which strongly affects tsunami generation and propagation in this region. See for example, Geist et al. [2006].

The above is illustrated by simple scenarios shown in Figure 8.1. The two hypothetical scenarios with homogeneous slip distribution share the same epicenter, but have opposite rupture propagation directions. In the first model (Figure 8.1a) rupture propagates northwards, similar to the December 2004 Great Andaman earthquake, while in the second model (Figure 8.1b) – in the opposite direction. All other rupture parameters are the same. These two scenarios are effectively indistinguishable according to the primary seismic information available to the warning center within the first minutes after an event, i.e., epicenter and magnitude. Nevertheless, resulting tsunami impacts at the Sumatran coast are very different for the two cases. While the north-propagating rupture poses no threat to the city of Bengkulu, the south propagating rupture would cause a major tsunami (Figure 8.1c). Such extreme difference is a typical characteristic of local, near-field tsunamis.

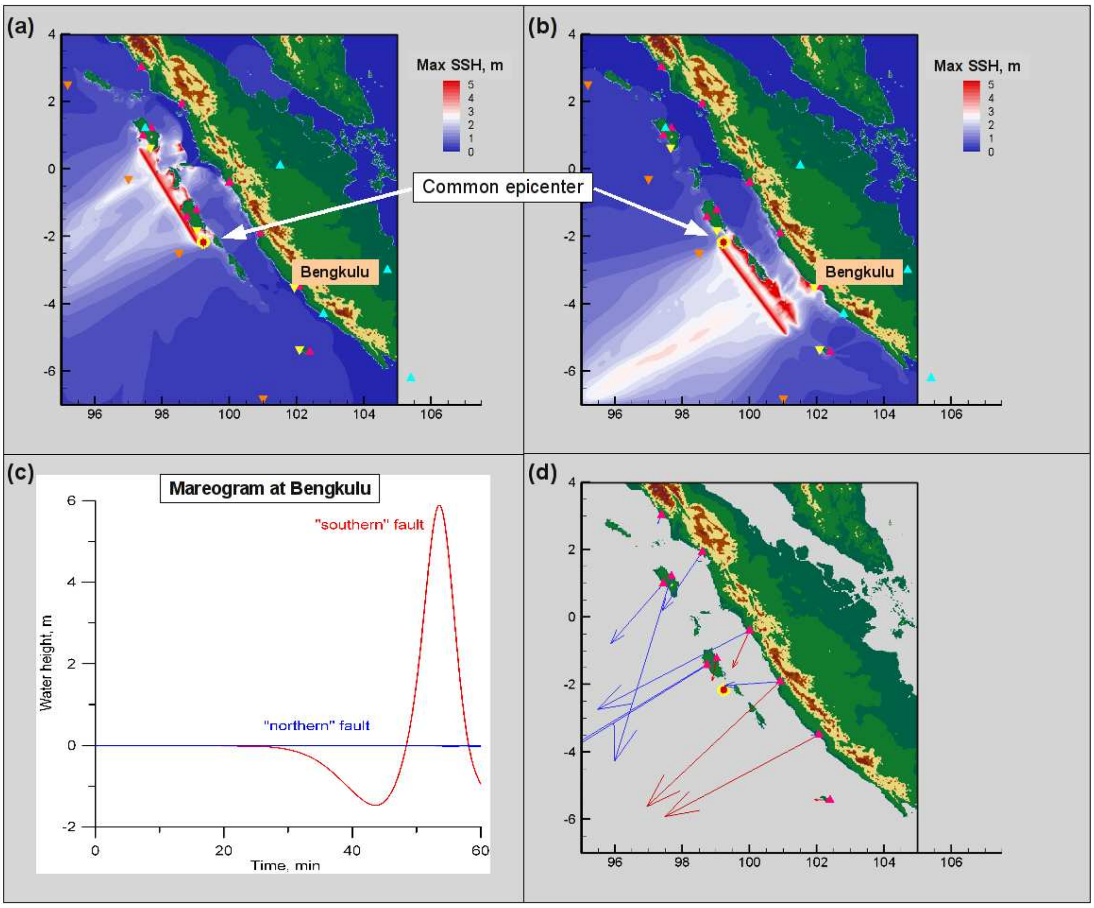

Figure 8.1 Two hypothetical scenarios offshore Sumatra demonstrating extreme sensitivity of local tsunamis to rupture position (which is not fully defined by the seismic epicenter!) and local bathymetry as well as high prediction potential of near real-time GPS observations. (a) Maximum tsunami wave heights

in case of unilateral rupture propagating northwards from the epicenter (red-yellow dot). (b) Rupture propagates in the opposite direction. (c) Resulting mareograms at Bengkulu. (d) Array of GPS stations can perfectly discriminate between the two scenarios in few minutes on an event.

The above scenarios with one-side rupture propagation do not seem unrealistic – compare them with rupture propagation of the 2004 Great Sumatra-Andaman earthquake [Lay et al., 2005; Ishii et al., 2005; Krüger and Ohrnberger, 2005a; Subarya et al., 2006].

Source models shown in Figure 8.1a, b assume simplified homogeneous slip distributions. This is usually not the case. Especially for large tsunamigenic earthquakes slip distribution is often heterogeneous with regions of largest slip, and hence, largest initial tsunami wave height, not coinciding with the epicenter. Recent tsunamigenic earthquakes at the Sunda Arc clearly illustrate this observation. E.g., the great December 2004 Sumatra-Andaman M_w=9.3 earthquake [Subarya et al., 2006], later July 2006 West Java M_w=7.8 earthquake [Fujii and Satake, 2006], September 2007 Bengkulu M_w=8.4 event [Lorito et al., 2008]. Geist and Dmowska [1999] and Geist [2002] clearly demonstrated the importance of non-homogeneous slip distribution in case of local tsunamis. Stability of the initial wave front almost directly translates all initial local wave peaks and troughs to the nearby coast.

Thus, summarizing, reliable local tsunami early warning requires much more information about the source than epicenter and magnitude. Ideally, it requires a finite fault model some 5-10 min after the event. It is still not reachable with present [Ji et al., 2002] or novel [Krüger and Ohrnberger, 2005a] seismological techniques based on teleseismic inversions. Long travel times of more than 15 min restrict their application for near-field tsunami early warning.

Alternatively, in the course of the GITEWS project, our group proposed to use near real-time GPS-arrays to get very fast information about finite fault parameters [Sobolev et al., 2006; Sobolev et al., 2007] and presented the concept of 'GPS-Shield' for Indonesia. This concept could be extended world-wide, to many other tsunamigenic active margins where the land is located above or close to seismogenic zones.

Potential usability of GPS observations for near-field tsunami early warning is illustrated in Figure 8.1d. A hypothetical coastal network of GPS stations would be able to perfectly discriminate between the two rupture scenarios. Note how prominent is the difference in fingerprints of GPS-signals issued by the 'northern' (blue) vs. 'southern' (red) rupture. Static displacements take some 2-5 min after an event to establish [Sobolev et al., 2007; Falck et al., 2010] which makes near real-time GPS a very valuable component of the tsunami early warning system. That is why the source modeling in GITEWS relies not only on seismic information but on near real-time GPS data as well.

The following section shortly presents the concept of source modeling in GITEWS. After that, in Sect. 3, we describe Rupture Generator (RuptGen) – a tool for source forward modeling, followed by some applications (Sect. 4). Finally, Sect. 5 discusses our approach to source inversion using GPS observations.

8.3 Concept of source modeling

The GITEWS approach to source modeling targets two main goals. First, it should be able to provide a reasonable source model based on very limited seismic information available just few minutes after the earthquake, namely – data on epicenter and magnitude. Second, in the case when near real-time GPS data are available, the model should be able to provide their inversion into slip distribution in order to provide a more realistic finite fault model. As noted before, GITEWS should be able to provide tsunami early warning already 5–10 min after an earthquake. To this time, only basic seismic information is available which includes position of the epicenter and magnitude [Hanka et al., 2008]. On the other hand, even simple physical rupture model, represented by the classical Okada's [1985] rectangular fault, requires knowledge of a number of parameters including rupture length and width, depth, strike-, dip and rake- angles as well as amount of co-seismic slip. Our idea is to utilize as much as possible a priori geological and geophysical information in order to pre-constrain maximum possible number of fault parameters. In particular, strike and dip angles of interplate earthquakes can be postulated from the known 3-D geometry of the plate interface. The same is true for the depth. Instead of accepting the reported hypocenter depth which can be very inaccurate, we calculate the focal depth by projecting the earthquake epicenter onto the 3-D plate interface surface.

After fixing these parameters, remaining rupture dimensions and amount of co-seismic slip can be estimated in real-time with the help of scaling laws.

In the case when near real-time GPS data are available additionally to seismic, our source model should be able to provide their effective inversion into a more reliable rupture model. Sobolev et al. [2006; 2007] demonstrated that near real-time coastal GPS arrays may be effectively employed for direct slip inversion in just a few minutes on an event. To facilitate inversion, it is better to keep it linear. Surface deformation linearly depends on the amount of slip and nonlinearly on other rupture parameters [Okada, 1985]. That means that GPS displacements could be effectively inverted into amount of slip. All other rupture parameters, whose relation to surface displacements is non-linear, should be predefined before the inversion. To meet the above requirements we discretize the 3-D subduction plate interface into numerous individual patches with dip- and strike-slip at each patch as the only free parameters, and apply the Green’s functions approach to forward and inverse calculations. Practically, for forward source modeling, this approach was realized in the so-called Rupture Generator (RuptGen) described in the next section.

8.4 Rupture Generator (RuptGen)

RuptGen is a GITEWS source modeling software tool that calculates static sea-floor and GPS displacements resulting from co-seismic slip along the subduction zone plate interface. Flexible input of rupture parameters allows various source models, from quick fully automatic ‘magnitude/location’ model to advanced user-specified slip distribution models. Program output includes gridded surface dislocations, displacement vectors at predefined positions (‘GPS-mode’) or direct output onto TsunAWI (GITEWS operational tsunami wave propagation code) non-structured grid for later tsunami propagation simulation (‘TsunAWI-mode’).

RuptGen employs the concept of patches (sub-faults) at the subduction plate interface. The plate interface between the subducting Indian-Australian and the upper Sunda plate is discretized into a regular mesh of rectangular patches (Figure 8.2) ranging from 0 to 100 km depth. The mesh follows the geometry of the plate interface as derived from the RUM model by Gudmundsson and Sambridge [1998] additionally checked against the earthquake relocation results by Engdahl et al. [2007] in the northern part. Discretization of the plate geometry is stored in a special plate interface description file. In the current version the mesh consists of 25×150 patches with dimensions of approximately 40×15 km. Each patch represents a rectangular fault plane of known geometry and position. Three components of the surface deformation (longitudinal, latitudinal and vertical displacements) due to the unit dip- and strike-slip are pre-computed for each patch and stored in a databank of patches Green's functions. Using this databank of Green's functions, sea-floor deformation can be easily calculated for any earthquake scenario with given slip distribution.

Present dislocation Green's functions are calculated using EDGRN/EDCMP software [Wang et al., 2003] for the IASP91 1D layered earth model [Kennett and Engdahl, 1991]. RuptGen is, however, absolutely flexible in choice of elastic dislocation models. Patches Green's functions can be alternatively calculated using, e.g., homogeneous half-space [Okada, 1985] or fully 3-D finite element models (not yet implemented).

RuptGen can operate in two different modes: 'automatic' and 'manual'. In the automatic mode RuptGen receives only primary seismic data (epicenter and magnitude) and automatically builds a fault model with a regular slip distribution to provide a simple but adequate solution to initiate tsunami propagation. In particular, RuptGen assumes constant rake angle for the whole rupture (90°, pure dip-slip) and employs empirical scaling laws to calculate rupture dimensions and effective co-seismic slip. Please note that 3-D geometry of the tsunamigenic plate interface and, hence, dip and strike angles as well as depth at each longitude/latitude position are predefined by the discretization model (see above).

Taking into account that rupture dimensions can be estimated from moment magnitude using empirical scaling laws, effective co-seismic slip can be estimated from the relation:

$$M_0(M_W) = (\mu)L(M_W)W(M_W)U$$

where M_0 is seismic moment and $M_W = 2/3(\log M_0 - 9.1)$, L is rupture length, W is rupture width, U is slip and (μ) is shear modulus of the ruptured media. To calculate rupture dimensions from the moment magnitude, RuptGen employs two empirical scaling laws: either relations by Wells and Coppersmith [1994] for reverse faults, or, alternatively, so called Okal's relation which postulates $L = 2W$ combined with the Wells and Coppersmith [1994] scaling law for the rupture area.

After estimating rupture dimensions and effective (average) co-seismic slip, RuptGen starts to build a finite fault model by positioning the rupture onto the plate interface discretized into patches and by applying corresponding slip shape function. Currently available slip shape functions include: (a) uniform slip, (b) Gaussian symmetrical in both directions and (3) asymmetrical crack model with a smooth closure condition along width [Freund and Barnett, 1976; Geist and Dmowska, 1999] combined with variable linear tapering along length.

Result of these manipulations is a list of ruptured patches with amount of slip at each patch. After that, Green's dislocation functions for each patch are linearly combined to give the resulting three component surface deformation (Figure 8.2).

In the second, manual mode, user can directly specify any slip distribution to simulate complex heterogeneous finite fault models. For example, teleseismic inversions of large tsunamigenic earthquakes can be interpolated into RuptGen to simulate historical events.

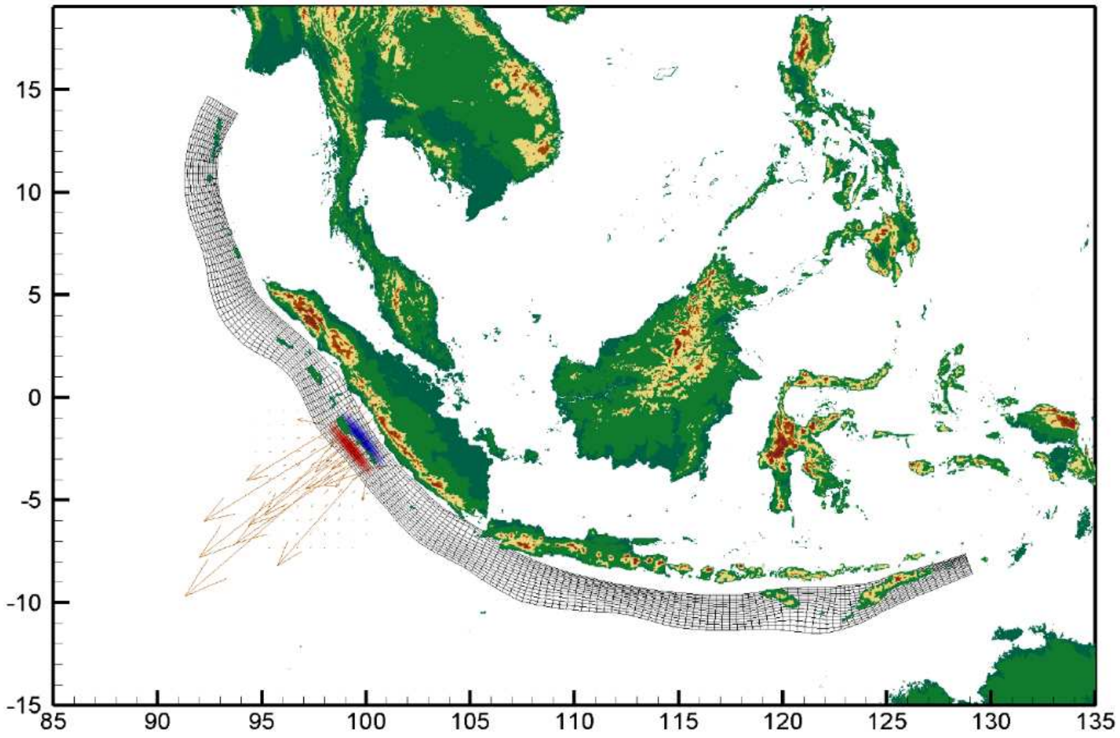

Figure 8.2 Discretization model for the tsunamigenic Sunda plate interface (150×25 patches) based on Gudmundsson and Sambridge [1998]. Also shown are initial wave and horizontal surface displacements for an M_w=8.4 scenario from the GITEWS scenario databank.

8.5 Implication of RuptGen for scenario generation

8.5.1 Providing sources for the GITEWS tsunami repository

GITEWS operational forecasting is based on the databank of pre-computed tsunami scenarios. Four different sensor systems – seismic, GPS, deep ocean buoys which combine a GPS buoy with a bottom pressure unit (OBU), and, finally, coastal tide gauges – deliver real-time observations to the Tsunami Service Bus (TSB) [Fleischer et al., 2010]. After initial proof and pre-processing of sensor data, TSB delivers them to the Decision Support System (DSS) [Steinmetz et al., 2010], which, in turn, asks the Simulation Module (SIM) [Behrens et al., 2010] to match observations to pre-computed tsunami scenarios. Scenarios, which best fit the data, are considered to represent the current situation off-shore and are used for the forecasting. It is worth to note that the DSS does not take a single 'best-fit' scenario but takes care of all possible data uncertainties and databank assumptions and builds an aggregated best-match scenario from a list of top-matches.

Presently, the databank includes about 2000 scenarios along the Sunda subduction zone plate interface with epicenters lying in centers of RuptGen patches (Figure 8.2), i.e., some 30 km apart and magnitudes ranging from 7.5 to 9.0. Despite RuptGen can model any slip distribution, there are no reasons to assume some complex non-symmetric slip distribution for regular databank scenarios. Standard scenario in the tsunami repository assumes a rupture model with following characteristics:

- width and length follow the scaling laws by Wells and Coppersmith [1994],
- epicenter coincides with the geometrical center of the rupture,
- slip distribution has a symmetrical bell-shaped (Gaussian) form with maximum at the epicenter,
- effective slip is calculated from the above equation assuming shear modulus $\mu=3.5\times10^{10}$ Pa.

Example scenario surface displacements corresponding to an $M_w=8.4$ earthquake are shown in Figure 8.2.

Additionally to wave propagation, GITEWS simulation databank contains also vertical and horizontal co-seismic static surface displacements for the later matching with real-time GPS observations.

8.5.2 Source models for historical events

Historical events are valuable natural benchmarks for testing of new models and algorithms. To calculate databank scenarios, we employed RuptGen in the automatic mode. In contrast, historical events with their known slip distribution should be usually modeled in the manual mode. In the following two models, slip distribution implied on input to RuptGen comes from inversion of co-seismic GPS observations (see more about inversion in Sect. 5).

Figure 8.3 presents slip reconstruction for the two historical events off Sumatra: the great December 2004 $M_w=9.1$ Sumatra-Andaman earthquake (Figure 8.3a) and following Nias event of March 2005 with $M_w=8.6$ (Figure 8.3b).

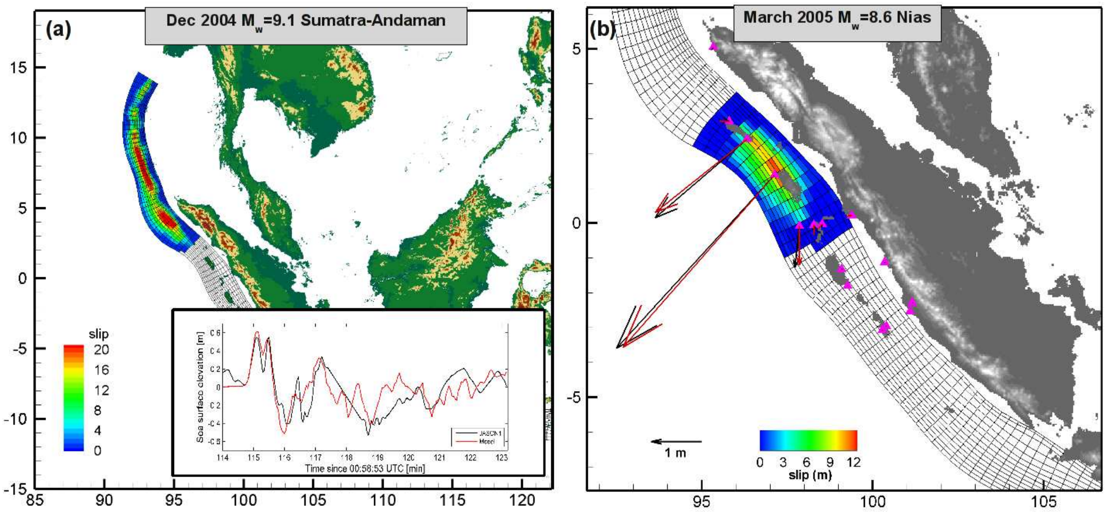

Figure 8.3 Source models for the two historical events off Sumatra. Slip distribution was inverted from GPS observations. (a) Model for the great Sumatra-Andaman M_w=9.3 earthquake [Hoechner et al., 2008]. Inlet shows comparison of the corresponding tsunami propagation model with the direct tsunami observation in Indian Ocean some 2 h. after the earthquake by the Jason-1 satellite mission. (b) 2005 Nias-Simeulue M_w=8.6 event.

Slip distribution for the December 2004 event comes from the GPS inversion by Hoechner et al. [2008]. See this paper for more details on inversion procedure and sources of data. An independent check for the quality of resulting source model is provided by the comparison of the computed tsunami wave propagation with the direct satellite observations by the Jason-1 mission (see inlet on Figure 8.3a).

Slip distribution for the Nias March 2005 earthquake is less heterogeneous (Figure 8.3b) showing the two regions of larger slip under the islands. Note very good correspondence between calculated and observed GPS-displacements [Konca et al., 2007].

Recent 30 September 2009 Padang M_w=7.5 earthquake took place when GITEWS Decision Support System was already running in Jakarta in test mode. We had a possibility to check our forecasting and warning procedures. It was even more intriguing since this earthquake was not a classical subduction zone event, which was expected to take place in the region of Padang after the Nias 2005 and Bengkulu 2007 events. Expected was a shallow-dipping thrust interplate event with strike parallel to the trench. Exactly such kind of events are pre-computed and stored in the GITEWS scenario database (Sect. 4.1). In reality, the earthquake of 30 September did not rupture the plate interface, instead, it was an intraplate event inside the subducting slab with much steeper dip angle (>50°) and strike angle almost perpendicular to the trench [USGS, 2009]. Events with such focal mechanisms are extremely rare in this region, which brought additional challenge to the GITEWS Decision Support System (DSS).

The Earthquake took place at 10:16:09 UTC. Five minutes after that, at 10:21:00 UTC, DSS had only primary seismic data for matching: position of the epicenter and magnitude value of 8.0. Simulation module (SIM) matched these data to the pre-computed scenario which forecasted about 2-3 m tsunami wave in the city of Padang. Actually, such forecast would lead to a false warning, since in reality observed wave height in Padang did not exceed 40 cm. The discrepancy is attributed to the difference between real rupture parameters, from one side, and that known to the DSS (magnitude estimate) and assumed by source modeling (focal mechanism, depth, geometry), from another side. We performed analysis of which parameters are responsible for the potential false alarm.

1. Focal mechanism. As noted above, the focal mechanism of the Padang earthquake was very unusual, with almost 90° rotated strike and much steeper dip compared to the 'classical' subduction zone earthquake comprising the scenario databank. Our hindcast modeling showed that focal mechanism did not play any significant role in this case. 'Classical' subduction zone effect of the same magnitude at the same position would give approximately the same minor runup in Padang.

2. Hypocenter depth. Finally reported CMT depth is about 80 km (intra-slab event) in contrast to the 60 km scenario hypocenter depth. Again, hindcast modeling showed that the 20 km depth difference could not account for somewhat significant runup difference.

3. Magnitude value. CMT value derived some hours after the event is M_w=7.5. At 10:21:00 UTC DSS operated with a SeisComP3 value of M_w=8.0 (later on this value was reduced to 7.7). And that was exactly the reason for the overestimation of the tsunami threat. Scenario models with M_w=7.5 magnitude predict no tsunami threat even if assuming 'classical' focal mechanism and/or shallower depth of 60 km.

In the introduction we noted that near real-time GPS data may be a very valuable addition to the seismic information in order to better constrain source parameters in a few minutes after an event. The earthquake on 30 September proved that once again. The Indonesian GPS-station in Padang operated by the National Coordination Agency for Surveys and Mapping (BAKOSURTANAL) did not show any notable coseismic displacement (C. Falck, personal communication). In contrast, the M_w=8.0 scenario, selected by matching to seismic data only, would have implied about 50 cm of horizontal displacement. Had GPS data been available to the Decision Support System 5 min after the earthquake, the above scenario, which overestimated tsunami hazard, could have been rejected by the matching procedure.

8.5.3 Modeling of hypothetical future events for testing and training

Together with historical events, fully synthetic hypothetical scenarios provide a valuable basis for tuning and testing of the GITEWS components as well as for teaching and training of the future warning center personnel. Moreover, historical records, while being of highest priority, nevertheless, cannot provide all necessary data for the extensive system verification and validation. Data are sparse and irregular, some sensor types like deep ocean buoys were not available in the Indonesian region until recently. Continuous near real-time GPS were not employed for the early warning elsewhere. Due to the same reasons, historical events are not the best scenarios for teaching and training of the warning center personnel. In this respect, synthetic scenarios, which provide all possible coherent sensor data to the same event, appear to be the best candidates for testing and training.

In GITEWS we developed a so-called Scenario Library consisting of a number of fully synthetic scenarios containing modeled sensor signals stored in natural sensor formats. Scenarios from this library can be any time played back on input to the GITEWS software units (Figure 8.4). The latter does not actually realize if incoming data come from real or from virtual world.

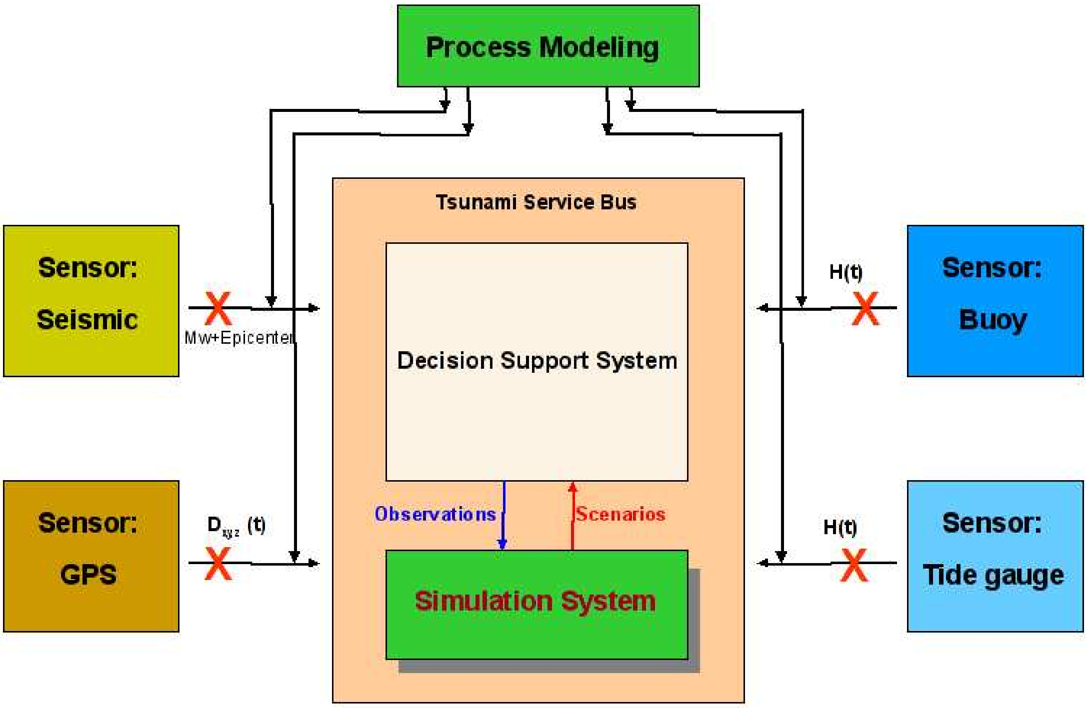

Figure 8.4 Implication of the process modeling for the testing of the GITEWS core software components: Tsunami Service Bus (see also Fleischer et al. [2010]), Decision Support System [Steinmetz et al., 2010] and Simulation Module. The system is being detached from real physical sensors and being feeded by precomputed scenario datasets at different sensor types.

Synthetic scenarios are fully under control of their developers. That makes them an ideal toolkit to simulate all possible situations which may realize in later operational work.

8.6 Towards more reliable source inversion with near real-time GPS data

As noted before, one of the goals of the source modeling unit of GITEWS is fast inversion of near real-time GPS data. Incorporation of GPS data in addition to seismic information can strongly increase the quality of the tsunami forecasting in the near-field [Sobolev et al., 2006; 2007] providing more information on source parameters in a few minutes on an event (see also Sect. 1).

Real-time GPS data were not previously employed in the tsunami early warning. Rapid progress of the GPS processing technique during the last decade makes near real-time GPS observations a valuable component of future tsunami warning systems. Blewitt et al. [2006] showed that even far-field GPS data can be used to correctly determine the magnitude and some information about the geometric pattern for a large earthquake in nearly real time. Simultaneously, Sobolev et al. [2007] studied the possibility of near real-time magnitude determination and slip inversion based on near- and middle-range GPS observations during the great Sumatra-Andaman earthquake. The two historical rupture models presented in Figure 8.3 are results of direct inversions of GPS observations into slip distribution.

GPS inversion into slip distribution, while exploiting the linearity of surface deformation relatively to the amount of slip, still remains a numerically challenging task [Hoechner et al., 2008]. An alternative way is the inversion with the help of pre-computed source models (database matching), such as scenarios from the GITEWS database. In the present section we want to assess the feasibility and possible benefit from performing a direct slip inversion as compared to selecting a pre-computed scenario for tsunami early warning.

To this purpose we consider an extreme earthquake in terms of slip distribution, with slip concentrating at the starting and the ending side of the rupture (approximately offshore Padang and Bengkulu). This scenario with heterogeneous slip and M_w=8.62 (forward model) is shown in the leftmost column of Figure 8.5. Azimuth of slip vectors is 210°.

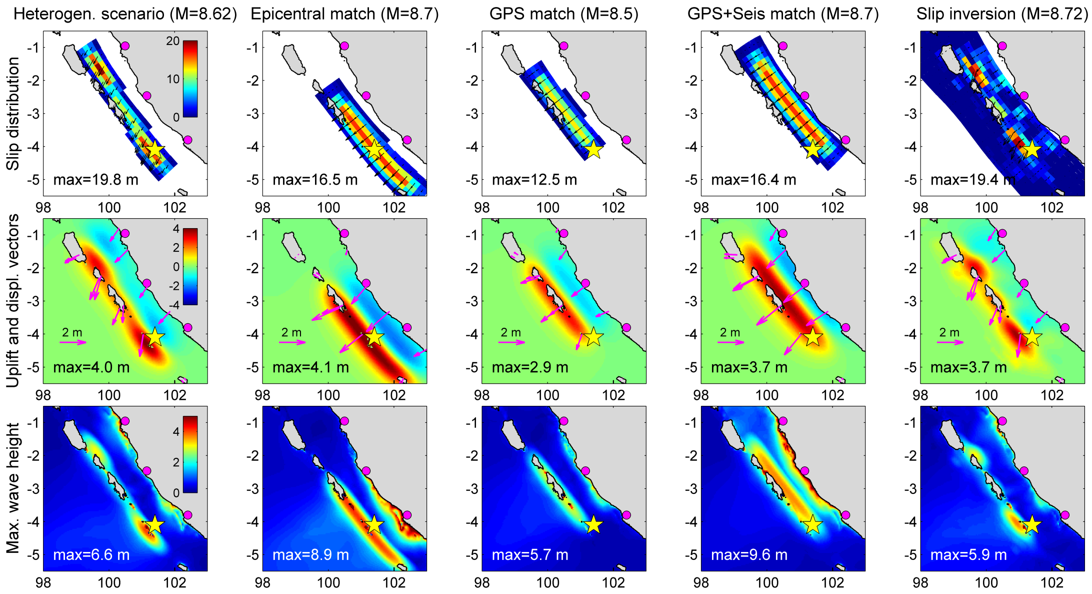

Figure 8.5 Comparing different methods of source inversion for a synthetic scenario with strongly heterogeneous slip distribution. Rows: First: slip distribution (color) and rake angle (arrows), epicenter (yellow star) and tide gauge positions (magenta circles, from north: Padang, Muko Muko, Bengkulu). Second: sea floor deformation and horizontal GPS displacement vectors. Third: maximum wave height. Columns: First: synthetic scenario with heterogeneous slip distribution (forward model). Second: scenario match from a pre-computed databank based on seismic data only (epicenter and magnitude). Third: best matching scenario using GPS. Fourth: best match using GPS plus seismic magnitude. Fifth: direct inversion of GPS into slip distribution.

We then generate a dataset of synthetic ruptures in magnitude steps of 0.2 and epicenters spaced every 25 km perpendicular and 80 km parallel to the trench. All ruptures have rake angles equal to 90° (pure dip-slip). Further on, we will compare our forward model to different matching schemes.

The second column in Figure 8.5 shows the scenario selected from the dataset using seismic parameters as matching criteria only: epicenter (yellow star) and magnitude. The next column presents matching based on GPS data. ‘GPS observations’ were generated from the forward model by applying random noise of 5 cm horizontal and 10 cm vertical amplitude. Spatial distribution of GPS stations corresponds to the ideal ‘GPS shield’ configuration as described in Sobolev et al. [2007]. The fourth column corresponds to the joint matching of GPS and seismic data.

Inversions presented in columns 2 to 4 were made by matching ‘observations’ with pre-computed scenarios from the dataset. In contrast, the last column in Figure 8.5 presents results of direct inversion of ‘GPS-observations’ into the slip distribution at the patches. The direct inversion procedure minimizes GPS misfit between forward model and inversion using smoothing and boundary constraints for slip and rake angle as described by Hoechner et al. [2008].

Since all the source models are, in end-effect, interesting relative to their tsunamigenic potential, we calculated corresponding tsunamis at the Sumatran coast. Figure 8.6 shows synthetic tide gauge time series at three selected sites. It is clear that the seismic match (second column on Figure 8.5) is not a good choice for such a unilateral rupture, – predicted maximum wave height at Bengkulu is about 2 times too high while prediction for Padang is about 6 times too low and 40 min too late. The two GPS-matches capture well the extent of the rupture. The GPS-only match significantly underpredicts wave heights, while joint GPS + seismic inversion results in quite good predictions for Padang and Bengkulu. At the same time, prediction at Muko Muko is about twice as high, since there are no earthquakes with heterogeneous slip distribution in the scenario dataset.

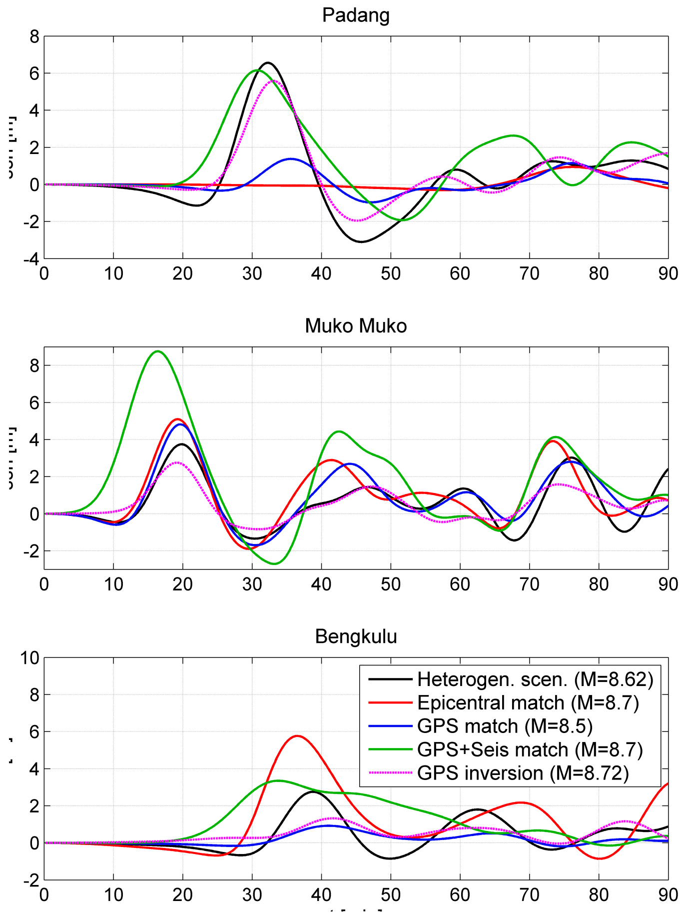

Figure 8.6 Mareograms at the three tide gauges (for location see Figure 8.5) for the different inversion methods.

Direct slip inversion was able to reconstruct the two separated slip maxima (Figure 8.5, rightmost column), and the general agreement at the tide gauges is good, though there is significant underprediction at Bengkulu (Figure 8.6). The reason therefore is that the southern patch of larger slip in the inverted model (rightmost column on Figure 8.5) is shifted some 50 km north relative to the forward model (leftmost column on Figure 8.5). Due to the extreme sensitivity to location (effect of the Mentawai islands), this shift is enough to get markedly smaller runup in Bengkulu. This observation illustrates, first of all, again that the near-field early warning crucially depends on source parameters [Geist, 2002], and, hence, on quality of source inversion.

Present modeling shows that direct inversion of GPS observations into slip distribution requires further studies and optimizations. Numerical analyses constrained by (rare) real observations seem to be an appropriate strategy for such studies. Direct slip inversion has many advantages coming, first of all, from its flexibility and absence of any pre-constrained slip distributions. On the other hand, direct inversion can be tricky and needs extensive calibration for each particular GPS-constellation, and, hence, costs time and expertise. To provide reliable source inversion, one needs very good station coverage. For example, an additional GPS-station south of Bengkulu might have helped to better resolve the southern end of the rupture.

Matching into pre-computed scenarios seems to be a reasonable alternative, especially when station coverage is far from ideal. The main advantage here is that such an inversion is numerically stable even with only a small number of observations and will always result in a physically credible source model, because we do not invert into slip on individual patches, but use already physically reasonable scenarios from the databank. The main disadvantage is that scenarios in the databank have some pre-defined slip distribution, so we would not be able to get real slip distribution. Actually, what we invert for is the position of the earthquake centroid and magnitude. Of course, matching with a single scenario could not be optimal for ruptures with strongly heterogeneous slip distribution, like in the example above. A perspective way to deal with such complex ruptures may be matching with linear combination of two or more databank scenarios simultaneously. That is, after matching to a single scenario, one may try to further reduce the GPS-mismatch by combining any two closely located scenarios with variable weights.

A very important issue is a forecast uncertainty which is generally a complex product of model and observation uncertainties. Model uncertainties include, e.g., megathrust geometry, limitations of dislocation model employed, material parameters. Figure 8.3 demonstrates that our source model is able to reproduce real observations for large events pretty well. We need, however, much more case studies, especially for smaller events, with lower signal-to-noise ratio.

If pre-computed scenarios are used for the source inversion, then other important model uncertainties come from the discreteness of the data-bank population and from imposed models of slip distribution. Figure 8.5 illustrates the effect of discreteness: compare, for example, the two pre-computing scenarios, columns 3 and 4, which are close to each other by location (~50 km) and magnitude (0.2 M_w) but predict significantly different wave heights (see also Figure 8.6, blue and green lines). Sensitivity analysis is required in each particular case to derive the necessary population density for the databank of pre-computed scenarios.

As to the observation uncertainty, one should recall at least the uncertainty in M_w. In the GITEWS Project, with its dense broadband station distribution, this uncertainty is estimated to be ±0.3 magnitude units during the first 5 to 10 min after an earthquake. In the early warning process, this uncertainty would be usually treated in a worst-case sense thus leading to the significant over-estimation of the source (compare to the previous paragraph), if not additionally constrained by other observations like near real-time GPS (see Behrens et al. [2010] for more information about multi-sensor inversion approach in GITEWS). Detailed analysis on the quality of forecast with near-real time GPS lies out of the scope of the present paper and will be addressed elsewhere.

8.7 Summary and outlook

In the present paper we presented the GITEWS approach to the source modeling for the tsunami early warning in Indonesia. Near-field tsunami poses strict requirements to both warning time and details of source characterization. To meet these requirements we try to employ as much geophysical and geological information as possible in order to pre-define maximum number of rupture parameters. We discretize the tsunamigenic Sunda plate interface into an ordered grid of patches and employ the concept of Green's functions for forward and inverse rupture modeling. Amount of dip- and strike- slip at the patches are the only free parameters in our source models.

Our forward modeling tool, Rupture Generator, additionally employs different scaling laws and slip shape functions to construct physically reasonable source models from basic seismic information only, namely, from magnitude and epicenter location.

GITEWS runs a library of semi- and fully synthetic scenarios to be extensively employed by system testing as well as by teaching and training activities in the warning center. Synthetic scenarios are probably the only way to get a physically coherent image of an event (earthquake plus tsunami) at different sensor types including land- (seismic, GPS) and ocean-based sensors (bottom pressure units, floating GPS buoys, coastal tide gauges).

Near real-time GPS observations are a very valuable complement to the local tsunami warning system. Their inversion provides quick (within a few minutes on an event) estimation of the earthquake magnitude, centroid location and, given sufficient station coverage, details of slip distribution. GPS data can be inverted either into pre-computed source models, or directly into slip distribution at the patches. The latter approach provides more reliable source models, especially for large events with heterogeneous slip distribution, but requires very good station coverage. Both inversion approaches require further efforts in development of methodology and fast numerical solutions as well as extensive testing and calibration at particular locations. Numerical rupture models, as developed in the present study, seem to provide an appropriate background for such studies.

8.8 Acknowledgments

The GITEWS project (German Indonesian Tsunami Early Warning System) is carried out through a large group of scientists and engineers from (GFZ) German Research Centre for Geosciences and its partners from the German Aerospace Centre (DLR), the Alfred Wegener Institute for Polar and Marine Research (AWI), the GKSS Research Centre, the German Marine Research Consortium (KDM), the Leibniz Institute for Marine Sciences (IFM-GEOMAR), the United Nations University (UNU), the Federal Institute for Geosciences and Natural Resources (BGR), the German Agency for Technical Cooperation (GTZ), as well as from Indonesian and other international partners. Funding is provided by the German Federal Ministry for Education and Research (BMBF), Grant 03TSU01. Authors thank Gerd Teschke (University of Applied Sciences, Neubrandenburg) for his valuable help in establishing GPS inversion algorithms. Johannes Franke (IABG, Müunchen) and Jens Fleischer (GFZ, Potsdam) assisted in development of the GITEWS Scenario Library. Comments and suggestions of S. Lorito, an anonymous reviewer and the editor of the Special Volume helped to improve the manuscript. This is GITEWS publication No. 113.

9 Conclusions and Outlook

This thesis focuses on two main subjects. One is tsunami early warning within the framework of the GITEWS project, the other is interpretation of observations influenced by the Sumatra-Andaman 2004 earthquake. Main thread going through all of my work is the involvement of GPS data.

9.1 Tsunami early warning

Primary task was the development of a database containing realistic earthquake scenarios for the Sunda Arc as tsunami sources and associated sensor responses. We decided to use a Green's functions approach, that is, to discretize the subduction interface and compute deformation as linear combination of the subfault contributions applying some scaling relations. The advantage of this approach is that earthquake models can be computed easily with only little information available, e.g. location and magnitude. Disadvantage is that intraplate or strike-slip earthquakes will be misinterpreted as happening at the subduction interface. But since these events are not tsunamigenic, an extension of the database is not planned.

The geometry is based on RUM slab geometry by Gudmundsson and Sambridge [1998], and we showed it to be in good agreement with newer seismic relocations by Engdahl et al. [2007] in the region of the Sumatra-Andaman 2004 earthquake. A similar comparison for the Sunda Arc south thereof would be desirable.

Most studies dealing with tsunami early warning use the analytical expression for a homogeneous halfspace by Okada [1985] to compute elastic deformation. We used a semi-analytical layered half-space approach [Wang et al., 2006] wich captures the largest corrections and is still computationally inexpensive

The simulation system in the tsunami early warning center uses a database of pre-calculated earthquake- and tsunami-scenarios, since the tsunami models have high resolution at the coast and thus are time-consuming. Recent advances in computing (e.g. adaptive meshes, GPU computing) make tsunami modeling in real-time possible. This offers the possibility to use seismic or GPS-based real-time source inversions as tsunami initial condition, resulting in better run-up estimates. Another advantage would be, that the maintenance of the database required when modifications or extension are implemented - which is quite a big job (it takes several months to compute all scenarios) - could be omitted.

The second big project related task involved the 'GPS shield concept', where we demonstrated the value of GPS for tsunami early warning. An other kind of sensitivity analysis is given in Figure 9.1, where the minimum resolvable earthquake magnitude for a certain constellation of GPS receivers is shown. The triangles represent existing GPS stations of the Sumatran GPS array [SuGAr] by Caltech and are used for tectonic analyses [Chlieh et al., 2008]. Unfortunately they are not equipped with real-time transmission and processing equipment and thus cannot be used for tsunami early warning. Efforts to upgrade these stations to real-time capability in the framework of the GITEWS project were not successful, but some of the numerous real-time seismic stations and tide gauges installed during the project are now being equipped with GPS

[Falck et al., 2010]. Together with the buoys, which are able to provide real-time vertical displacement information, they will form some basic version of the ‘GPS-shield concept’. We are involved in a similar resolution analysis as shown in Figure 9.1 for the eastern part of the Aleutian arc.

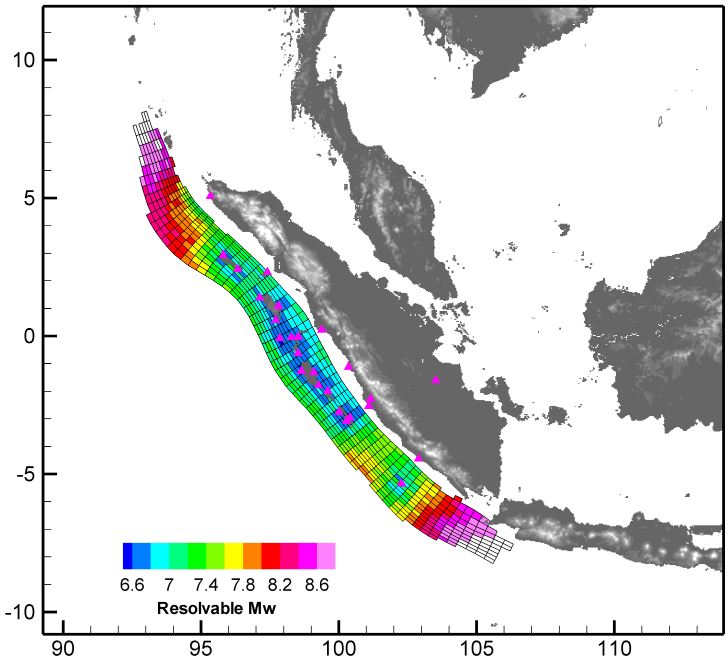

Figure 9.1 Sensitivity analysis for the Sumatran GPS array [SuGAr] assuming ±0.5 cm horizontal and ±1.5 cm vertical accuracy of GPS data. Colors show the minimum resolvable magnitude, triangles represent the receivers.

9.2 Geophysical interpretation of GPS observations

Through the interpretation of GPS data it is possible to shed light on processes acting on very different time scales. Final static displacements are easily extracted from coseismic time series and allow reconstruction of the slip distribution. For larger events and good signal to noise ratio, it is possible to obtain rupturing properties similar to seismic methods. Postseismic data allow to infer afterslip and to draw conclusions on rheological properties of the upper mantle. Interseismic time series reveal locking conditions at the subduction interface. And of course, the relative motion of tectonic plates and intraplate deformation is superposed to above processes. However, separation of the effects of above processes is a non-trivial task. Longer observation times from denser networks, combined with other types of observations as well as advances in theoretical models are required in order to get more stringent conclusions.

During my PhD position I dealt with all of the above processes, however not all activities led to publications. A very fruitful application of geodetic methods for scientific as well as earthquake and tsunami early warning issues is the analysis of interseismic strain buildup. It allows detection of locked patches at the subduction interface, and together with the earthquake history to identify regions at high risk. More generally, it improves the understanding of the seismic cycle and the subduction process. During my PhD studies I performed inversions for interseismic locking offshore Sumatra, but it turned out that there was not much to add to the very thorough work by Chlieh et al. [2008], unless new data becomes available, so that activity was suspended.

I used a layered half-space approach throughout my modeling. But unlike in the case of tsunami early warning, there would be some benefit from using spherical models or fully three-dimensional finite element models for seismic and tectonic applications. It was actually planned at the beginning of my PhD work to switch to finite element modeling at some point, but priorities shifted during the project, and focus was more on inversion procedures and a broader range of observations. Meanwhile, other groups published GPS inversions for the Sumatra 2004 earthquake based on finite element modeling: [Masterlark and Hughes, 2008; Moreno et al., 2009], former using ‘ABAQUS’, latter using ‘ANSYS’, both commercial software packages.

Biviscous Burgers rheology of the asthenosphere is a possibility to reconcile postseismic observations and modeling. It enables to resolve contradictions between GPS and geoid data. The generalized Maxwell model, representing several or even a continuum of relaxation times would be an appealing further enhancement from a theoretical point of view, and also interesting in terms of rock physics (e.g. relating different grain sizes).

The quasi-static assumption for deformation propagation proposed in chapter 6 represents a ‘bottom-up’ approach: additionally to slip distribution obtained from the final static displacement, it allows in a simple way to obtain rupturing properties. It works for large or slow events (aseismic slip) and near-field receivers. The recent emergence of high-rate GPS will undoubtedly lead to interesting applications of seismological methods to the analysis of GPS data, as for example in [Delouis et al., 2010].

Especially attractive for a geodynamic modeling group would be to use one code to cover a whole spectrum of processes: from dynamic rupturing to the seismic cycle, including loading and relaxation, coupled to global geodynamic evolution, all with nonlinear rheologies. In our group, some experiments with self-made elasto-visco-plastic codes normally used for geologic time scale modeling have been carried out to implement seismic waves. But to reach above goal, advances in many respects are required and a lot of theses have still to be written!

10 Appendix: Public outreach

This appendix contains non-scientific materials in whose preparation I was involved in.

10.1 Brochure: ‘Tsunami Warning: How much mathematics is in the wave?’

The following text is from a brochure which was made on occasion of the ‘Year of Mathematics’ in Germany in 2008. Part of the exhibition on ‘MS Wissenschaft’, which toured along the major rivers of the country, was about the mathematics of tsunami. It introduced the concept of the simulation system for GITEWS and featured several exhibits.

Tsunami-Warnung: Wie viel Mathematik steckt in der Welle?

Der Tsunami vom 26. Dezember 2004 riss fast eine Viertelmillion Menschen in den Tod. Noch Stunden nach dem verheerenden Erdbeben, das die Katastrophe verursachte, starben an den Ufern des Indischen Ozeans viele Menschen, weil sie nicht gewarnt werden konnten. Die Bundesregierung beschloss daher, im Rahmen der deutschen Flutopferhilfe den Aufbau eines Tsunami-Frühwarnsystems für den Indischen Ozean und erteilte der Helmholtz-Gemeinschaft unter Federführung des Deutschen GeoForschungsZentrums (GFZ) dazu den Auftrag. Zusammen mit der am stärksten betroffenen Nation Indonesien entwickelt ein Konsortium deutscher Geo- und Meeresforscher das GITEWS (German Indonesian Tsunami Early Warning System), das Ende 2008 den operationellen Betrieb aufnehmen wird und 2010 vollständig aufgebaut in indonesische Hände übergeben wird.

Was ist GITEWS?

GITEWS ist ein Warnsystem, das aus verschiedenen, voneinander unabhängigen Sensorsystemen besteht, deren Daten in einem nationalen Warnzentrum in Jakarta zusammenlaufen und dort ausgewertet werden. Da über 90% aller Tsunamis von Seebeben ausgelöst werden, ist die schnelle Erfassung und Auswertung von Erdbeben das Kernstück für den Tsunami-Alarm. Aber auch die wesentlich selteneren Auslöser wie Hangrutschungen und Vulkanausbrüche müssen erfasst werden. Erzeugt ein solches Ereignis einen Tsunami, muss dieser gemessen, gemeldet und bewertet werden. Dazu dienen verschiedene Sensoren unter Wasser, an Land, auf Bojen und satellitengestützte Messungen. Bei den gewaltigen Datenmengen, die hier anfallen, ist die computergestützte (numerische) Mathematik ein unerlässliches Hilfsmittel.

Wie misst man den Tsunami?

Vor Indonesien treffen zwei große Kontinentalplatten aufeinander, wobei sich die Indisch-Australische Platte mit einer Geschwindigkeit von 6 cm pro Jahr unter die Eurasische Platte schiebt. Diese Kollisionszone, die weitgehend parallel zur Küste Indonesiens verläuft, wird Sundabogen genannt. Bei diesem Subduktionsprozess kommt es immer wieder zu heftigen Erdbeben. Wissenschaftler des GFZ haben dort mittlerweile 12 moderne seismische Stationen installiert und diese über Satellitenkommunikation mit etwa 100 internationalen Erdbebenstationen in der Region des Indischen Ozeans zu einem leistungsfähigen Messnetz verbunden. Die Positionierung der Seismometer und der Aufbau des Netzwerks folgen der Forderung, dass ein Erdbeben, egal an welcher Stelle des Gebiets es auftritt, innerhalb von 2 Minuten an mindestens drei Stationen des Netzes registriert wird und somit eine erste Lokalisierung sehr schnell erfolgen kann Die Lokalisierung und Magnitudenbestimmung wird dann im Laufe der folgenden Minuten durch die Einbeziehung weiterer Stationen immer sicherer und genauer. Bereits heute ist das System in der Lage, auch starke Erdbeben dort innerhalb von vier Minuten zu erfassen und zu bestimmen - eine enorme Leistung, die auf der von Seismologen und Informatikern des GFZ Potsdam entwickelten Software SeisComP3 beruht. Darüber hinaus ermöglichen Stationen an Land mit dem Satellitennavigationssystem GPS die Bestimmung des Bodenversatzes, der durch das Erdbeben hervorgerufen wird. Da aber nicht jedes Seebeben einen Tsunami erzeugt, muss dieser im Ozean gemessen und verifiziert werden. Dazu dienen einerseits Drucksensoren, die entlang des Sundabogens vor der Küste Indonesiens auf dem Meeresboden ausgebracht werden. Wandert der Tsunami über den Sensor, so ändert sich der Wasserdruck durch die Meeresspiegeländerung. Diese Veränderung wird am Meeresboden erfasst und mit Hilfe eines Unterwassermodems zu einer Boje übertragen, von wo die Daten dann per Satellit an das Warnzentrum gesendet werden. Der Tsunami kann andererseits noch mit GPS-Geräten registriert werden, die auf diesen Bojen installiert sind, oder aber entlang der Küste bzw. auf den vorgelagerten Inseln mit Pegelstationen. Um sowohl bei den Bojen, den Unterwassereinheiten und den Küstenpegeln die durch Wind und Gezeiten erzeugten Meeresspiegeländerungen von einem Tsunami zu unterscheiden, setzt man leistungsfähige mathematische Filter ein, so dass die Tsunamiwelle mit mehreren unabhängigen Verfahren zuverlässig erkannt werden kann.

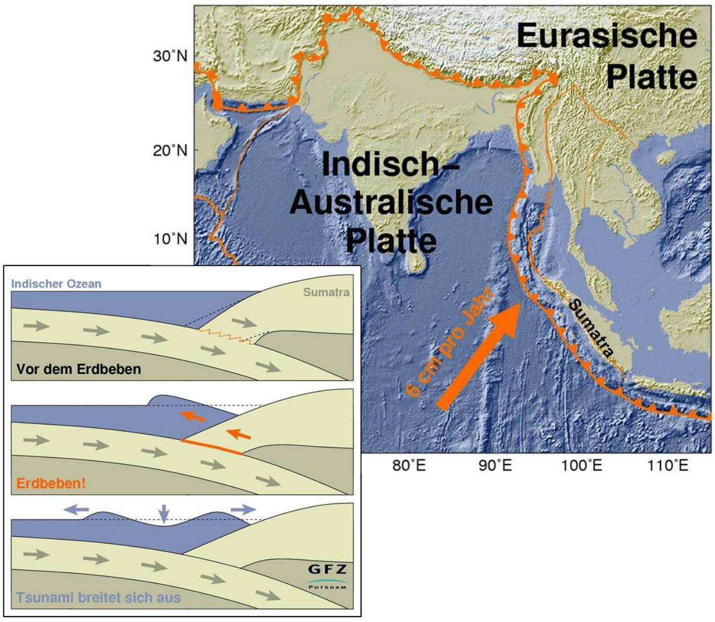

Plattentektonische Situation vor der Küste Indonesiens (Sumatra) und schematische Darstellung der Tsunami-Entstehung durch ein starkes Erdbeben.

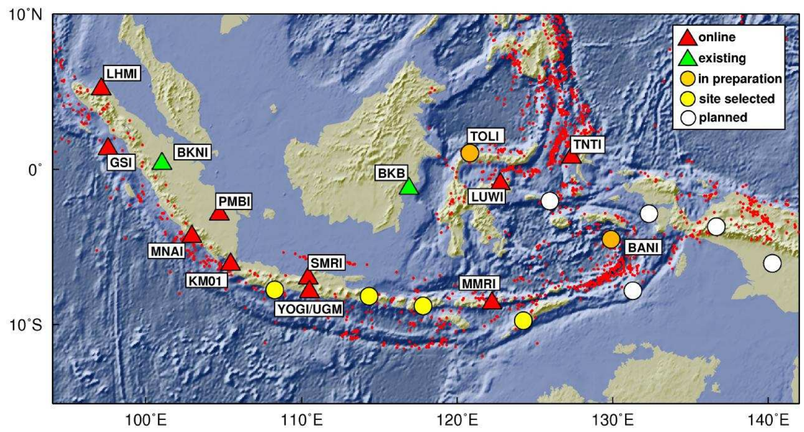

Aufgebaute und geplante deutsche seismologische Stationen in Indonesien. Die schnelle Erfassung und Auswertung des Erdbebens ist eine wesentliche Komponente des Tsunami-Frühwarnsystems

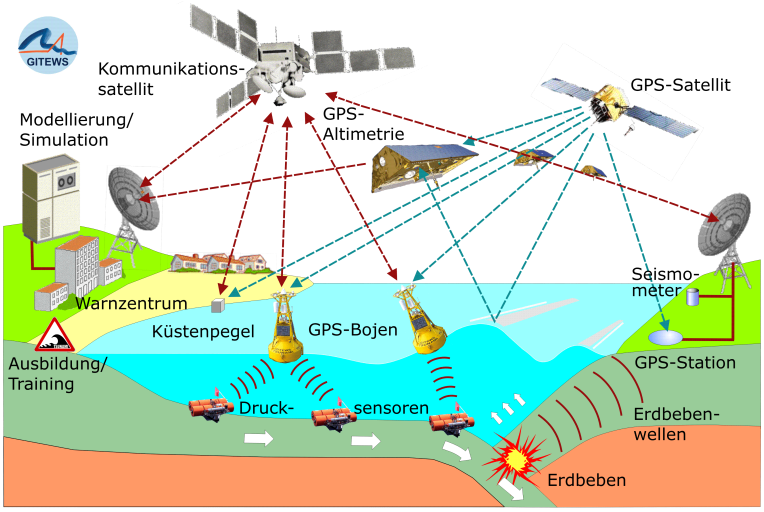

Das Tsunami-Frühwarnsystem besteht aus verschiedenen Sensoren wie Seismometer, Meteo-, Druck- und GPS-Sensoren der Boje, Pegeln und GPS-Sensoren, deren Daten in einem nationalen Warnzentrum zusammenlaufen und ausgewertet werden.

Modellierung eines Tsunami

Alle erfassten Informationen treffen in Echtzeit im Daten- und Warnzentrum ein. Um die vielen Einzelmessungen der unterschiedlichen Instrumentensysteme zu einem schnell interpretierbaren Gesamtbild mit den wichtigen Informationen, z.B. Ankunftszeit des Tsunami an verschiedenen Küstenabschnitten oder erwartete Wellenhöhe, zusammenzufassen, hilft uns die numerische Mathematik. Im Fall des Sumatra-Bebens von 2004 schlugen die Wellen bereits eine Viertelstunde nach dem Erdbeben auf der Küste auf. Niemand kann in dieser Zeit eine Stadt evakuieren. Aber im Voraus berechnete Szenarien können die Einsatzplanung für die Hilfskräfte optimieren helfen. Für weiter entfernte Küstenabschnitte oder gar andere Länder lässt sich vorausberechnen, wann der Tsunami dort ankommt, wie stark seine Kraft sich auswirken wird und welche Küstenabschnitte gefährdet sind und somit evakuiert werden müssen. Dazu dient die mathematische Simulation. Mithilfe eines numerischen Verfahrens zur Lösung hydrodynamischer Gleichungen werden Tsunami-Modellierungen durchgeführt. Das klingt allerdings einfacher, als es ist, denn ein solches Modell setzt gute Kenntnisse vom auslösenden Prozess, von der Wassertiefe, von der Topographie des Meeresbodens und der Küstenbeschaffenheit voraus. Die Ausbreitungsgeschwindigkeit eines Tsunami hängt von der Wassertiefe ab. Im tiefen Meer entspricht sie der Geschwindigkeit eines Verkehrsflugzeuges, im flachen Wasser etwa der eines schnellen Radfahrers. Das hydrodynamische Gleichungssystem unterscheidet sog. Flachwassergleichungen von Tiefwassergleichungen; im Kern bedeutet das, dass vor allem die Ozeanbodenbeschaffenheit im flachen Wasser bekannt sein muss. Daher wurde die Küste vor Sumatra seit 2004, auch mit deutscher Hilfe, neu kartiert. Das ist für die Bestimmung der Randbedingungen des Gleichungssystems unerlässlich.

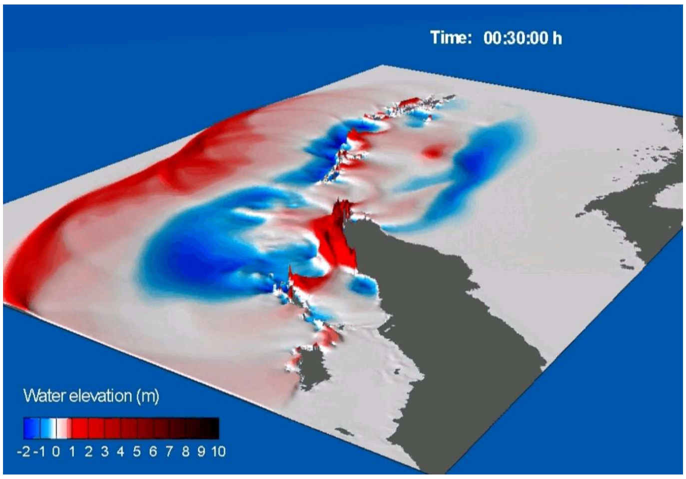

Der Tsunami vor der Küste Sumatras wird ausgelöst durch die vom Erdbeben verursachte Verformung des Meeresbodens. Er breitet sich mit hoher Geschwindigkeit über das offene Meer aus, wird in Küstennähe „aufgestaut“ und überflutet in einem komplizierten Ablauf das Land. Sämtliche Prozesse können angenähert physikalisch modelliert, mathematisch beschrieben und auf einem Computer simuliert werden.

Ausbreitungsszenarien

Aufgrund der extrem knappen Vorwarnzeit können solche Modelle nicht in Echtzeit berechnet werden. Daher berechnet man mögliche Szenarien im Voraus. So wurde eine große Anzahl von Simulationen (> 1000) für verschiedene Erdbebenlokationen entlang des Sundabogens mit unterschiedlichen Bebenstärken und Risslängen vorberechnet und in einer Datenbank abgelegt. Im Falle eines durch das Erdbebenmonitoringsystem und die ozeanografischen Messungen festgestellten Tsunami wird mit den gemessenen Parametern – Erdbebenlokation, Bebenstärke, Wellenhöhe im Ozean und an den Küstenpegeln sowie der Verschiebung der GPS-Stationen – die am besten zu der Situation passende vorberechnete Simulation herausgesucht. Dazu werden die gemessenen Parameter mit den Werten aller Szenarien in der Datenbank verglichen, und diejenige Simulation ausgewählt, die die geringste Abweichung aufweist. Diese Simulation wird in eine Gefährdungskarte, in denen die zu erwartende Wellenhöhe und -ankunftszeit für die verschiedenen Küstenbereiche zu erkennen sind, für die betreffenden Küstenabschnitte umgesetzt. Der gesamte Prozess läuft im Daten- und Frühwarnzentrum in wenigen Sekunden automatisiert ab. Die Karten werden dann vom Warnzentrum den zuständigen Behörden in den betroffenen Gebieten zur Verfügung gestellt, so dass diese ihrerseits alle notwendigen Maßnahmen in die Wege leiten können.

Das Daten- und Frühwarnzentrum: Auslösung des Alarms oder nicht?


Erdbebenbeobachtung im Warnzentrum in Jakarta, Indonesien.

Nicht jedes starke Erdbeben löst einen Tsunami aus. Die Entwarnung ist daher genau so wichtig wie die rechtzeitige Warnung. Im Datenzentrum laufen alle Daten zusammen. Hat das automatisch arbeitende Gesamtsystem auf „Alarm“ gestellt, muss im Warnzentrum die Entscheidung getroffen werden, ob alarmiert wird oder nicht. Dabei gibt es verschiedene Abstufungen, in der die Alarmierung verschiedener Organisationseinheiten erfolgt. So wird bereits nach 5 Minuten, wenn ein starkes Seebeben registriert wurde, ein interner Alarm gegeben und bestimmte Einheiten in den betroffenen Gebieten (Polizei, Feuerwehr, Katastrophenschutz) werden in Bereitschaft versetzt. Im Laufe der nächsten Minuten, wenn Daten von weiteren Messinstrumenten verfügbar und geprüft sind, wird der Alarm entsprechend weiter intensiviert oder auch wieder aufgehoben. Die Warnmeldungen werden über ein Geoinformationssystem mit weiteren Daten wie z.B. Evakuierungskarten, Informationen über Bevölkerungsdichten und kritische Infrastrukturen verschnitten. Im Ergebnis erhält man nach einer Zeit von etwa 10 Minuten ein Warndossier, das als Grundlage für die weiteren Maßnahmen herangezogen werden kann. Die Verteilung der Warnmeldung erfolgt zurzeit in Indonesien direkt vom Warnzentrum in Jakarta aus über verschiedene Kanäle. Wichtigster Kommunikationsweg ist eine direkte Telefonverbindung zu lokalen Polizeistationen, die weitere Aktivitäten wie z.B. Evakuierungen durchführen sollen. Daneben werden über Internet und Fax weitere Institutionen in Indonesien von einer Tsunamigefährdung unterrichtet. Zusätzlich werden SMS-Meldungen generiert sowie die Rundfunk- und Fernsehanstalten informiert. Ein Naturereignis wie der Tsunami von 2004 kann nicht verhindert werden und solche Katastrophen werden auch bei einem perfekt arbeitenden Alarmsystem weiterhin ihre Opfer fordern. Aber die Auswirkungen einer solchen Naturkatastrophe können mit einem Frühwarnsystem erheblich minimiert werden. Das ist das Ziel von GITEWS.

Bundesministerium
für Bildung
und Forschung

Das “German-Indonesian Tsunami Early Warning System” (GITEWS) ist ein Beitrag der Deutschen Bundesregierung zum Wiederaufbau der Infrastrukturen in der Region des Indischen Ozeans. Das Projekt wird durch das Bundesministerium für Bildung und Forschung (BMBF) gefördert.

Informationen zum Verhalten bei Starkbeben und Tsunamis finden sich im Merkblatt auf der Homepage des GFZ: http://www.gfz-potsdam.de. Weitere Informationen zum Tsunami-Frühwarnsystem für den Indischen Ozean: http://www.gitews.de

Wissenschaftsjahr 2008
Mathematik
Alles, was zählt

GFZ
Helmholtz-Zentrum
Potsdam

HELMHOLTZ
GEMEINSCHAFT

10.2 Earthquake and Tsunami energies

I compiled the simple formulae below to give an idea of the relations of the processes involved to the general public, but it turned out that also geoscientists could find themselves orders of magnitudes from the actual results, if asked to make a guess about the energies!

10.2.1 Earthquake moment

$M_0 = \mu \cdot B \cdot s$

μ: shear modulus ≈ 40 GPa = $4 \cdot 10^{10}$ N/m^2
B: size of the ruptured area in m^2
s: average slip at the fault in m

e.g. for Sumatra 2004:
B = *length·width* of the ruptured area = 1000 km · 200 km = $2 \cdot 10^{11}$ m^2
s = 10 m
=> $M_0 = 4 \cdot 10^{10}\ Nm^{-2} \cdot 10^{11}\ m^2 \cdot 10\ m = 8 \cdot 10^{22}\ Nm = 8 \cdot 10^{22}\ J$

This corresponds approximately to the electric energy produced by a nuclear power plant in a million years.

10.2.2 Magnitude

$$M_W = \frac{2}{3}\log_{10} M_0 - 6{,}1$$

e.g. for Sumatra 2004:

$$M_W = \frac{2}{3}\log_{10}(8 \cdot 10^{22}) - 6{,}1 \approx \frac{2}{3} \cdot 22{,}9 - 6{,}1 \approx 9{,}2$$

10.2.3 Energy of the seismic waves

$$E_{Seis} = 1{,}6 \cdot 10^{-5} M_0$$

e.g. for Sumatra 2004:
$E_{Seis} \approx 1.3 \cdot 10^{18}$ J

This corresponds approximately to the electric energy produced by a nuclear power plant in 30 years.

10.2.4 Energy of the tsunami

$$E_{Tsun} = \frac{A \cdot g \cdot \rho}{2} \cdot h^2$$

A: size of the uplifted area in m^2
g: gravitational acceleration ≈ 10 m/s
ρ: density of the water ≈ 1000 kg/m^3
h: average uplift in m

e.g. for Sumatra 2004:

$$A = length \cdot width = 100'000\ \mathrm{km}^2 = 10^{11}\ \mathrm{m}^2$$
$$h = 4\ \mathrm{m}$$
$$\Rightarrow E = \frac{1}{2} \cdot 10^{11} \cdot 10 \cdot 1000 \cdot 4^2\ \frac{\mathrm{kg} \cdot \mathrm{m}^2}{\mathrm{s}^2} = 8 \cdot 10^{15}\ \mathrm{J}$$

This corresponds approximately to the electric energy produced by a nuclear power plant in two months.

10.3 A tsunami exercise

I made the following exercise for the lectures I gave at the GITEWS training course in Jakarta in 2009. Participants were staff (or future staff) of tsunami early warning centers of the Indian Ocean.

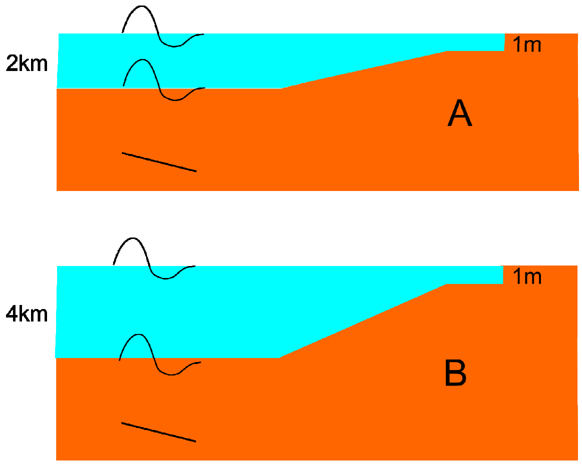

Figure 10.1 Two tsunami initial conditions.

The two tsunami scenarios shown in Figure 10.1 have identical initial sea floor (and sea surface) deformation but different ocean depth.

10.3.1 Which tsunami arrives first at the coast?

In linear shallow water approximation, the velocity of a tsunami depends only on the depth of the ocean:

$$v = \sqrt{g \cdot D}$$

with gravitational acceleration $g \approx 10$ m/s^2 and water depth D in [m].

For
A: $v \approx 504$ km/h
B: $v \approx 713$ km/h

The deeper the ocean, the faster the tsunami.

10.3.2 Which tsunami has higher amplitude when it hits the coast?

When reaching shallower water, the tsunami undergoes ‘compression’, it becomes higher and shorter (in space). The amplification factor is

$$a = \sqrt{\sqrt{\frac{D_1}{D_2}}}$$

D_1 being water depth in deep- D_2 in shallow water.

For
A: $a = 6.9$
B: $a = 8.0$

The tsunami originating in deeper water experiences more compression.

But be aware: don't multiply initial wave height with amplification factor to obtain run up, other factors are also important, e.g. geometrical spreading, focusing effects and nonlinear interactions at the coast!

10.3.3 Which tsunami lasts longer (has longer period)?

Assume wave length $l = 70$ km. $T = l/v$

For
A: $T = 500$ s
B: $T = 353$ s

The tsunami from the deeper water is faster and hence has a shorter period.

Note: the period does not change when the tsunami enters shallower water.

10.3.4 Which tsunami has more energy?

Tsunami energy is given by:

$$E_T = \frac{1}{2}\rho \cdot g \int z^2 dA$$

with z: sea surface elevation anomaly, water density $\rho \approx 1000$ kg/m3, gravitational acceleration g≈ 10 m/s2,.

That is, not the whole water column contributes to the available energy, only the part lifted above the sea level.

Simplify by assuming an initial uplift of cross section as shown in Figure 10.2 and length $L = 800$ km (breadth of the wave):

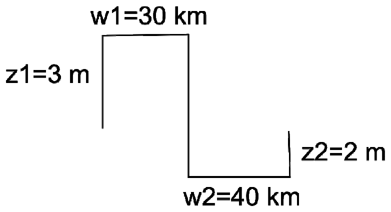

Figure 10.2 Simplified tsunami initial condition.

For the given initial condition, above formula simplifies to:

$$E_T = 0.5 \cdot \rho \cdot g \cdot L \cdot \sum_{i=1}^{2} z_i^2 \cdot w_i$$

$$E_T = 0.5 \cdot 1000 \cdot 10 \cdot 8e5 \cdot (3^2 \cdot 3 \cdot 10^4 + 2^2 \cdot 4 \cdot 10^4)\ \text{J} = 1.7 \cdot 10^{15}\ \text{J}$$

The energy of a tsunami does not depend on the depth of the water where it was created!

Nevertheless, equal total energy of the two tsunamis does not mean that they have the same impact. Amplitude, period, number of waves etc. at some location at the coast are the important factors.

11 Publications

Table 11.1 Publications as of September 2010.

2007	Tsunami early warning using GPS-Shield arrays; Journal of Geophysical Research; S.V. Sobolev, A.Y. Babeyko, R. Wang, A. Hoechner, R. Galas, M. Rothacher, D.V. Sein, J. Schroeter, J. Lauterjung, C. Subarya; (Chapter 7)
2008	Enhanced GPS inversion technique applied to the 2004 Sumatra earthquake and tsunami; Geophysical Research Letters; A. Hoechner, A.Y. Babeyko, S.V. Sobolev; (Chapter 3)
2010	Simulation of space-borne tsunami detection using GNSS-Reflectometry applied to tsunamis in the Indian Ocean; Natural Hazards and Earth System Sciences; R. Stosius, G. Beyerle, A. Helm, A. Hoechner, J. Wickert; (not included in thesis)
2010	Source modeling and inversion with near real-time GPS: a GITEWS perspective for Indonesia; Natural Hazards and Earth System Sciences; A.Y. Babeyko, A. Hoechner, S.V. Sobolev; (Chapter 8)
2010, accepted	Gravity changes due to the Sumatra-Andaman and Nias Earthquakes as detected by the GRACE satellites; Geophysical Journal International; I. Einarsson, A. Hoechner, R. Wang, J. Kusche; (not included in thesis)
2010, submitted	Postseismic deformation and geoid change caused by the 2004 Sumatra earthquake allow distinguishing between transient (Burgers) and steady-state (Maxwell) rheology of the asthenosphere; A. Hoechner, S.V. Sobolev, I. Einarsson, R. Wang; (Chapter 5)
2010, to be submitted	Deriving Earthquake Rupture Timing from GPS Observations; A. Hoechner, S.V. Sobolev; (Chapter 6)

12 References

Ammon, C.J., Ji, C., Thio, H.-K., Robinson, D., Ni, S., Hjorleifsdottir, V., Kanamori, H., Lay, T., Das, S., Helmberger, D., Ichinose, G., Polet, J., and Wald, D., 2005, Rupture Process of the 2004 Sumatra-Andaman Earthquake: Science, v. 308, no. 5725, p. 1133-1139, doi: 10.1126/science.1112260.

Babeyko, A.Y., Hoechner, A., and Sobolev, S.V., 2010, Source modeling and inversion with near real-time GPS: a GITEWS perspective for Indonesia: Natural Hazards and Earth System Sciences, v. 10, no. 7, p. 1617-1627, doi: 10.5194/nhess-10-1617-2010.

Banerjee, P., Pollitz, F., and Burgmann, R., 2005, The Size and Duration of the Sumatra-Andaman Earthquake from Far-Field Static Offsets: Science, v. 308, no. 5729, p. 1769-1772, doi: 10.1126/science.1113746.

Banerjee, P., Pollitz, F., Nagarajan, B., and Bürgmann, R., 2007, Coseismic Slip Distributions of the 26 December 2004 Sumatra-Andaman and 28 March 2005 Nias Earthquakes from GPS Static Offsets: Bulletin of the Seismological Society of America, v. 97, no. 1A, p. S86-102, doi: 10.1785/0120050609.

Barrientos, S.E., and Ward, S.N., 1990, The 1960 Chile earthquake: inversion for slip distribution from surface deformation: Geophysical Journal International, v. 103, no. 3, p. 589-598, doi: 10.1111/j.1365-246X.1990.tb05673.x.

Bassin, C., Laske, G., and Masters G., 2000, The Current Limits of Resolution for Surface Wave Tomography in North America: EOS Trans AGU, v. 81, p. F897.

Behrens, J., Androsov, A., Babeyko, A.Y., Harig, S., Klaschka, F., and Mentrup, L., 2010, A new multi-sensor approach to simulation assisted tsunami early warning: Natural Hazards and Earth System Sciences, v. 10, no. 6, p. 1085-1100, doi: 10.5194/nhess-10-1085-2010.

Blewitt, G., Hammond, W., Kreemer, C., Plag, H.-P., Stein, S., and Okal, E., 2009, GPS for real-time earthquake source determination and tsunami warning systems: Journal of Geodesy, v. 83, no. 3, p. 335-343, doi: 10.1007/s00190-008-0262-5.

Blewitt, G., Kreemer, C., Hammond, W.C., Plag, H.-P., Stein, S., and Okal, E., 2006, Rapid determination of earthquake magnitude using GPS for tsunami warning systems: Geophysical Research Letters, v. 33, no. 11, doi: 10.1029/2006GL026145.

Bock, Y., Nikolaidis, R.M., Jonge, P.J. de, and Bevis, M., 2000, Instantaneous geodetic positioning at medium distances with the Global Positioning System: Journal of Geophysical Research, v. 105, no. B12, p. PP. 28,223-28,253, doi: 200010.1029/2000JB900268.

Bock, Y., Prawirodirdjo, L., and Melbourne, T.I., 2004, Detection of arbitrarily large dynamic ground motions with a dense high-rate GPS network: Geophysical Research Letters, v. 31, p. 4 PP., doi: 200410.1029/2003GL019150.

Boebel, O., Busack, M., Flüh, E., Gouretski, V., Rohr, H., Macrander, A., Krabbenhöft, A., Motz, M., and Radtke, T., 2010, The GITEWS ocean bottom sensor packages: Natural Hazards and Earth System Sciences,.

Boore, D.M., 1983, Stochastic simulation of high-frequency ground motions based on seismological models of the radiated spectra: Bulletin of the Seismological Society of America, v. 73, no. 6A, p. 1865-1894.

Borrero, J.C., Sieh, K., Chlieh, M., and Synolakis, C.E., 2006, Tsunami inundation modeling for western Sumatra: Proceedings of the National Academy of Sciences, v. 103, no. 52, p. 19673-19677, doi: 10.1073/pnas.0604069103.

Briggs, R.W., Sieh, K., Meltzner, A.J., Natawidjaja, D., Galetzka, J., Suwargadi, B., Hsu, Y.-ju, Simons, M., Hananto, N., Suprihanto, I., Prayudi, D., Avouac, J.-P., Prawirodirdjo, L., and Bock, Y., 2006, Deformation and Slip Along the Sunda Megathrust in the Great 2005 Nias-Simeulue Earthquake: Science, v. 311, no. 5769, p. 1897-1901, doi: 10.1126/science.1122602.

Brune, J.N., 1970, Tectonic Stress and the Spectra of Seismic Shear Waves from Earthquakes: Journal of Geophysical Research, v. 75, no. 26, p. PAGES 4997–5009.

Brune, S., 2009, Landslide generated tsunamis: numerical modeling and real-time prediction: Thesis; University Potsdam, Germany; URL: http://opus.kobv.de/ubp/volltexte/2009/3298/.

Bürgmann, R., and Dresen, G., 2008, Rheology of the Lower Crust and Upper Mantle: Evidence from Rock Mechanics, Geodesy, and Field Observations: Annual Review of Earth and Planetary Sciences, v. 36, no. 1, p. 531-567, doi: 10.1146/annurev.earth.36.031207.124326.

Cannelli, V., Melini, D., Piersanti, A., and Boschi, E., 2008, Postseismic signature of the 2004 Sumatra earthquake on low-degree gravity harmonics: Journal of Geophysical Research, v. 113, p. B12414, doi: 10.1029/2007JB005296.

Catherine, J.K., Gahalaut, V.K., and Sahu, V.K., 2005, Constraints on rupture of the December 26, 2004, Sumatra earthquake from far-field GPS observations: Earth and Planetary Science Letters, v. 237, no. 3-4, p. 673-679, doi: 10.1016/j.epsl.2005.07.012.

Chen, J.L., Wilson, C.R., Tapley, B.D., and Grand, S., 2007, GRACE detects coseismic and postseismic deformation from the Sumatra-Andaman earthquake: Geophysical Research Letters, v. 34, p. 5 PP., doi: 200710.1029/2007GL030356.

Chlieh, M., Avouac, J.P., Sieh, K., Natawidjaja, D.H., and Galetzka, J., 2008, Heterogeneous coupling of the Sumatran megathrust constrained by geodetic and paleogeodetic measurements: Journal of Geophysical Research, v. 113, p. B05305, doi: 10.1029/2007JB004981.

Chlieh, M., Avouac, J.-P., Hjorleifsdottir, V., Song, T.-R.A., Ji, C., Sieh, K., Sladen, A., Hebert, H., Prawirodirdjo, L., Bock, Y., and Galetzka, J., 2007, Coseismic Slip and Afterslip of the Great Mw 9.15 Sumatra-Andaman Earthquake of 2004: Bulletin of the Seismological Society of America, v. 97, no. 1A, p. S152-173, doi: 10.1785/0120050631.

Chlieh, M., Chabalier, J.B. de, Ruegg, J.C., Armijo, R., Dmowska, R., Campos, J., and Feigl, K.L., 2004, Crustal deformation and fault slip during the seismic cycle in the North Chile subduction zone, from GPS and InSAR observations: Geophysical Journal International, v. 158, no. 2, p. 695-711, doi: 10.1111/j.1365-246X.2004.02326.x.

Delouis, B., Nocquet, J.-M., and Vallée, M., 2010, Slip distribution of the February 27, 2010 Mw = 8.8 Maule Earthquake, central Chile, from static and high-rate GPS, InSAR, and broadband teleseismic data: Geophysical Research Letters, v. 37, no. 17, doi: 10.1029/2010GL043899.

Dziewonski, A.M., and Anderson, D.L., 1981, Preliminary reference Earth model: Physics of the Earth and Planetary Interiors, v. 25, no. 4, p. 297-356.

Einarsson, I., Hoechner, A., Wang, R., and Kusche, J., 2010, Gravity changes due to the Sumatra-Andaman and Nias earthquakes as detected by the GRACE satellites: a reexamination: Geophysical Journal International, v. 183, no. 2, p. 733-747, doi: 10.1111/j.1365-246X.2010.04756.x.

Engdahl, E.R., Villasenor, A., DeShon, H.R., and Thurber, C.H., 2007, Teleseismic Relocation and Assessment of Seismicity (1918-2005) in the Region of the 2004 Mw 9.0 Sumatra-Andaman and 2005 Mw 8.6 Nias Island Great Earthquakes: Bulletin of the Seismological Society of America, v. 97, no. 1A, p. S43-61, doi: 10.1785/0120050614.

Falck, C., Ramatschi, M., Subarya, C., Bartsch, M., Merx, A., Hoeberechts, J., and Schmidt, G., 2010, Near real-time GPS applications for tsunami early warning systems: Natural Hazards and Earth System Sciences, v. 10, no. 2, p. 181-189, doi: 10.5194/nhess-10-181-2010.

Fleischer, J., Häner, R., Herrnkind, S., Kloth, A., Kriegel, U., Schwarting, H., and Wächter, J., 2010, An integration platform for heterogeneous sensor systems in GITEWS – Tsunami Service Bus: Natural Hazards and Earth System Sciences, v. 10, no. 6, p. 1239-1252, doi: 10.5194/nhess-10-1239-2010.

Freed, A., Burgmann, R., Calais, E., and Freymueller, J., 2006, Stress-dependent power-law flow in the upper mantle following the 2002 Denali, Alaska, earthquake: Earth and Planetary Science Letters, v. 252, no. 3-4, p. 481-489, doi: 10.1016/j.epsl.2006.10.011.

Freed, A.M., and Burgmann, R., 2004, Evidence of power-law flow in the Mojave desert mantle: Nature, v. 430, no. 6999, p. 548-551, doi: 10.1038/nature02784.

Freed, A.M., Herring, T., and Bürgmann, R., 2010, Steady-state laboratory flow laws alone fail to explain postseismic observations: Earth and Planetary Science Letters, v. 300, no. 1-2, p. 1-10, doi: 10.1016/j.epsl.2010.10.005.

Freund, L.B., and Barnett, D.M., 1976, A two-dimensional analysis of surface deformation due to dip-slip faulting: Bulletin of the Seismological Society of America, v. 66, no. 3, p. 667-675.

Freymueller, J.T., 2005, Real Time GPS Magnitudes for the Largest Earthquakes, and Application to Tsunami Warning: AGU Spring Meeting Abstracts, v. 51, p. 05.

Fujii, Y., and Satake, K., 2006, Source of the July 2006 West Java tsunami estimated from tide gauge records: Geophysical Research Letters, v. 33, no. 24, doi: 10.1029/2006GL028049.

Gahalaut, V.K., Nagarajan, B., Catherine, J.K., and Kumar, S., 2006, Constraints on 2004 Sumatra-Andaman earthquake rupture from GPS measurements in Andaman-Nicobar Islands: Earth and Planetary Science Letters, v. 242, no. 3-4, p. 365-374, doi: 10.1016/j.epsl.2005.11.051.

Geist, E.L., 2002, Complex earthquake rupture and local tsunamis: Journal of Geophysical Research, v. 107, no. B5, p. 10.1029/2000JB000139.

Geist, E.L., 1998, Local Tsunamis and Earthquake Source Parameters, *in* Tsunamigenic Earthquakes and Their Consequences, Elsevier, p. 117-209.

Geist, E.L., and Dmowska, R., 1999, Local Tsunamis and Distributed Slip at the Source: Pure and Applied Geophysics, v. 154, no. 3, p. 485-512, doi: 10.1007/s000240050241.

Geist, E.L., Bilek, S.L., Arcas, D., and Titov, V.V., 2006, Differences in tsunami generation between the December 26, 2004 and March 28, 2005 Sumatra earthquakes: Earth, Planets and Space, , no. 58, p. 2.

Gudmundsson, Ó., and Sambridge, M., 1998, A regionalized upper mantle (RUM) seismic model: Journal of Geophysical Research, v. 103, no. B4, p. PP. 7121-7136, doi: 199810.1029/97JB02488.

Hanert, E., Roux, D.Y.L., Legat, V., and Deleersnijder, E., 2005, An efficient Eulerian finite element method for the shallow water equations: Ocean Modelling, v. 10, no. 1-2, p. 115-136, doi: 10.1016/j.ocemod.2004.06.006.

Hanka, W., Saul, J., Weber, B., Becker, J., and GITEWS Team, 2008, Timely regional tsunami warning and rapid global earthquake monitoring, ORFEUS Newsletter - June 2008:.

Han, S.C., and Simons, F.J., 2008, Spatiospectral localization of global geopotential fields from the Gravity Recovery and Climate Experiment (GRACE) reveals the coseismic gravity change owing to the 2004 Sumatra-Andaman earthquake: Journal of Geophysical Research - Solid Earth, v. 113, no. B1, doi: 10.1029/2007JB004927.

Han, S.C., Sauber, J., Luthcke, S.B., Ji, C., and Pollitz, F., 2008, Implications of postseismic gravity change following the great 2004 Sumatra-Andaman earthquake from the regional harmonic analysis of GRACE intersatellite tracking data: Journal of Geophysical Research, v. 113, no. B11, doi: 10.1029/2008JB005705.

Han, S.C., Shum, C.K., Bevis, M., Ji, C., and Kuo, C.-Y., 2006, Crustal Dilatation Observed by GRACE After the 2004 Sumatra-Andaman Earthquake: Science, v. 313, no. 5787, p. 658-662, doi: 10.1126/science.1128661.

Harig, S., Chaeroni, Pranowo, W.S., and Behrens, J., 2008, Tsunami simulations on several scales: Ocean Dynamics, v. 58, no. 5, p. 429-440, doi: 10.1007/s10236-008-0162-5.

Hoechner, A., Babeyko, A.Y., and Sobolev, S.V., 2008, Enhanced GPS inversion technique applied to the 2004 Sumatra earthquake and tsunami: Geophysical Research Letters, v. 35, p. 5 PP., doi: 200810.1029/2007GL033133.

Hoechner, A., Babeyko, A.Y., Sobolev, S.V., and Brune, S., 2006, Slip Distribution of Recent Sunda Trench Earthquakes: Reconciling 3D GPS Inversions with Seismological and Ocean Measurements: AGU Fall Meeting Abstracts, v. 53, p. 0034.

Hoechner, A., Sobolev, S.V., Einarsson, I., and Wang, R., 2011, Investigation on afterslip, steady-state- and transient rheology based on postseismic deformation and geoid change caused by the Sumatra 2004 earthquake: Geochemistry Geophysics Geosystems,, doi: 10.1029/2010GC003450.

Hyndman, R.D., Rogers, G.C., Dragert, H., Wang, K., Clague, J.J., Adams, J., and Bobrowsky, P.T., 1996, Giant Earthquakes Beneath Canada's West Coast: Geoscience Canada, v. 23, no. 2.

IGS International GNSS Service, formerly the International GPS Service: http://igscb.jpl.nasa.gov/,.

Imamura, F., Goto, C., Ogawa, Y., and Shuto, N., 1997, IUGG/IOC Time Project:.

Irikura, K., 1983, Semi-empirical estimation of strong ground motions during large earthquakes: Bulletin of the Disaster Prevention Research Institute, v. 33, no. 297, p. 63-104.

Ishii, M., Shearer, P.M., Houston, H., and Vidale, J.E., 2005, Extent, duration and speed of the 2004 Sumatra-Andaman earthquake imaged by the Hi-Net array: Nature, v. 435, no. 7044, p. 933-936, doi: 10.1038/nature03675.

Jade, J., Ananda, M.B., Kumar, P.D., and Banerjee, S., 2005, Co-seismic and postseismic displacements in Andaman and Nicobar Islands from GPS measurements: Curr. Sci., , no. 88, p. 1980-1984.

Ji, C., Wald, D.J., and Helmberger, D.V., 2002, Source Description of the 1999 Hector Mine, California, Earthquake, Part I: Wavelet Domain Inversion Theory and Resolution Analysis: Bulletin of the Seismological Society of America, v. 92, no. 4, p. 1192-1207, doi: 10.1785/0120000916.

Kamigaichi, O., 2009, Tsunami forecasting and warning, *in* Encyclopedia of Complexity and Systems Science, Springer, Edited by R. A. Meyers, p. 9592-9618.

Kanamori, H., and Stewart, G.S., 1979, A slow earthquake: Physics of The Earth and Planetary Interiors, v. 18, no. 3, p. 167-175, doi: 10.1016/0031-9201(79)90112-2.

Karato, S.-I., 2008, Deformation of Earth Materials: An Introduction to the Rheology of Solid Earth: Cambridge University Press.

Kennett, B.L.N., and Engdahl, E.R., 1991, Traveltimes for global earthquake location and phase identification: Geophysical Journal International, v. 105, no. 2, p. 429-465, doi: 10.1111/j.1365-246X.1991.tb06724.x.

Kennett, B.L.N., Engdahl, E.R., and Buland, R., 1995, Constraints on seismic velocities in the Earth from traveltimes: Geophysical Journal International, v. 122, no. 1, p. 108-124, doi: 10.1111/j.1365-246X.1995.tb03540.x.

Konca, A.O., Avouac, J.-P., Sladen, A., Meltzner, A.J., Sieh, K., Fang, P., Li, Z., Galetzka, J., Genrich, J., Chlieh, M., Natawidjaja, D.H., Bock, Y., Fielding, E.J., Ji, C., and Helmberger, D.V., 2008, Partial rupture of a locked patch of the Sumatra megathrust during the 2007 earthquake sequence: Nature, v. 456, no. 7222, p. 631-635, doi: 10.1038/nature07572.

Konca, A.O., Hjorleifsdottir, V., Song, T.-R.A., Avouac, J.-P., Helmberger, D.V., Ji, C., Sieh, K., Briggs, R., and Meltzner, A., 2007, Rupture Kinematics of the 2005 Mw 8.6 Nias-Simeulue Earthquake from the Joint Inversion of Seismic and Geodetic Data: Bulletin of the Seismological Society of America, v. 97, no. 1A, p. S307-322, doi: 10.1785/0120050632.

Krüger, F., and Ohrnberger, M., 2005a, Spatio-temporal source characteristics of the 26 December 2004 Sumatra earthquake as imaged by teleseismic broadband arrays: Geophysical Research Letters, v. 32, no. 24, doi: 10.1029/2005GL023939.

Krüger, F., and Ohrnberger, M., 2005b, Tracking the rupture of the Mw = 9.3 Sumatra earthquake over 1,150 km at teleseismic distance: Nature, v. 435, no. 7044, p. 937-939, doi: 10.1038/nature03696.

Kusche, J., 2007, Approximate decorrelation and non-isotropic smoothing of time-variable GRACE-type gravity field models: Journal of Geodesy, v. 81, no. 11, p. 733-749, doi: 10.1007/s00190-007-0143-3.

Lauterjung, J., Münch, U., and Rudloff, A., 2010, The challenge of installing a tsunami early warning system in the vicinity of the Sunda Arc, Indonesia: Natural Hazards and Earth System Sciences, v. 10, no. 4, p. 641-646, doi: 10.5194/nhess-10-641-2010.

Lay, T., Kanamori, H., Ammon, C.J., Nettles, M., Ward, S.N., Aster, R.C., Beck, S.L., Bilek, S.L., Brudzinski, M.R., Butler, R., DeShon, H.R., Ekstrom, G., Satake, K., and Sipkin, S., 2005, The Great Sumatra-Andaman Earthquake of 26 December 2004: Science, v. 308, no. 5725, p. 1127-1133, doi: 10.1126/science.1112250.

Lee, W.H.K., Kanamori, H., Jennings, P.C., and Kisllinger, C., 2003, International handbook of earthquake and engineering seismology: Academic Press.

Lorito, S., Romano, F., Piatanesi, A., and Boschi, E., 2008, Source process of the September 12, 2007, MW 8.4 southern Sumatra earthquake from tsunami tide gauge record inversion: Geophysical Research Letters, v. 35, p. 6 PP., doi: 200810.1029/2007GL032661.

Maerten, F., Resor, P., Pollard, D., and Maerten, L., 2005, Inverting for Slip on Three-Dimensional Fault Surfaces Using Angular Dislocations: Bulletin of the Seismological Society of America, v. 95, no. 5, p. 1654-1665, doi: 10.1785/0120030181.

Masterlark, T., and Hughes, K.L.H., 2008, Next generation of deformation models for the 2004 M9 Sumatra-Andaman earthquake: Geophysical Research Letters, v. 35, no. 19, doi: 10.1029/2008GL035198.

Matlab R2009a, The Mathworks Inc.

Mazzotti, S., Dragert, H., Henton, J., Schmidt, M., Hyndman, R., James, T., Lu, Y., and Craymer, M., 2003, Current tectonics of northern Cascadia from a decade of GPS measurements: Journal of Geophysical Research, v. 108, p. 18 PP., doi: 200310.1029/2003JB002653.

McCaffrey, R., 2009, The Tectonic Framework of the Sumatran Subduction Zone: Annual Review of Earth and Planetary Sciences, v. 37, no. 1, p. 345-366, doi: 10.1146/annurev.earth.031208.100212.

McCloskey, J., Nalbant, S.S., and Steacy, S., 2005, Indonesian earthquake: Earthquake risk from co-seismic stress: Nature, v. 434, no. 7031, p. 291, doi: 10.1038/434291a.

Meltzner, A.J., Sieh, K., Abrams, M., Agnew, D.C., Hudnut, K.W., Avouac, J.-P., and Natawidjaja, D.H., 2006, Uplift and subsidence associated with the great Aceh-Andaman earthquake of 2004: Journal of Geophysical Research, v. 111, p. 8 PP., doi: 200610.1029/2005JB003891.

Menke, W., Abend, H., Bach, D., Newman, K., and Levin, V., 2006, Review of the source characteristics of the Great Sumatra–Andaman Islands earthquake of 2004: Surveys in Geophysics, v. 27, no. 6, p. 603-613, doi: 10.1007/s10712-006-9013-4.

Mignan, A., King, G., Bowman, D., Lacassin, R., and Dmowska, R., 2006, Seismic activity in the Sumatra-Java region prior to the December 26, 2004 (Mw = 9.0-9.3) and March 28, 2005 (Mw = 8.7) earthquakes: Earth and Planetary Science Letters, v. 244, no. 3-4, p. 639-654, doi: 10.1016/j.epsl.2006.01.058.

Mooney, W.D., Laske, G., and Masters, T.G., 1998, CRUST 5.1: A global crustal model at 5° × 5°: Journal of Geophysical Research, v. 103, no. B1, p. PAGES 727–747.

Moreno, M.S., Bolte, J., Klotz, J., and Melnick, D., 2009, Impact of megathrust geometry on inversion of coseismic slip from geodetic data: Application to the 1960 Chile earthquake: Geophysical Research Letters, v. 36, no. 16, doi: 10.1029/2009GL039276.

Müller, G., 1986, Generalized Maxwell bodies and estimates of mantle viscosity: Geophysical Journal International, v. 87, no. 3, p. 1113-1141, doi: 10.1111/j.1365-246X.1986.tb01986.x.

Nalbant, S.S., Steacy, S., Sieh, K., Natawidjaja, D., and McCloskey, J., 2005, Seismology: Earthquake risk on the Sunda trench: Nature, v. 435, no. 7043, p. 756-757, doi: 10.1038/nature435756a.

Ogawa, R., and Heki, K., 2007, Slow postseismic recovery of geoid depression formed by the 2004 Sumatra-Andaman Earthquake by mantle water diffusion: Geophysical Research Letters, v. 34, no. 6, doi: 10.1029/2007GL029340.

Okada, Y., 1985, Surface deformation due to shear and tensile faults in a half-space: Bulletin of the Seismological Society of America, v. 75, no. 4, p. 1135-1154.

Okal, E.A., 1988, Seismic parameters controlling far-field tsunami amplitudes: A review: Natural Hazards, v. 1, no. 1, p. 67-96, doi: 10.1007/BF00168222.

Panet, I., Mikhailov, V., Diament, M., Pollitz, F., King, G., de Viron, O., Holschneider, M., Biancale, R., and Lemoine, J.-M., 2007, Coseismic and post-seismic signatures of the Sumatra 2004 December and 2005 March earthquakes in GRACE satellite gravity: Geophysical Journal International, v. 171, no. 1, p. 177-190, doi: 10.1111/j.1365-246X.2007.03525.x.

Panet, I., Pollitz, F., Mikhailov, V., Diament, M., Banerjee, P., and Grijalva, K., 2010, Upper mantle rheology from GRACE and GPS postseismic deformation after the 2004 Sumatra-Andaman earthquake: Geochem. Geophys. Geosyst., v. 11, no. 6, p. Q06008, doi: 10.1029/2009GC002905.

Park, J., Song, T.-R.A., Tromp, J., Okal, E., Stein, S., Roult, G., Clevede, E., Laske, G., Kanamori, H., Davis, P., Berger, J., Braitenberg, C., Van Camp, M., Lei, X., Sun, H., et al., 2005, Earth’s Free Oscillations Excited by the 26 December 2004 Sumatra-Andaman Earthquake: Science, v. 308, no. 5725, p. 1139-1144, doi: 10.1126/science.1112305.

Paul, J., Lowry, A.R., Bilham, R., Sen, S., and Smalley, R., 2007, Postseismic deformation of the Andaman Islands following the 26 December, 2004 Great Sumatra–Andaman earthquake: Geophysical Research Letters, v. 34, no. 19, doi: 10.1029/2007GL031024.

Petersen, M.D., Dewey, J., Hartzell, S., Mueller, C., Harmsen, S., Frankel, A., and Rukstales, K., 2004, Probabilistic seismic hazard analysis for Sumatra, Indonesia and across the Southern Malaysian Peninsula: Tectonophysics, v. 390, no. 1-4, p. 141-158, doi: doi: DOI: 10.1016/j.tecto.2004.03.026.

Pietrzak, J., Socquet, A., Ham, D., Simons, W., Vigny, C., Labeur, R.J., Schrama, E., Stelling, G., and Vatvani, D., 2007, Defining the source region of the Indian Ocean Tsunami from GPS, altimeters, tide gauges and tsunami models: Earth and Planetary Science Letters, v. 261, no. 1-2, p. 49-64, doi: 10.1016/j.epsl.2007.06.002.

Plafker, G., Cluff, L.S., Lloyd, X., Nishenko, S.P., Stuart, Y., and Syahrial, D., 2007, Evidence for a secondary tectonic source for the cataclysmic tsunami of 12/26/2004 on NW Sumatra: Seismological Society of America, v. Annual meeting, Hawaii.

Pollitz, F., 2003, Transient rheology of the uppermost mantle beneath the Mojave Desert, California: Earth and Planetary Science Letters, v. 215, no. 1-2, p. 89-104, doi: 10.1016/S0012-821X(03)00432-1.

Pollitz, F., Banerjee, P., Bürgmann, R., Hashimoto, M., and Choosakul, N., 2006, Stress changes along the Sunda trench following the 26 December 2004 Sumatra-Andaman and 28 March 2005 Nias earthquakes: Geophysical Research Letters, v. 33, p. 4 PP., doi: 200610.1029/2005GL024558.

Pollitz, F., Banerjee, P., Grijalva, K., Nagarajan, B., and Bürgmann, R., 2008, Effect of 3-D viscoelastic structure on post-seismic relaxation from the 2004 M= 9.2 Sumatra earthquake: Geophysical Journal International, v. 173, no. 1, p. 189-204, doi: 10.1111/j.1365-246X.2007.03666.x.

Pollitz, F., Bürgmann, R., and Banerjee, P., 2006, Post-seismic relaxation following the great 2004 Sumatra-Andaman earthquake on a compressible self-gravitating Earth: Geophysical Journal International, v. 167, no. 1, p. 397-420, doi: 10.1111/j.1365-246X.2006.03018.x.

Press, W.H., Teukolsky, W.T., Vetterling, W.T., and Flannery, B.P., 1992, Numerical Recipies in C: The Art of Scientific Computing: Cambridge University Press.

Ranalli, G., 1995, Rheology of the Earth: Springer.

Roessler, D., Krueger, F., Ohrnberger, M., and Ehlert, L., 2010, Rapid characterisation of large earthquakes by multiple seismic broadband arrays: Natural Hazards and Earth System Sciences, v. 10, no. 4, p. 923-932, doi: 10.5194/nhess-10-923-2010.

Rudloff, A., Lauterjung, J., Münch, U., and Tinti, S., 2009, Preface "The GITEWS Project (German-Indonesian Tsunami Early Warning System):" Natural Hazards and Earth System Sciences, v. 9, no. 4, p. 1381-1382, doi: 10.5194/nhess-9-1381-2009.

Schmidt, R., Flechtner, F., Meyer, U., Neumayer, K.-H., Dahle, C., König, R., and Kusche, J., 2008, Hydrological Signals Observed by the GRACE Satellites: Surveys in Geophysics, v. 29, no. 4-5, p. 319-334, doi: 10.1007/s10712-008-9033-3.

Schöne, T., Subarya, C., Manurung, P., Nölte, C., Roemer, S., Galas, R., Illigner, J., Kloth, A., Köppl, M., Queisser, T., Selke, C., Stolarczuk, N., and Bartsch, M., 2008, Offshore and onshore sea level measurements: Proceedings of the International Conference on Tsunami Warning (ICTW), Bali, Indonesia,.

SEAMERGES South-East Asia: Mastering Environmental Research with GEodetic techniques: http://www.deos.tudelft.nl/seamerges/,.

Sibuet, J.-C., Rangin, C., Le Pichon, X., Singh, S., Cattaneo, A., Graindorge, D., Klingelhoefer, F., Lin, J.-Y., Malod, J., Maury, T., Schneider, J.-L., Sultan, N., Umber, M., and Yamaguchi, H., 2007, 26th December 2004 great Sumatra-Andaman earthquake: Co-seismic and post-seismic motions in northern Sumatra: Earth and Planetary Science Letters, v. 263, no. 1-2, p. 88-103, doi: 10.1016/j.epsl.2007.09.005.

Sieh, K., Natawidjaja, D.H., Chlieh, M., Galetzka, J., Avouac, J., Suwargadi, B.W., Edwards, R., and Cheng, H., 2004, The giant subduction earthquakes of 1797 and 1833, West Sumatra: Characteristic couplets, uncharacteristic slip: AGU Fall Meeting Abstracts, v. 12, p. 04.

Sieh, K., Natawidjaja, D.H., Meltzner, A.J., Shen, C.-C., Cheng, H., Li, K.-S., Suwargadi, B.W., Galetzka, J., Philibosian, B., and Edwards, R.L., 2008, Earthquake Supercycles Inferred from Sea-Level Changes Recorded in the Corals of West Sumatra: Science, v. 322, no. 5908, p. 1674-1678, doi: 10.1126/science.1163589.

Sieh, K., Ward, S.N., Natawidjaja, D., and Suwargadi, B.W., 1999, Crustal deformation at the Sumatran Subduction Zone revealed by coral rings: Geophys. Res. Lett., v. 26, no. 20, p. 3141-3144.

Sobolev, S.V., Babeyko, A.Y., Wang, R., Galas, R., Rothacher, M., Lauterjung, J., Sein, D., Schröter, J., and Subarya, C., 2006, Towards Real-Time Tsunami Amplitude Prediction: Eos, v. 87, no. 37, p. P. 374, doi: 200610.1029/2006EO370003.

Sobolev, S.V., Babeyko, A.Y., Wang, R., Hoechner, A., Galas, R., Rothacher, M., Sein, D.J., Schröter, J., Lauterjung, J., and Subarya, C., 2007, Tsunami early warning using GPS-Shield arrays: Journal of Geophysical Research, v. 112, p. B08415, doi: 10.1029/2006JB004640.

Sørensen, M.B., and Atakan, K., 2008, Continued Earthquake Hazard in Northern Sumatra: Eos, v. 89, no. 14, p. P. 133, doi: 200810.1029/2008EO140001.

Steinmetz, T., Raape, U., Teßmann, S., Strobl, C., Friedemann, M., Kukofka, T., Riedlinger, T., Mikusch, E., and Dech, S., 2010, Tsunami early warning and decision support: Natural Hazards and Earth System Sciences,.

Stein, S., and Okal, E.A., 2005, Seismology: Speed and size of the Sumatra earthquake: Nature, v. 434, no. 7033, p. 581-582, doi: 10.1038/434581a.

Stosius, R., Beyerle, G., Helm, A., Hoechner, A., and Wickert, J., 2010, Simulation of space-borne tsunami detection using GNSS-Reflectometry applied to tsunamis in the Indian Ocean: Natural Hazards and Earth System Sciences, v. 10, no. 6, p. 1359-1372, doi: 10.5194/nhess-10-1359-2010.

Stosius, R., Beyerle, G., Hoechner, A., Wickert, J., and Lauterjung, J., 2011, The impact on tsunami detection from space using GNSS-reflectometry when combining GPS with GLONASS and Galileo: Advances in Space Research, v. 47, no. 5, p. 843-853, doi: 10.1016/j.asr.2010.09.022.

Subarya, C., Chlieh, M., Prawirodirdjo, L., Avouac, J.-P., Bock, Y., Sieh, K., Meltzner, A.J., Natawidjaja, D.H., and McCaffrey, R., 2006, Plate-boundary deformation associated with the great Sumatra–Andaman earthquake: Nature, v. 440, no. 7080, p. 46-51, doi: 10.1038/nature04522.

SuGAr Sumatran cGPS Array, Sumatran plate boundary observatory, California Institute of Technology: URL: http://www.tectonics.caltech.edu/sumatra/sugar.html.

Tang, L., Titov, V.V., and Chamberlin, C.D., 2009, Development, testing, and applications of site-specific tsunami inundation models for real-time forecasting: Journal of Geophysical Research, v. 114, p. C12025, doi: 10.1029/2009JC005476.

Tanioka, Y., and Satake, K., 1996, Tsunami generation by horizontal displacement of ocean bottom: Geophysical Research Letters, v. 23, no. 8, p. PAGES 861–864.

Tapley, B.D., Bettadpur, S., Watkins, M., and Reigber, C., 2004, The gravity recovery and climate experiment: Mission overview and early results: Geophysical Research Letters, v. 31, no. 9, doi: 10.1029/2004GL019920.

Tinti, S., and Gavagni, I., 1995, A smoothing algorithm to enhance finite-element tsunami modelling: An application to the 5 February 1783 Calabrian case, Italy: Natural Hazards, v. 12, no. 2, p. 161-197, doi: 10.1007/BF00613075.

Titov, V.V., 2009, Tsunami forecasting, *in* The Sea, Tsunamis, Harvard University Press, edited by Bernard, E. N. and Robinson A. N., p. 371-400.

USGS, 2009, Magnitude 7.5 - southern Sumatra, Indonesia:.

Vigny, C., Simons, W.J.F., Abu, S., Bamphenyu, R., Satirapod, C., Choosakul, N., Subarya, C., Socquet, A., Omar, K., Abidin, H.Z., and Ambrosius, B.A.C., 2005, Insight into the 2004 Sumatra-Andaman earthquake from GPS measurements in southeast Asia: Nature, v. 436, no. 7048, p. 201-206, doi: 10.1038/nature03937.

de Viron, O., Panet, I., Mikhailov, V., Van Camp, M., and Diament, M., 2008, Retrieving earthquake signature in grace gravity solutions: Geophysical Journal International, v. 174, no. 1, p. 14-20, doi: 10.1111/j.1365-246X.2008.03807.x.

Wang, R., 1999, A simple orthonormalization method for stable and efficient computation of Green's functions: Bulletin of the Seismological Society of America, v. 89, no. 3, p. 733-741.

Wang, R., Lorenzo-Martín, F., and Roth, F., 2006, PSGRN/PSCMP--a new code for calculating co- and post-seismic deformation, geoid and gravity changes based on the viscoelastic-gravitational dislocation theory: Computers & Geosciences, v. 32, no. 4, p. 527-541, doi: 10.1016/j.cageo.2005.08.006.

Wang, R., Martín, F.L., and Roth, F., 2003, Computation of deformation induced by earthquakes in a multi-layered elastic crust--FORTRAN programs EDGRN/EDCMP: Computers & Geosciences, v. 29, no. 2, p. 195-207, doi: 10.1016/S0098-3004(02)00111-5.

Wei, Y., Bernard, E.N., Tang, L., Weiss, R., Titov, V.V., Moore, C., Spillane, M., Hopkins, M., and Kânoğlu, U., 2008, Real-time experimental forecast of the Peruvian tsunami of August 2007 for U.S. coastlines: Geophysical Research Letters, v. 35, no. 4, doi: 10.1029/2007GL032250.

Wells, D.L., and Coppersmith, K.J., 1994, New empirical relationships among magnitude, rupture length, rupture width, rupture area, and surface displacement: Bulletin of the Seismological Society of America, v. 84, no. 4, p. 974-1002.

Wyss, M., and Stefansson, R., 2006, Nucleation Points of Recent Mainshocks in Southern Iceland, Mapped by b-Values: Bulletin of the Seismological Society of America, v. 96, no. 2, p. 599-608, doi: 10.1785/0120040056.

Zachariasen, J., Sieh, K., Taylor, F.W., Edwards, R.L., and Hantoro, W.S., 1999, Submergence and uplift associated with the giant 1833 Sumatran subduction earthquake: Evidence from coral microatolls: Journal of Geophysical Research, v. 104, no. B1, p. PP. 895-919, doi: 199910.1029/1998JB900050.

Zumberge, J.F., Heflin, M.B., Jefferson, D.C., Watkins, M.M., and Webb, F.H., 1997, Precise point positioning for the efficient and robust analysis of GPS data from large networks: Journal of Geophysical Research, v. 102, no. B3, p. PP. 5005-5017, doi: 199710.1029/96JB03860.

13 List of Figures

14 List of tables

15 Acknowledgments

I want to thank my supervisor and head of the geodynamic modeling group at GFZ Dr. Stephan Sobolev, for giving me a lot of freedom in choosing the direction of my research and helping me to focus on key points with good advice and ideas. I enjoyed the cooperation, fruitful discussions and careful considerations with Dr. Andrey Babeyko, responsible for source modeling in GITEWS. Thanks also to the other colleagues from our group and GITEWS for an inspiring environment. Our floor neighbors, the field engineers doing the really hard work in Indonesia, had always a good story to tell. It was interesting to follow the progress made by the seismologists and software developers from GEMPA, to whom I wish good luck. Thanks to Prof. Dr. Michael Weber, director of the department ‘Physics of the Earth’ at GFZ for taking me to the SPICE workshop in Corsica, the best trip I made during my PhD. I profited a lot from exchange with my coauthors Indridi Einarsson and Dr. Ralf Stosius. It was great to have Dr. Rongjiang Wang, author of several of the codes I used during my study, at disposition whenever there were problems. Thanks to Prof. Dr. Gerd Teschke for the discussions about inversion methods and for relying on me as an assessor. I admire the way in which Prof. Dr. Jörn Behrens, responsible for the simulation system, managed to coordinate efforts in order to deliver a working product in time, and the way in which Jörn Lauterjung overcame all obstacles to make GITEWS a success. Thanks to Dr. Alexander Rudloff and PD Dr. Johannes Schneider for valuable input and to Ade Anggraini for translating the abstract into Bahasa Indonesia. Special thanks to my family.